Università degli Studi di Ferrara

DOTTORATO DI RICERCA IN FISICA

CICLO XVII

COORDINATORE: *Prof. Giovanni Fiorentini*

Study of the $B^0 \to D^{*-}\ell^+\nu_\ell$ Decay with the Partial Reconstruction Technique

---

DOTTORANDO:
Dott. Mirco Andreotti

TUTORE:
Prof. Roberto Calabrese

Dott. Concezio Bozzi

ANNO 2002/2004

Ai miei genitori,
Marco e Marina

Solamente il viso dell'angelo che scorgi
guardando la luna alta nel cielo
appartiene alla persona capace
di colmarti di gioia il cuore e di
migliorarti con un sincero sorriso.

Contents

Introduction

In this thesis I will present a measurement of the branching ratio of the decay $B^0 \to D^{*-}\ell^+\nu_\ell$ from data collected by the *BABAR* Experiment. The *BABAR* Experiment at the PEP-II asymmetric B Factory has been taking data on the $\Upsilon(4S)$ resonance since 1999, collecting about 260 fb^{-1} by the end of 2004.
The physics program of the *BABAR* experiment is mainly based on measurements of the violation of the CP symmetry in B mesons in order to test the validity of the CKM approach to CP violation in the Standard Model of the electroweak interactions.
Various analyses in *BABAR* measured and are measuring the CKM matrix elements $|V_{ub}|$ and $|V_{cb}|$. Both of them need to be determined more accurately to test the Standard Model, and in this thesis I study the $B^0 \to D^{*-}\ell^+\nu_\ell$ decay as a first step towards a measurement of $|V_{cb}|$.

The CKM matrix element $|V_{cb}|$ can be extracted by measuring the differential branching ratio $d\mathcal{B}/dq^2$ of the decay $B^0 \to D^{*-}\ell^+\nu_\ell$ and its charge conjugated ($\overline{B}^0 \to D^{*+}\ell^-\overline{\nu}_\ell$) as a function of the 4-momentum transfer from the B to the D^* meson. The Branching ratio $\mathcal{B}\left(B^0 \to D^{*-}\ell^+\nu_\ell\right)$ has been subject to various measurements, but the agreement between them is not so good. One of these measurements has been performed by *BABAR* and results to be within two standard deviations from the world average. The uncertainty on $\mathcal{B}\left(B^0 \to D^{*-}\ell^+\nu_\ell\right)$ measured by *BABAR* is dominated by systematic effects, the main contribution comes from the final state reconstruction in exclusive modes. This fact suggests to measure the $\mathcal{B}\left(B^0 \to D^{*-}\ell^+\nu_\ell\right)$ with a different technique. The decay $D^{*\pm} \to D^0\pi^\pm$ has a special kinematics that allows to implement a partial reconstruction of the D^* by detecting only the soft pion from its decay. The partial reconstruction of the D^* does not require the full reconstruction of the D^0 decay chain, therefore the systematic uncertainties introduced by the reconstruction of the D^0 decay products and by the limited knowledge of the D^0 branching ratios do not enter in the final evaluation of the branching ratio. Moreover, in order to reduce background contamination, the partial reconstruction of $B^0 \to D^{*-}\ell^+\nu_\ell$ will be done on the recoil of fully reconstructed B decays. The drawback due to the small efficiency for fully reconstructing one B meson in the event is compensated by the large data samples collected at the B Factory, resulting in a competitive measurement, not dominated by systematical uncertainties.

In this thesis the D^* partial reconstruction has been developed for the extraction of the number of $B^0 \to D^{*-}\ell^+\nu_\ell$ events in order to measure the $\mathcal{B}\left(B^0 \to D^{*-}\ell^+\nu_\ell\right)$. A conservative estimate of the systematic errors has been performed, and a result comparable with the existing measurements of $\mathcal{B}\left(B^0 \to D^{*-}\ell^+\nu_\ell\right)$ has been obtained. The statistical and systematic errors result to be comparable, however systematics can be reduced by a more detailed approach.

Since in this analysis the lepton reconstruction plays an important role, I will describe also the upgrade of the muon detector (IFR) of *BABAR*. The upgrade of the barrel IFR consists of the replacement of the actual RPCs with LSTs. In summer 2004 two sextants of the barrel have been replaced, but data collection has not yet started. Data with new muon detector will be used for a future update of this analysis.

In Chapter 1 the theoretical arguments concerning semileptonic decays and the $B^0 \to D^{*-}\ell^+\nu_\ell$ decay will be illustrated. The Prediction of the Heavy Quark Effective Theory (HQET) concerning the interested process will be shown, together with the method to extract the $|V_{cb}|$ matrix element. The existing measurements of $\mathcal{B}\left(B^0 \to D^{*-}\ell^+\nu_\ell\right)$ and $|V_{cb}|$ will be also shown.

The *BABAR* detector will be described in Chapter 2.

In Chapter 3 the LST project for the barrel IFR upgrade will be illustrated. This includes the proposal of the upgrade, the R&D performed on LST prototypes, the production of LSTs and the first performance of the two replaced sextants of the IFR.

In Chapter 4 we illustrate the reconstruction of the events, from the full reconstruction of one B meson to the partial reconstruction on the recoiling B. Studies of different methods for the soft pion detection will be illustrated.

In Chapter 5 we will describe the method used for signal extraction and background subtraction, calculate the $\mathcal{B}\left(B^0 \to D^{*-}\ell^+\nu_\ell\right)$ and evaluate systematic uncertainties. Finally we compare the result obtained from this analysis with all the existing measurements.

In Chapter 6 we give some conclusions on the obtained results and future perspectives.

Appendix A shows the mathematical derivation of the formula for signal extraction and background subtraction.

In appendix B we describe the procedure used to subtract continuum and combinatorial background.

Notes. In the entire thesis we will refer to the $B^0 \to D^{*-}\ell^+\nu_\ell$ process by implicitly implying its charge conjugated process $\overline{B}^0 \to D^{*+}\ell^-\overline{\nu}_\ell$ as well. Throughout this thesis I tried to use consistently natural units $\hbar = c = 1$.

Chapter 1

The Semileptonic Decay $B^0 \to D^{*-}\ell^+\nu_\ell$

In a semileptonic decay the final state particles include a charged lepton, which is the experimental signature for a weak process mediated by the W-boson. From a theoretical point of view a semileptonic decay is relatively simple to study, more simple than an hadronic process, and this can provide measurements of the fundamental parameters of the standard-model and detailed studies of decay dynamics [1].
In particular it is possible to understand and measure the weak coupling between different quark generations, that means to measure the CKM-matrix parameters [2]. It is also possible to extract information concerning the dynamics of strong interactions, for example form factor of the hadrons involved in the process[3].
In this thesis we will concentrate our attention to the semileptonic decay $B^0 \to D^{*-}\ell^+\nu_\ell$, we will measure the branching ratio $\mathcal{B}\left(B^0 \to D^{*-}\ell^+\nu_\ell\right)$ as a first step for a future measurement of the CKM matrix element $|V_{cb}|$. A good measurement of the differential branching ratio as a function of the squared momentum transfered to the lepton pair allows us to extract also the value of CKM matrix element $|V_{cb}|$ with small theoretical uncertainty.

1.1 Semileptonic decays and the CKM Matrix

The flavor-changing quark transition in weak processes is taken into account by the Standard Model using a $V-A$ charged weak current operator $\mathcal{J}^\mu$ that couples to the W-boson, according to the interaction Lagrangian:

$$\mathcal{L}_{int} = -\frac{g}{\sqrt{2}}\left(\mathcal{J}^\mu W_\mu^+ + \mathcal{J}^{\mu\dagger} W_\mu^-\right) \tag{1.1}$$

where for quark transitions

$$\mathcal{J}^\mu = \sum_{ij} V_{ij} J_{ij}^\mu = \sum_{ij} \overline{u}_i \gamma^\mu \frac{1}{2}(1-\gamma_5) V_{ij} d_j \tag{1.2}$$

where indexes i and j run over the three quark generations, so that the field operators u_i (i=1,2,3) annihilate u, c and t (or create their antiparticles), and the d_j annihilate d, s and b. The matrix V_{ij} mixes the three quarks of charge $-e/3$ [2], this happens because the quark mass eigenstates are not the weak eigenstates. A weak charged current process between quarks will be proportional to the associate matrix element: for example the processes $d_j \to W^- u_i$ and $\overline{u}_i \to W^- \overline{d}_j$ are proportional to V_{ij}, while $u_j \to W^+ d_i$ and $\overline{d}_i \to W^+ \overline{u}_j$ are proportional to V_{ij}^*. The matrix V_{ij} is the CKM matrix that will be described in more detail in the next section.
The coupling of leptons to the W is also governed by a $V-A$ charged current, but the analog CKM matrix for leptons is the unit matrix, because the neutrino is assumed to be massless in Standard Model.

In order to obtain the transition amplitude of a meson M into a meson X in the contest of the semileptonic decay, like a process $M \to X l\nu$, the quark and lepton current operator must be sandwiched between physical states. Concerning the lepton, this calculation gives directly an expression in terms of Dirac spinors, while for the involved hadrons the situation is more complicated. The hadronic current cannot be easily evaluated, because the quark are confined into hadron by strong interaction and nonperturbative effects have important effects of the physical states. The hadronic current is parametrized with form factors in order to take into account the structure of the involved hadrons and strong interaction effects. Section 1.3.1 presents a discussion on form factor.

If the energy involved in the process is much less than the W mass, it is possible to obtain a phenomenological form of the decay amplitude by using an approximate form for the W propagator and the relation $G_F/\sqrt{2} = g^2/(8M_W^2)$. The amplitude for the semileptonic decay $M_{Qq} \to X_{q'q} l\nu$ of a meson M_{Qq} (composed by quarks Qq) into a meson $X_{q'q}$ (composed by quarks $q'q$) can be written:

$$\mathcal{M}\left(M_{Qq} \to X_{q'q} l\nu\right) = -i\frac{G_F}{\sqrt{2}} V_{q'Q} L^\mu H_\mu \tag{1.3}$$

where L^μ and H_μ are respectively the leptonic and hadronic current. The first one can be expressed in terms of Dirac spinors:

$$L^\mu = \overline{u}_l \gamma^\mu (1-\gamma_5) v_\nu \tag{1.4}$$

The hadronic current is related to the matrix element of the operator J_μ given in eq.1.2:

$$H_\mu = \langle X | \overline{q}' \gamma_\mu (1-\gamma_5) Q | M \rangle \tag{1.5}$$

The hadronic current cannot be calculated in a simple manner, but as we said before, it is possible to express it in term of form factors. The elements $V_{q'Q}$ is the magnitude of the the mixing between quarks q' and Q.

In the Standard Model the quark mass eigenstates are not the weak eigenstates, and the CKM matrix relates these bases. This matrix was defined for six quarks and an explicit parametrization was given by Kobayashi and Maskawa in 1973 [2]. The CKM matrix is unitary and operates on three quarks of charge $-e/3$ (d, s and b):

$$\begin{pmatrix} d' \\ s' \\ b' \end{pmatrix} = \begin{pmatrix} V_{ud} & V_{us} & V_{ub} \\ V_{cd} & V_{cs} & V_{cb} \\ V_{td} & V_{ts} & V_{tb} \end{pmatrix} \begin{pmatrix} d \\ s \\ b \end{pmatrix} \tag{1.6}$$

There are several parametrizations of the CKM matrix, the "standard" one [5] utilizes the angles θ_{12}, θ_{23}, θ_{13} and a phase δ_{13}:

$$V = \begin{pmatrix} c_{12}c_{13} & s_{12}c_{13} & s_{13}e^{-i\delta_{13}} \\ -s_{12}c_{23} - c_{12}s_{23}s_{13}e^{i\delta_{13}} & c_{12}c_{23} - s_{12}s_{23}s_{13}e^{i\delta_{13}} & s_{23}c_{13} \\ s_{12}s_{23} - c_{12}c_{23}s_{13}e^{i\delta_{13}} & c_{12}s_{23} - s_{12}c_{23}s_{13}e^{i\delta_{13}} & c_{23}c_{13} \end{pmatrix} \tag{1.7}$$

where $c_{ij} = \cos\theta_{ij}$ and $s_{ij} = \sin\theta_{ij}$ for the generation labels $i, j = 1, 2, 3$. The interpretation of this parametrization allows the mixing between two generation to vanish when the angles between these vanishes, for example for $\theta_{23} = \theta_{13} = 0$ the third generation decouples from the first two generations and the parametrization reduces to the usual Cabibbo mixing of the first two generations, where $\theta_{12} = \theta_C$ (the Cabibbo angle).

The matrix elements can be directly measured from decay processes. A good approximation is $c_{13} = 1$ then we can relate elements in eq.1.6 with those in eq.1.7 as follows: $V_{ud} = c_{12}$, $V_{us} = s_{12}$, $V_{ub} = s_{13}e^{-i\delta_{13}}$, $V_{cb} = s_{23}$ and $V_{tb} = c_{23}$.

In order to emphasize the hierarchy in the size of angles ($s_{12} \gg s_{23} \gg s_{13}$) an approximation of the CKM matrix, due to Wolfenstein [6] is commonly used. In the Wolfenstein parametrization one sets the parameter $\lambda \equiv s_{12}$, and the other elements are written in powers of λ:

$$V \approx \begin{pmatrix} 1 - \lambda^2/2 & \lambda & A\lambda^3(\rho - i\eta) \\ -\lambda & 1 - \lambda^2/2 & A\lambda^2 \\ A\lambda^3(1 - \rho - i\eta) & -A\lambda^2 & 1 \end{pmatrix} + \mathcal{O}(\lambda^4) \tag{1.8}$$

where A, ρ and η are real numbers close to the unity, and can be expressed in term of the matrix elements in eq.1.6 by the following relations:

$$\frac{|V_{cb}|}{|V_{us}|^2} = A \quad \left|\frac{V_{ub}^*}{V_{cd}V_{cb}}\right| = \sqrt{\rho^2 + \eta^2} \tag{1.9}$$

Applying the orthogonality condition to the first and third columns in eq.1.6, we obtain a useful relation between the two smallest elements of the CKM matrix, V_{ub} and V_{td}:

$$V_{ud}V_{ub}^* + V_{cd}V_{cb}^* + V_{td}V_{tb*} = 0 \tag{1.10}$$

In the parametrization given in eq.1.8 V_{cb}, V_{cd} and V_{tb} are real, then using $V_{ud} \simeq V_{tb} \simeq 1$ and $V_{cd} < 0$ we obtain the following relation:

$$\frac{V_{ub}^*}{|V_{cd}V_{cb}|} + \frac{V_{td}}{|V_{cd}V_{cb}|} = 1 \tag{1.11}$$

this relation can be expressed by a triangle in the complex plain, which is commonly referred to Unitary Triangle. Looking at the second relation in eq.1.9 it is clear that ρ and η are the real and imaginary components of the first term in eq.1.11.

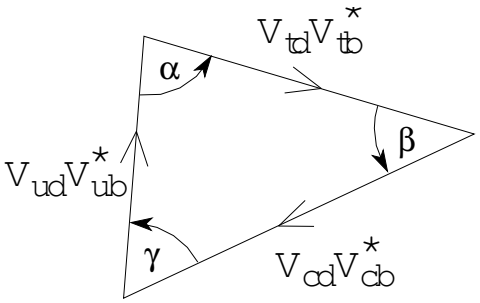

(a)

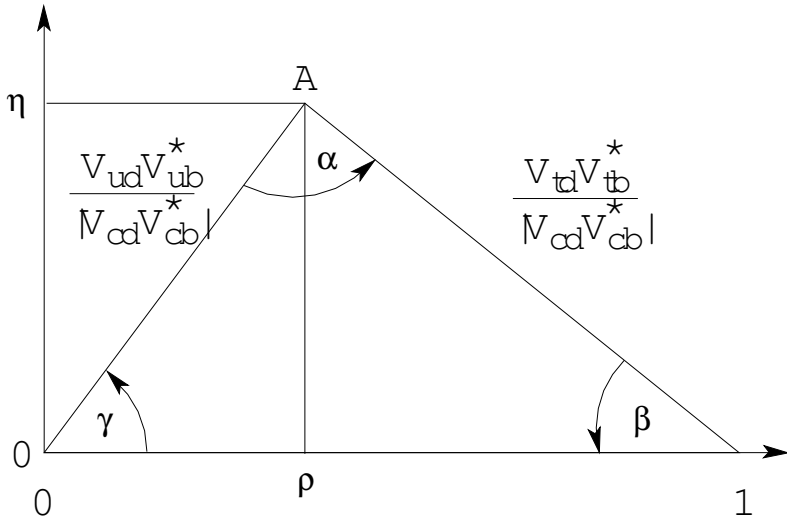

(b)

Figure 1.1: The Unitary Triangle. Figure (a) is the representation of equation 1.11 in the complex plane with the length of the sides indicated in terms of the complex CKM matrix elements. Figure (b) shows the Unitary Triangle with all sides scaled by $V_{cb}^* V_{cd}$ with vertexes (0,0), (1,0) and (ρ, η).

1.2 Dynamics of the semileptonic decay $B^0 \to D^{*-}\ell^+\nu_\ell$

In order to have a qualitative picture of the dynamics of the semileptonic decay $B^0 \to D^{*-}\ell^+\nu_\ell$ we can treat a more general case of a semileptonic decay of a pseudoscalar meson P into a vector meson V,$P \to Vl\nu$, both composed of an heavy and a light quark [3].

A powerful tool for describing the dynamics is the Dalitz plot, which gives us the probability

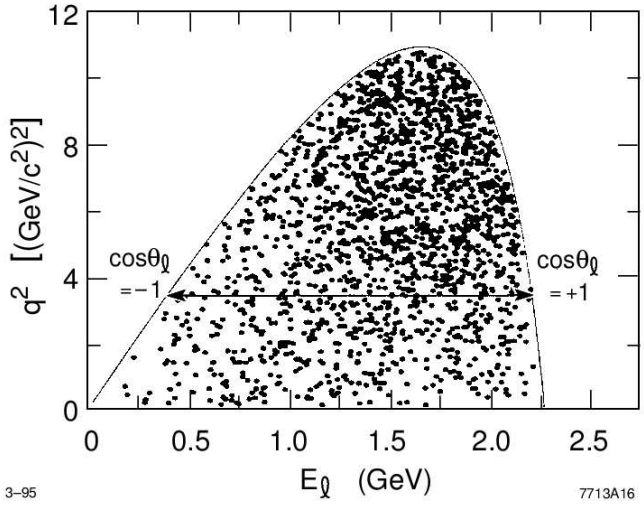

Figure 1.2: A Monte Carlo simulation of the Dalitz plot for the process $B^0 \to D^{*-}\ell^+\nu_\ell$, using HQET-based form factors from Neubert [7]. The form factors are largest at high q^2, which increases the density of points toward the top of the plot. At a fixed value of q^2, the range in lepton energies from left to right corresponds to the variation of $\cos\theta_l$, where θ_l is the polar angle of the lepton in W^* rest frame, from -1 to +1 (see Fig.1.3). The increase in density across the Dalitz plot from left to right can be traced to the $\cos\theta_l$ distribution, which is asymmetric due to the $V-A$ coupling. This coupling enhances the amplitude for the negative-helicity state for W^* relative to the positive-helicity state. Special cases occur at q^2_{max}, where the W^* (or the D^*) is unpolarized, and at $q^2 = 0$, where it is in a pure helicity zero state.

for the different kinematic configuration. Commonly used variables are the squared momentum transfered to the lepton pair and the energy of the charged lepton in the rest frame of the decaying meson P:

$$q^2 = m^2_{W^*} = (p_l + p_{\overline{\nu}})^2 = (p_P - p_V)^2 = m^2_P + m^2_V - 2m_P E_V \tag{1.12}$$

where p are four-momenta, m are masses and E are energies in P rest frame.

For a given lepton energy E_l, the allowed range for q^2 is given by:

$$\left(m^2_l \approx 0\right) \leq q^2 \leq 2m_P E_l + \frac{2m_V E_l}{2E_l - m_P} \tag{1.13}$$

which defines the boundary of the physical region.

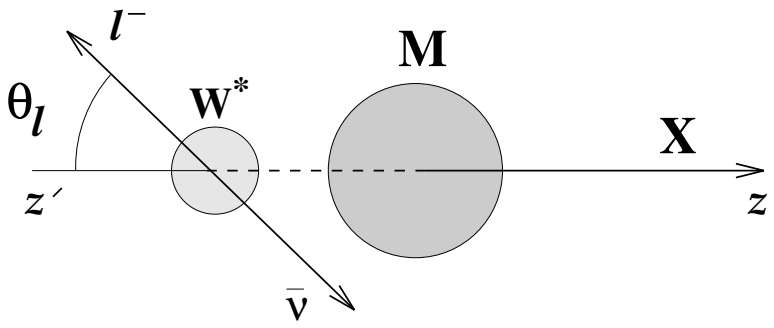

Figure 1.3: The polar angle θ_l is defined in the rest frame of the virtual W^* (denoted here as W^*), in which the charged lepton and the neutrino are back-to-back. The angle is measured with respect to the axis z' pointed opposite to the momentum vector of the daughter meson X (in our case the D^*). In the M rest frame (M here stands for the B pseudoscalar meson) $\vec{p}_{W^*} = -\vec{p}_X$. Due to the Lorentz boost between the W^* and $M(orB)$ rest frames, leptons with small values of θ_l have higher energy in the B rest frame than leptons with large values of θ_l, at fixed q^2.

In order to understand the physics of the decay we have to understand the correlation between the Dalitz plot variables q^2 and E_l shown in Fig.1.2. The characteristic distributions of these variables depend on two effects: the dynamics of formation of the hadronic system V and the spin structure of the decay. Fig.1.3 shows geometry of a semileptonic decay in W^* rest frame.

1.2.1 q^2 distribution

We start to analyze these effects by looking at the q^2 variables. As shown in Fig.1.4 we can look at two different configurations of the decay, namely at high and low q^2. Fig.1.4(a) shows the initial meson containing an heavy quark and a light spectator quark, as for a B meson.

At high q^2 the masses of the daughter heavy meson and of W^* take up most of the available energy, so both V and W^* will be nearly at rest: the lepton pair will therefore be produced nearly back-to-back. This means that the daughter meson receives little or no momentum kick, then this can be seen as a "zero-recoil" configuration, where $E_V \approx m_V$ and $q^2 = q^2_{max} = (m_P - m_V)^2$. Another important effect of the zero-recoil configuration is that the light degrees of freedom [1] between initial and final mesons are almost completely undisturbed. If both initial and final quarks are heavy compared to Λ_{QCD} [2], as in $b \to cl\nu$, an heavy static source of color field at the

[1] The so-called light degrees of freedom is the motion of an heavy quark relative to the spectator light quark and the gluons as can happens in meson B or D^*

[2] Λ_{QCD} provides a parametrization of strong coupling constant α_s. It has the dimension of a mass and typical value is ≈ 300 MeV.

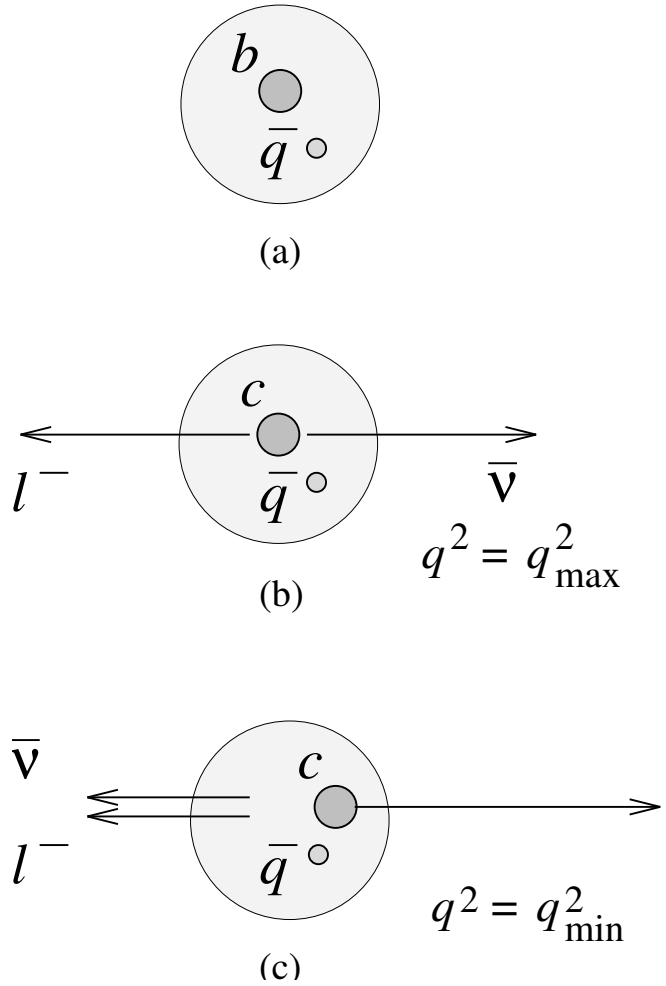

Figure 1.4: Kinematic configuration for the semileptonic decay of a B meson: (a) B meson before decay; (b) decay configuration for $q^2 = q^2_{\rm max}$ (zero recoil or $w = 1$, where the form factors are largest for producing a D^* vector meson in the final state; (c) decay configuration for $q^2 = q^2_{\rm min}$, where the form factors are smallest.

center of the initial meson is replaced by a source of color field of a different flavor, but the color field is unchanged.

Moreover the zero-recoil configuration and the heavy masses of involved quarks (as b and c quarks) allows us to ignore relativistic effects, and also in this configuration the heavy quarks are nearly at rest. The later considerations are the basic ideas of the Heavy Quark Effective Theory (HQET) that we will treat in more details in the next section.

It is clear from the above considerations that the region of phase space around the q^2_{max}

configuration is quite special. The spectator and the daughter quarks are produced in a state that has a large overlap with the wave function of an ordinary non-excited meson, thus the decay rate for processes like $B^0 \to D^{*-}\ell^+\nu_\ell$ are largest in this configuration and decrease with q^2, or with the increasing of the velocity recoil of the daughter meson. This behavior results clear also from the Dalitz plot, in fact the density of the events is higher at higher q^2, we have to note that at q^2_{max} there is not a peak, because at the maximum value of q^2 the phase space vanishes.

At low q^2 the lepton and neutrino are nearly parallel and the daughter quark receives a large kick, then the formation of mesons is less favorable, because gluons have to be exchanged in order to bound the daughter quark to form a bound state. This situation is more similar to the formation of jets.

1.2.2 Lepton energy distribution

The lepton energy spectrum is affected by three aspects: (1) the $V-A$ coupling, (2) the quantum number of the final meson V, and (3) the distribution in q^2. See Fig.1.5 for a graphical rappresentation of the following discussions.

$V-A$ coupling

The $V-A$ coupling gives different results in semileptonic decays of b and c quarks. In a process $b \to c\, l^-\, \overline{\nu}$ and $b \to u\, l^-\, \overline{\nu}$ the produced quarks c and u have predominantly helicity $\lambda = -1/2$ in association with a charged lepton that has almost $\lambda = -1/2$. The case is different for processes involving the decay of a quark c, like $c \to s\, l^+\nu$ and $c \to d\, l^+\nu$, where s and d quarks have predominantly helicity $\lambda = -1/2$ in association with a charged lepton with helicity $\lambda = +1/2$. A direct consequence of this behavior is a collinear configuration in which the charged lepton recoils against the daughter quark and the neutrino. This configuration with highest charged lepton energy is allowed for b decays, but forbidden for c decays by angular momentum conservation. Then in the case of b (or $\overline{b}$) decays, the lepton energy spectrum peaks at a higher energy than the neutrino spectrum, while the situation is reversed for c decays.

Quantum number of final meson V

The lepton energy spectrum depends also on the quantum number of the final meson. In fact different spectra will be obtained from vector meson or from a pseudoscalar meson. In the case of a pseudoscalar meson the information on the helicity is lost, while in the case of a vector meson, its spin-1 plays an important role on the energy spectrum. For a vector meson it is more probable to have an helicity $\lambda = -1$ than $\lambda = +1$. The W^* meson has to be the same helicity of the meson V, then the predominance of $\lambda_{W^*} = -1$ affects the energy spectrum of the charged lepton, that will be produced with $\lambda = -1/2$: the angular distribution of the charged lepton in W^* rest

frame will be $(1 + \cos\theta_l)^2$. The Lorentz boost will typically produce a hard lepton spectrum in this configuration. Then for the decay processes like $B^0 \to D^{*-}\ell^+\nu_\ell$ the spectrum of the charged lepton will be harder than the spectrum of the neutrino.

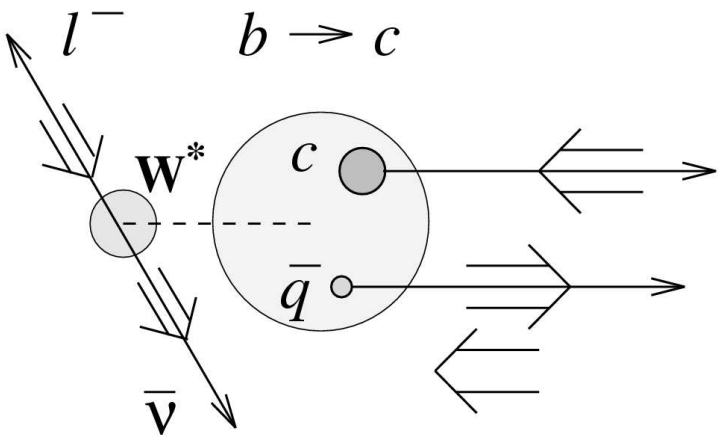

Figure 1.5: In B semileptonic decay, the $V - A$ coupling at the $b \to c$ (or $b \to u$) vertex produces a c quark that is predominantly helicity $\lambda = -1/2$, In the simple model shown here, the helicity of the meson X is then determined by whether the c quark combines with a spectator quark that has $\lambda = \pm 1/2$. If X is a spin-zero meson, only $\lambda = +1/2$ spectator quarks can contribute. If X has spin 1, both helicities of spectator quarks contribute, leading to X helicities of $\lambda = 0$ and $\lambda = -1$, but not $\lambda = +1$. It is easy to see that this $V - A$ effect, combined with overall angular momentum conservation, results in a harder energy spectrum for the charged lepton than for the neutrino, as observed in the rest frame of M.

q^2 distribution

A direct consequence of a more populated q^2 distribution at high q^2 is the fact that also E_l will be high. This effect is absorbed in the case of a pseudoscalar final meson where P-wave suppresses high q^2. In our case, since the final particle is a vector meson, we will have more probability to find an event with both high E_l and q^2.

Summarizing our understanding of the Dalitz plot for the process $B^0 \to D^{*-}\ell^+\nu_\ell$, we can say that when q^2 is large, the D^* is very slow and it is unpolarized: λ = -1, 0 and +1 are present with about the same probability. The W^* is also unpolarized, resulting in a uniform $\cos\theta_l$ distribution. The form factor in this region is high. As q^2 decreases the $\lambda = -1$ component of the D^* begins to dominate over the $\lambda = +1$ component, this is the cause of the higher probability on the right side of the Dalitz plot than on the left side. At low values of q^2 the lepton and the neutrino are parallel in the B meson rest frame. This is the situation when recoil of the D^* is maximum, then both D^*

and W^* are forced into a pure $\lambda = 0$ state.
The above discussion is just to give a qualitative description of the semileptonic decay. A more detailed description of the form factors will be presented in the next section.

1.3 Theory of exclusive semileptonic decays of $B^0 \to D^{*-}\ell^+\nu_\ell$

In this section we describe the theoretical approaches used to predict the semileptonic decay $B^0 \to D^{*-}\ell^+\nu_\ell$. We start with the standard parametrizations of the hadronic current in term of a single form factor. We will discuss briefly some quark models used to predict the form factors, then we will describe them in terms of HQET [9]. Finally the Isgur-Wise model and its corrections will be discussed [10].

1.3.1 Structure of hadronic currents

The hadronic current in semileptonic decays has to be constructed from the available four-vectors, which are momenta and spin-polarization vectors. In order to take into account the internal structure of the involved hadron the hadronic current has to be parametrized in terms of Lorentz-invariant form factors.
For the process $B^0 \to D^{*-}\ell^+\nu_\ell$ each term in the current must be linear in the polarization vector ϵ of the vector meson D^*, then the hadronic current will have the following general expression:

$$\begin{aligned}\left\langle D^*(p^{'},\epsilon)\left|V^\mu - A^\mu\right|B(p)\right\rangle = &\frac{2i\epsilon^{\mu\nu\alpha\beta}}{m_B + m_{D^*}}\epsilon^*_\nu p^{'}_\alpha p_\beta V(q^2) - (m_B + m_{D^*})\epsilon^{*\mu}A_1(q^2)\\ &+ \frac{\epsilon^*\cdot q}{m_B + m_{D^*}}(p + p^{'})^\mu A_2(q^2) + 2m_{D^*}\frac{\epsilon^*\cdot q}{q^2}q^\mu A_3(q^2)\\ &- 2m_{D^*}\frac{\epsilon^*\cdot q}{q^2}q^\mu A_0(q^2)\end{aligned} \tag{1.14}$$

where $V^\mu = \overline{q}^{'}\gamma^\mu Q$, $A^\mu = \overline{q}^{'}\gamma^\mu\gamma_5 Q$ and

$$A_3(q^2) = \frac{m_B + m_{D^*}}{2m_{D^*}}A_1(q^2) - \frac{m_B - m_{D^*}}{2m_{D^*}}A_2(q^2) \tag{1.15}$$

with $A_0(q^2) = A_3(q^2)$. The terms proportional to q^μ play an important role only for $l = \tau$, then with good approximation we can neglect them and the hadronic current becomes:

$$\begin{aligned}\left\langle D^*(p^{'},\epsilon)\left|V^\mu - A^\mu\right|B(p)\right\rangle = &\frac{2i\epsilon^{\mu\nu\alpha\beta}}{m_B + m_{D^*}}\epsilon^*_\nu p^{'}_\alpha p_\beta V(q^2) - (m_B + m_{D^*})\epsilon^{*\mu}A_1(q^2)\\ &+ \frac{\epsilon^*\cdot q}{m_B + m_{D^*}}(p + p^{'})^\mu A_2(q^2)\end{aligned} \tag{1.16}$$

The form factor $A_1(q^2)$ and $A_2(q^2)$ can be associated with the exchange of a particle with quantum number $J^P = 1^+$, while $V(q^2)$ is associated with $J^P = 1^-$. $A_1(q^2)$ contributes to all three helicity components of the D^* meson, $A_2(q^2)$ contributes to the helicity-zero component and $V(q^2)$ contributes only to the ± 1 helicity components.

As said before the form factors take into account the strong interactions inside the hadron involved in the decays, then form factors have to be calculated in the framework of strong interactions. Several quark-model calculation have been performed to determine form factors. Quark-model calculations estimate the meson wave function and use it in order to compute the matrix elements that appear in the hadronic currents. These calculations have been performed at particular values of q^2 ($q^2 = 0$ and $q^2 = q^2_{max}$). In a separate step quark-models predict the variation with q^2 of the form factors. These calculations have very large uncertainties, because nonperturbative effects play an important role. Many quark-models as ISGW [10] and WSB [11] have been developed, but none of these have to be taken too seriously. More interesting and useful are the form factors obtained from HQET that we will describe in the next subsection.

1.3.2 Heavy Quark Effective Theory

Heavy quark effective theory (HQET) [9] is a theoretical approach in order to analyze hadrons containing one heavy quark. These theory is used to analyze mesons composed of one heavy and one light quark, and it is also used to study baryons made of one heavy and two light quarks. The basic idea of HQET is that the heavy quark inside the hadron moves non-relativistically. The momentum of the heavy quark ($\vec{p}_Q$) has to be balanced by the momentum of the light quark ($\vec{p}_q$), then $|\vec{p}_Q| = |\vec{p}_q| \approx \Lambda_{QCD}$, of the order of 10^{-1} GeV. When $m_Q >> \Lambda_{QCD}$ the heavy quark behaves essentially like a stationary source of color field. A direct consequence of the heavy quark limit is the heavy quark symmetry that is useful to study the decay of a meson with one heavy quark to a meson with another heavy quark of different flavor. In the limit of infinite heavy quark mass there is no difference between the daughter meson and the decaying one: the initial heavy quark is replaced by another heavy quark of different flavor, but the magnitude of the color field as well as the light degrees of freedom between the two mesons are unchanged. From above consideration it clear that HQET is an useful tool to study the $B^0 \to D^{*-}\ell^+\nu_\ell$ decay, where both B and D^* mesons contain one heavy and one light quark.

In the framework of HQET the appropriate quantity to use instead of q^2 is the four-velocity transfer, since in the heavy quark limit the light quark constituent configuration is not affected by the replacement of an heavy quark $Q(v, s)$ with another heavy quark $Q'(v, s')$. In this approximation the velocity of the heavy quark is also the velocity of the meson. Then HQET calculations use the square of the four-velocity transfer $(v - v')^2 \approx 2(1 - v \cdot v')$, where v and v' are velocity of the initial and daughter meson respectively. In the rest frame of the initial meson the product $v \cdot v'$ is the boost of the final meson, the D^* in our case:

$$v \cdot v' = \gamma_{D^*} = \frac{1}{\sqrt{1 - \beta_{D^*}}} \tag{1.17}$$

In literature the product $v \cdot v'$ is also called w and it is related to the square of transfered momentum

as follows:

$$w \equiv v \cdot v^{'} = \frac{m_B^2 + m_{D^*}^2 - q^2}{2m_B m_{D^*}} \tag{1.18}$$

for the $B^0 \to D^{*-}\ell^+\nu_\ell$ decay, w has a variation of $\delta w = 0.5$, this small range is helpful for the extraction of $|V_{cb}|$ from $B^0 \to D^{*-}\ell^+\nu_\ell$, as it will appear clear soon.
In term of HQET form factors the hadronic current for the decay $B^0 \to D^{*-}\ell^+\nu_\ell$ has this form:

$$\begin{aligned}\langle D^*(v',\epsilon)\,|V^\mu - A^\mu|\,B(v)\rangle = \sqrt{m_B m_{D^*}}[&ih_V(w)\epsilon^{\mu\nu\alpha\beta}\epsilon^*_\nu v'_\alpha v_\beta \\ &- h_{A_1}(w)\epsilon^{*\mu}(w+1) + h_{A_2}(w)v^\mu \epsilon^* \cdot v \\ &+ h_{A_3}(w)v'^\mu \epsilon^* \cdot v]\end{aligned} \tag{1.19}$$

In the heavy quark symmetry limit we obtain [3]:

$$h_V(w) = h_{A_1}(w) = h_{A_3}(w) = \xi(w) \tag{1.20}$$

$$h_{A_2}(w) = 0 \tag{1.21}$$

where $\xi(w)$ is the so called Isgur-Wise [10] function [3] , which can be regarded as the form factor for the elastic scattering of a meson by a current that gives a kick to the heavy quark. Heavy quark symmetry provides the relation 1.21, but it cannot provide the variation of $\xi(w)$ with w.
Of great importance for measuring $|V_{cb}|$ is the results at zero recoil ($w = 1$), where the Isgur-Wise function is equal one: $\xi(1) = 1$.

In the heavy quark symmetry the standard form factors of eq.1.14 are related to the HQET form factors by the following expression [3]:

$$V(q^2) = A_2(q^2) = \frac{A_1(q^2)}{\left[1 - \frac{q^2}{(m_B + m_{D^*})^2}\right]} = R^{*-1}\xi(w) \tag{1.22}$$

where the constant R^* is:

$$R^* = \frac{2\sqrt{m_B m_{D^*}}}{m_B + m_{D^*}} \tag{1.23}$$

In the framework of HQET a particular parametrization of the ratios between form factors can be defined as follows [3]:

$$\frac{h_{A_1}(w)}{h_{A_1}(1)} = 1 - \rho^2_{h_{A_1}}(w-1) \tag{1.24}$$

$$R_1(w) = \frac{h_V(w)}{h_{A_1}(w)} = R_1(1) \tag{1.25}$$

$$R_2(w) = \frac{h_{A_3}(w) + \frac{m_{D^*}}{m_B}h_{A_2}}{h_{A_1}(w)} = R_2(1) \tag{1.26}$$

This description has 3 free parameters: $\rho^2_{h_{A_1}}$, $R_1(1)$ and $R_2(1)$. A more theoretical driven parametrization provided by Caprini et al. [13], involving unitary constraints and dispersive

[3] The Isgur-Wise function can be seen also as a common form factor for decays into pseudoscalar and vector mesons: as a consequence of the heavy quark symmetry, the pseudoscalar and vector mesons are in the same HQET multiplet.

bounds, gives:

$$\frac{h_{A_1}(w)}{h_{A_1}(1)} = 1 - 8\rho^2_{h_{A_1}} z + (53\rho^2_{h_{A_1}} - 15)z^2 - (231\rho^2_{h_{A_1}} - 91)z^3 \tag{1.27}$$

$$R_1(w) = 1.27 - 0.12(w-1) + 0.05(w-1)^2 \tag{1.28}$$

$$R_2(w) = 0.80 + 0.11(w-1) - 0.06(w-1)^2 \tag{1.29}$$

where the variable z is related to w by:

$$z = \frac{\sqrt{w+1} - \sqrt{2}}{\sqrt{w+1} + \sqrt{2}} \tag{1.30}$$

the slope $\rho^2_{h_{A_1}}$ has the same meaning in both parametrizations, and it is the slope of the function $h_{A_1}(w)/h_{A_1}(1)$ versus w evaluated at $w = 1$.
The above parametrizations are needed in order to compute corrections due to the departure from heavy quark symmetry. Concerning the $B^0 \to D^{*-}\ell^+\nu_\ell$ decay we have to point out that a typical value for $w - 1 \approx 0.25$, gives small variations from the unity of the ratios.

1.3.3 The Isgur-Wise Function

As seen before, the heavy quark symmetry relates various form factors to the Isgur-Wise function $\xi(w)$, but HQET cannot predict the variation of ξ with w. In order to predict that it is necessary to use nonperturbative methods like lattice QCD or QCD sum rules, since the Isgur-Wise function describes long-range and soft-gluon interaction inside the hadrons. Concerning the $B^0 \to D^{*-}\ell^+\nu_\ell$ decay the small range of w (from 1 to 1.5) allows to express ξ in Taylor expansion around $w = 1$:

$$\xi(w) \approx 1 - \rho^2(w-1) + \mathcal{O}(w-1)^2 \tag{1.31}$$

This approximation it is expected to work well in the range of variation of w, and the resulting function is characterized primarily by the slope ρ. Other forms for Isgur-Wise function are discussed in literature [3], but experimentally it is very difficult to distinguish among such forms, because the range of w is very small.
The slope ρ^2 is difficult to calculate, it has to be positive and it is expected to range roughly between 0.5 and 2.0. Various predictions of ρ^2 have been calculated from different authors, but it is not simple to compare all results.
The Isgur-Wise function will be discussed in next section concerning the measurement of $|V_{cb}|$.

1.3.4 Decay distribution of $B^0 \to D^{*-}\ell^+\nu_\ell$

The $B^0 \to D^{*-}\ell^+\nu_\ell$ decay where the D^* decays into $D^0\pi^+$ is described by four independent variables: q^2 or w and the angles shown in Fig.1.6. The angle θ_l is measured in the W^* rest frame between the lepton and the opposite of the direction of the D^* in the B rest frame. The angle θ_V

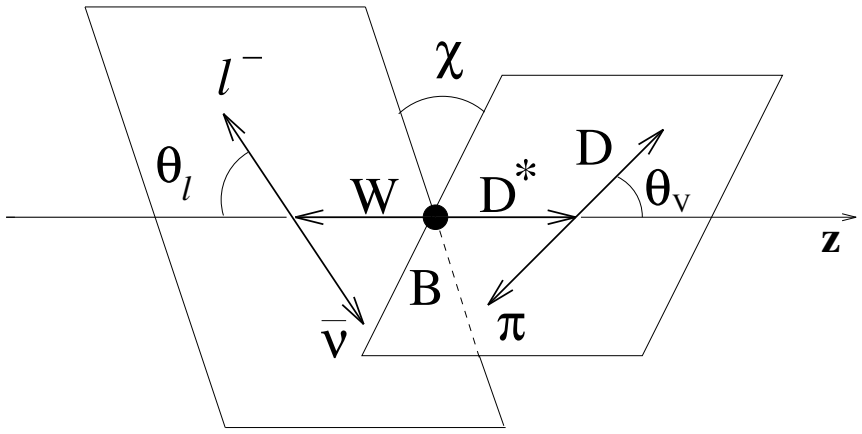

Figure 1.6: Definitions of the angles θ_l, θ_V ($\equiv \theta_{D^*}$) and χ in the decay $B^0 \to D^{*-}\ell^+\nu_\ell$. The lepton and the neutrino are drawn back to back because they are shown in the W^* rest frame. Similarly, the D and the π are shown in the D^* rest frame. The angle θ_l is thus measured in the W^*, while θ_V is measured in the D^* rest frame. The azimuthal angle χ is measured between the W^* and the D^* decay planes.

is measured in the D^* rest frame between the D^0 and the direction of the D^* in the B rest frame. The angle χ is the azimuthal angle between the projection of the momenta of the lepton and the D^0 in the plane perpendicular to the decay axis. The differential decay rate for $B^0 \to D^{*-}\ell^+\nu_\ell$,$D^* \to D^0\pi^+$ can be expressed in terms of these four kinematic variables q^2, θ_l, θ_V and χ as [3]:

$$\begin{aligned}\frac{d\Gamma(B \to D^* l\nu, D^* \to D^0\pi^+)}{dq^2 d\cos\theta_V d\cos\theta_l d\chi} &= \frac{3}{8(4\pi)^4} G_F^2 |V_{cb}|^2 \frac{|\vec{p}_{D^*}|q^2}{m_B^2} \mathcal{B}(D^* \to D^0\pi^+) \\ &\times \{(1-\cos\theta_l)^2 \sin^2\theta_V |H_+(q^2)|^2 \\ &+ (1+\cos\theta_l)^2 \sin^2\theta_V |H_-(q^2)|^2 \\ &+ 4\sin^2\theta_l \cos^2\theta_V |H_0(q^2)|^2 \\ &- 4\sin\theta_l(1-\cos\theta_l)\sin\theta_V\cos\theta_V\cos\chi H_+(q^2)H_0(q^2) \\ &+ 4\sin\theta_l(1+\cos\theta_l)\sin\theta_V\cos\theta_V\cos\chi H_-(q^2)H_0(q^2) \\ &- 2\sin^2\theta_l \sin^2\theta_V \cos 2\chi H_+(q^2)H_-(q^2)\}\end{aligned} \tag{1.32}$$

where $|\vec{p}_{D^*}|$ is evaluated in the B rest frame and is a function of q^2, see eq.1.38. Since the B meson has spin zero, the D^* and W^* must have the same helicity, then the amplitude for helicities 0,+1 and -1 are proportional to $H_0(q^2)$, $H_+(q^2)$ and $H_-(q^2)$ respectively.

It is easy to understand the origin of most terms in eq.1.32. For example, the angular dependence of the $|H_+(q^2)|^2$ coefficient comes from the helicity state $\lambda_{W^*} = +1$, then the decay angular

distribution of the charged lepton in the W^* rest frame is proportional to the Wigner d-function:

$$d^1_{\lambda_{W^*},\lambda_l-\lambda_\nu}(\theta_l) = \frac{1}{2}(1-\cos\theta_l) \tag{1.33}$$

Since $\lambda_{D^*} = +1$, the angular distribution of the D^0 meson in the D^* rest frame is given by

$$d^1_{\lambda_{D^*},\lambda_D-\lambda_\pi}(\theta_V) = \frac{1}{\sqrt{2}}\sin\theta_V \tag{1.34}$$

The helicity amplitudes can be expressed in terms of the set of form factor defined in HQET as follows:

$$H_0(w) = (m_B - m_{D^*})\sqrt{\frac{m_B m_{D^*}}{q^2(w)}}(w+1)h_{A_1}(w)\left[1+\left(\frac{w-1}{1-r}\right)(1-R_2(w))\right] \tag{1.35}$$

and

$$\begin{aligned} H_\pm(w) &= (m_B - m_{D^*})\sqrt{\frac{m_B m_{D^*}}{q^2(w)}}(w+1) \\ &\times h_{A_1}(w)\frac{\sqrt{1-2wr+r^2}}{1-r}\left[1 \mp \sqrt{\frac{w-1}{w+1}}R_1(w)\right] \end{aligned} \tag{1.36}$$

where $r = m_{D^*}/m_B$, the terms $w \pm 1$ are related to q^2 by

$$w \pm 1 = \frac{(m_B \pm m_{D^*})^2 - q^2}{2m_B m_{D^*}} \tag{1.37}$$

By looking at this formula it is clear that for $w \to 1$, H_0 and $H_\pm$ are governed by $h_{A_1}(w)$. Also the tri-momentum $|\vec{p}_{D^*}|$ can be expressed in terms of w by the relation:

$$|\vec{p}_{D^*}| = m_{D^*}\sqrt{w^2-1} \tag{1.38}$$

The differential decay rate given by eq.1.32 can be integrated over $\cos\theta_l$, $\cos\theta_V$ and χ in order to obtain the differential decay rate in terms of q^2, and therefore w, from which it is possible to measure the CKM matrix element $|V_{cb}|$, as we will discuss in the next section.

1.4 The determination of $|V_{cb}|$ with $B^0 \to D^{*-}\ell^+\nu_\ell$ decay

The magnitude of the CKM matrix element $|V_{cb}|$ can be measured in three different ways, using: (1) the inclusive semileptonic rate; (2) the total rates for exclusive $b \to cl\nu$ process like $B^0 \to D^{*-}\ell^+\nu_\ell$; or (3) the partial rate for $B^0 \to D^{*-}\ell^+\nu_\ell$ in the region of phase space where the D^* has very low momentum in the B rest frame. The first method has the advantage that the inclusive semileptonic branching fraction and the B meson lifetimes are measured very well, but theoretical uncertainties play an important role; recent measurements of the moments of the lepton and hadronic invariant mass spectra [16] give reduced theoretical uncertainties. The second method needs the integration over all range of q^2, this means that a good knowledge of

the variation of form factors with q^2 is needed. The third method allows to use the powerful heavy quark symmetry, giving a more reliable extraction of $|V_{cb}|$. Here we will discuss this third method, because it is our idea to follow this path in order to measure the element $|V_{cb}|$.

In order to treat the decay rate in a limited region of w we have to integrate the differential decay rate eq.1.32 over $\cos\theta_l$, $\cos\theta_V$ and χ, obtaining the following expression:

$$\begin{aligned}\frac{d\Gamma(B \to D^* l\nu)}{dw} &= \frac{G_F^2}{48\pi^3} m_{D^*}^3 (m_B - m_{D^*})^2 \sqrt{w^2-1}(w+1)^2 \\ &\times \left[1 + \frac{4w}{w+1}\frac{1-2wr+r^2}{(1-r)^2}\right] |V_{cb}|^2 \mathcal{F}^2(w)\end{aligned} \tag{1.39}$$

The function $\mathcal{F}(w)$ is the product $\mathcal{F}(w) = \eta_A \hat{\xi}(w)$, where $\eta_A = 0.985 \pm 0.015$ is a QCD correction [8], and $\hat{\xi}(w)$ is a form factor which becomes equal to Isgur-Wise function in the heavy quark limit, and it can be written as an expansion in w as $\xi(w)$. The form factor $\hat{\xi}(w)$ is related to $h_{A_1}(w)$ by the expression:

$$\hat{\xi}^2(w) = \frac{\sum_i |\tilde{H}_i(w)|^2}{\left[1 + \frac{4w}{w+1}\frac{1-2wr+r^2}{(1-r)^2}\right]} \eta_A^{-2} |h_{A_1}(w)|^2 \tag{1.40}$$

where $\tilde{H}_i(w)$ are related to $H_i(w)$ by:

$$\tilde{H}_i(w) = \frac{H_i(W)}{(m_B - m_{D^*})\sqrt{\frac{m_B m_{D^*}}{q^2(w)}}(w+1)h_{A_1}(w)} \tag{1.41}$$

Concerning the extraction of $|V_{cb}|$ from eq.1.39 the idea is to measure the branching fraction at a certain value of w, at which $\mathcal{F}(w)$ is well known. In the zero recoil configuration ($w = 1$) the heavy quark symmetry allows to calculate the correction from the departure of $\mathcal{F}(1)$ from the unity. Concerning the $B^0 \to D^{*-}\ell^+\nu_\ell$ decay the first-order correction to $\mathcal{F}(1)$ vanishes as a consequence of Luke's Theorem [12], then the leading correction are of the order $(\Lambda_{QCD}/m_b)^2$, $(\Lambda_{QCD}/m_c)^2$. The value of $\mathcal{F}(1)$ is known theoretically to about 5% level [14]:

$$\mathcal{F}(1) = 0.913 \pm 0.042 \tag{1.42}$$

Recently new results for $\mathcal{F}(1)$ [15] have been obtained with lattice QCD calculations, giving a result compatible with eq.1.42, but with smaller uncertainty:

$$\mathcal{F}(1) = 0.919^{+0.030}_{-0.035} \tag{1.43}$$

This result is obtained after applying a QED correction of +0.007 which reduces the uncertainty to 4%. The basic idea to determine $|V_{cb}|$ is to measure the differential branching fraction of $B^0 \to D^{*-}\ell^+\nu_\ell$ to extrapolate the product $\mathcal{F}(w)|V_{cb}|$ at $w = 1$ and then use the known value of $\mathcal{F}(1)$. In the next section we will discuss the existing measurements of $|V_{cb}|$.

1.5 Existing measurements of $\mathcal{B}\left(B^0 \to D^{*-}\ell^+\nu_\ell\right)$ and $|V_{cb}|$

Many experiments measured the $B^0 \to D^{*-}\ell^+\nu_\ell$ branching fraction and the $\mathcal{F}(1)|V_{cb}|$. The existing measurements of $\mathcal{B}\left(B^0 \to D^{*-}\ell^+\nu_\ell\right)$ are eight as shown in Fig.1.7(a). The χ^2/dof of all these measurements is marginal. The existing *BABAR* measurement has been obtained from an exclusive analysis [20]. Measuring the $\mathcal{B}\left(B^0 \to D^{*-}\ell^+\nu_\ell\right)$ by using a different approach is an important cross-check of the existing results.

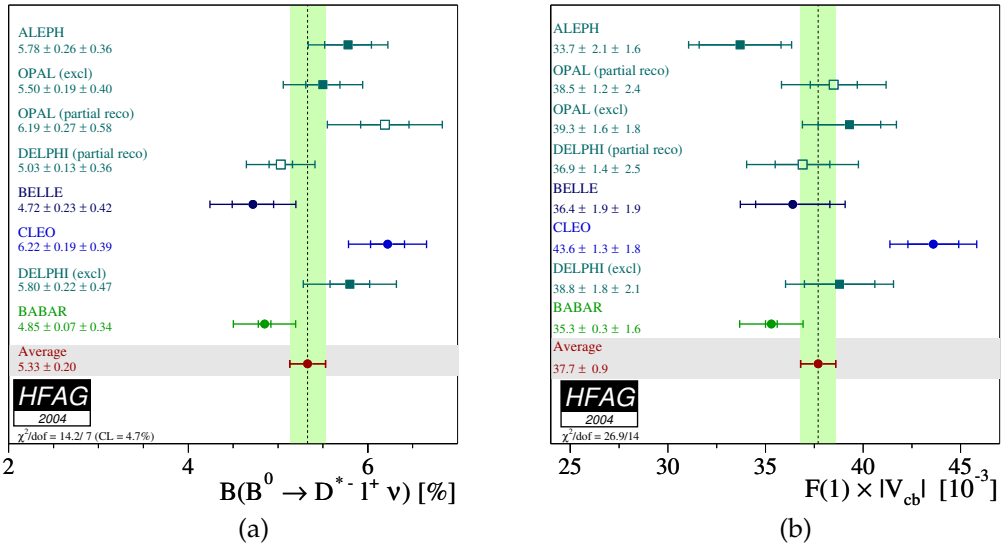

Figure 1.7: (a) All existing measurements of the branching fraction $\mathcal{B}\left(B^0 \to D^{*-}\ell^+\nu_\ell\right)$ [23]. (b) All existing measured values of $\mathcal{F}(1)|V_{cb}|$ [23].

Measurements of the product $\mathcal{F}(w)|V_{cb}|$ as a function of w have been performed at the $\Upsilon(4S)$ by the CLEO [18], BELLE [19] and *BABAR* [20] Collaborations; the results are shown respectively in Fig.1.8(a), (c) and (b). In Fig.1.7(b) all the existing measured values of $\mathcal{F}(1)|V_{cb}|$ are reported. In order to combine the published data, the central values and errors of $\mathcal{F}(1)|V_{cb}|$ and ρ^2 ([4]) are rescaled to the same set of form factors input parameters and their quoted uncertainties. The $\mathcal{F}(1)|V_{cb}|$ values used for this average are extracted using the parametrization adopted by the latest $B^0 \to D^{*-}\ell^+\nu_\ell$ CLEO analysis [18] based on the CLEO experimental determination of the form factor ratios R_1 and R_2 [17]. The LEP data, which originally used theoretical values for these ratios, are rescaled accordingly. The averaging procedure [21] takes into account statistical and systematic correlation between $\mathcal{F}(1)|V_{cb}|$ and ρ^2.

[4] defined as the slope of the form factor at zero recoil.

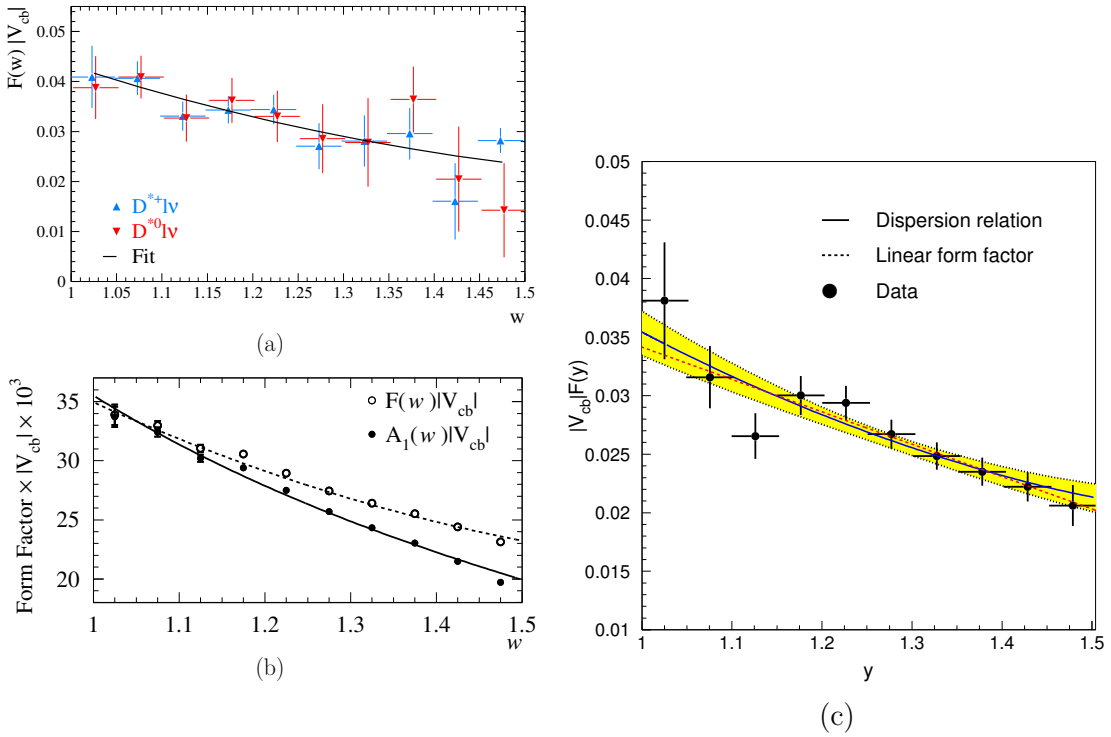

Figure 1.8: **(a)** CLEO 2002 [18] latest result on $\mathcal{F}(w)|V_{cb}|$. CLEO analysis use $B^0 \to D^{*-}\ell^+\nu_\ell$ (blue triangle) and $B^\pm \to D^{*0}l^\pm\nu$ (red triangle) data sample. The result of their fit if $\mathcal{F}(1)|V_{cb}| = (4.31 \pm 0.13(stat) \pm 0.18(syst)) \times 10^{-2}$ and using the value $\mathcal{F}(1)$ in 1.42 they extracted $|V_{cb}| = (4.69 \pm 0.14(stat) \pm 0.20(syst) \pm 0.18(theor)) \times 10^{-2}$. **(b)** *BABAR* 2004 [20] result on $\mathcal{F}(w)|V_{cb}|$ using only the decay $B^0 \to D^{*-}\ell^+\nu_\ell$. Using the value $\mathcal{F}(1)$ in 1.43 they extracted $|V_{cb}| = (3.87 \pm 0.03(stat) \pm 0.17(syst)^{+1.5}_{-1.3}(theor)) \times 10^{-2}$. **(c)** BELLE result [19] on $\mathcal{F}(w)|V_{cb}|$ using only the decay $B^0 \to D^{*-}\ell^+\nu_\ell$ and its charge-conjugate. The result of their fit if $\mathcal{F}(1)|V_{cb}| = (3.358 \pm 0.19(stat) \pm 0.18(syst)) \times 10^{-2}$ and using the value $\mathcal{F}(1)$ in 1.42 they extracted $|V_{cb}| = (4.19 \pm 0.45(stat) \pm 0.53(syst) \pm 0.30(theor)) \times 10^{-2}$. Their notation adopts y instead of w.

Averaging the corrected measurements the PDG [4] quotes:

$$\mathcal{F}(1)|V_{cb}| = (38.2 \pm 0.5 \pm 0.9)^{-3} \tag{1.44}$$

$$\rho^2 = 1.56 \pm 0.05 \pm 0.13 \tag{1.45}$$

The error ellipses for the corrected measurements and for the world average are shown in Fig.1.9 [23]. Using the value for $\mathcal{F}(1) = 0.91 \pm 0.04$ [22], PDG [4] calculates $|V_{cb}|$ from exclusive semileptonic $B^0 \to D^{*-}\ell^+\nu_\ell$ to be:

$$|V_{cb}| = (42.0 \pm 1.1_{exp} \pm 1.9_{theo}) \times 10^{-3} \tag{1.46}$$

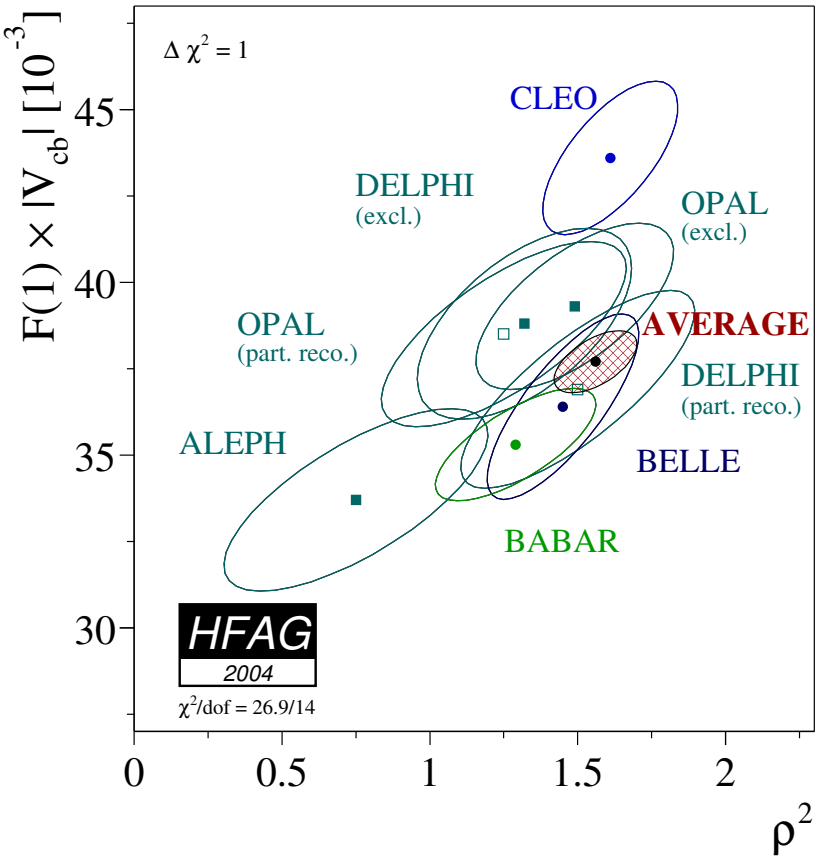

Figure 1.9: The error ellipses for the corrected measurements and world average for $\mathcal{F}(1)|V_{cb}|$ versus ρ^2. The ellipses are obtained from product between the 1 σ error of $\mathcal{F}(1)|V_{cb}|$, ρ^2 and the correlation between the two [23].

Chapter 2

The *BABAR* detector

2.1 Introduction

The PEP-II B Factory[24] is an asymmetric e^+e^- collider designed to operate at a luminosity of $3 \times 10^{33}\ \mathrm{cm}^{-2}\mathrm{s}^{-1}$ and beyond at a center-of-mass energy of $10.58\,\mathrm{GeV}$, the mass of the $\Upsilon(4S)$ resonance (see figure 2.1). This resonance decays almost exclusively into $B^0\overline{B}^0$ or B^+B^- pairs and thus provides an ideal laboratory for the study of B mesons. In PEP-II, the electron beam of $9.0\,\mathrm{GeV}$ collides head-on with the positron beam of $3.1\,\mathrm{GeV}$ resulting in a boost to the $\Upsilon(4S)$ resonance of $\beta\gamma = 0.56$. This boost makes it possible to reconstruct the decay vertices of the two B mesons and to determine their relative times. One can therefore measure the decay time dependence of decay rates. The crucial test of *CP* invariance is a comparison of these rates for B^0 and $\overline{B}^0$ to a *CP* eigenstate. Experimentally this requires events in which one B meson decays to a *CP* eigenstate is fully reconstructed and the other B meson is tagged as B^0 or as $\overline{B}^0$ by its decay products, a charged lepton, a charged kaon or a D^* decay. The very small branching ratios of B mesons to *CP* modes, typically 10^{-4}, and the need for full reconstruction of final states with two or more charged particles and several π^0 plus the tagging of the second B place stringent requirements on the detector.

2.1.1 Physics requirements

Several requirements are needed to achieve the goal of performing accurate *CP* violation measurements:

- a large and uniform acceptance, in particular down to small polar angles relative to the boost direction, to avoid particle losses;
- excellent detection efficiency for charged particles down to $60\,\mathrm{MeV}$ and for photons to $25\,\mathrm{MeV}$;
- high momentum resolution to separate small signals from background;

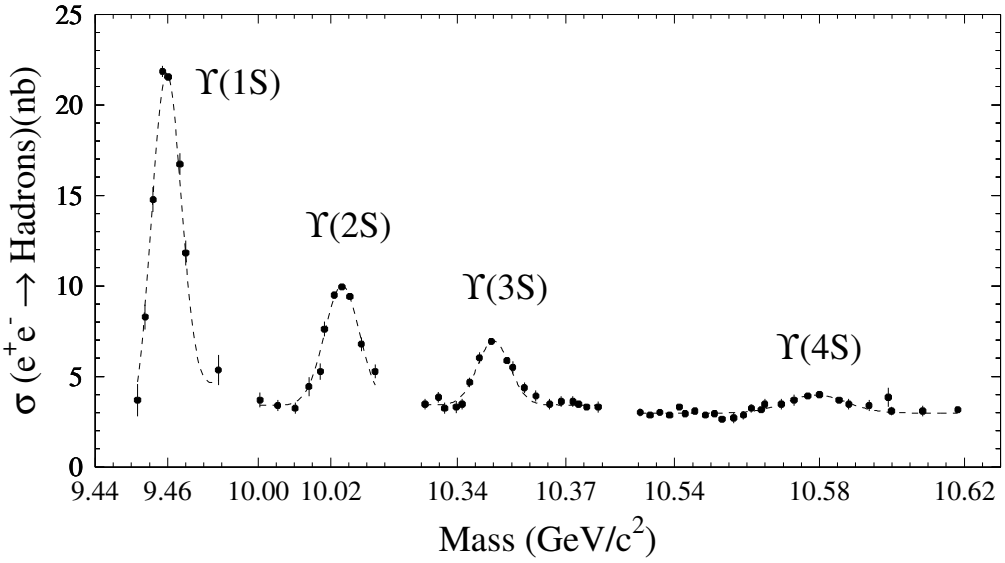

Figure 2.1: The first four S-wave Υ resonances shown with the hadronic cross section versus center-of-mass energy/c^2 in the Υ mass region. The $\Upsilon(4S)$, at 10.58 GeV/c^2, is the third radial excitation of the ground state. It has sufficient mass to decay into $B^0\overline{B}^0$ and B^+B^- pairs, which results in its larger width. Note the difference in resonance amplitude between the $\Upsilon(4S)$ and the lower resonances and the significant continuum background. The continuum events underneath the $\Upsilon(4S)$ typically have a two-jet topology, which allows them to be distinguished from the much more isotropic distribution of tracks in the $\Upsilon(4S) \to B\overline{B}$ decays.

- excellent energy and angular resolution for the detection of photons from π^0 and radiative B decays in the range from $25\,\mathrm{MeV}$ to $4\,\mathrm{GeV}$;
- very good vertex resolution, both transverse and parallel to the beam;
- identification of electrons and muons over a range of momentum, primarily for the detection of semi-leptonic decays used to tag the B flavor and for the study of semi-leptonic and rare decays;
- identification of hadrons over a wide range of momentum for B flavor tagging as well as for the separation of pions from kaons in decay modes like $B^0 \to K^\pm\pi^\mp$ and $B^0 \to \pi^+\pi^-$ as well as in charm meson and τ decays;
- a highly efficient, selective trigger system with redundancy so as to avoid significant signal losses and systematic uncertainties;

2.1.2 B Factoryrequirements

To reach the desired sensitivity for the most interesting measurements, data sets of some 10^8 B mesons will be needed. For the peak cross section at the $\Upsilon(4S)$ of 1.1 fb this will require an integrated luminosity of some $200 - 500$ fb^{-1} which starts to be compatible with the actual *BABAR* recorded luminosity shown in Fig.2.2. Targeting to collect such a huge amount of data requires the collider to work with few interruptions or shutdown periods. The main requirements for the B-factory are then:

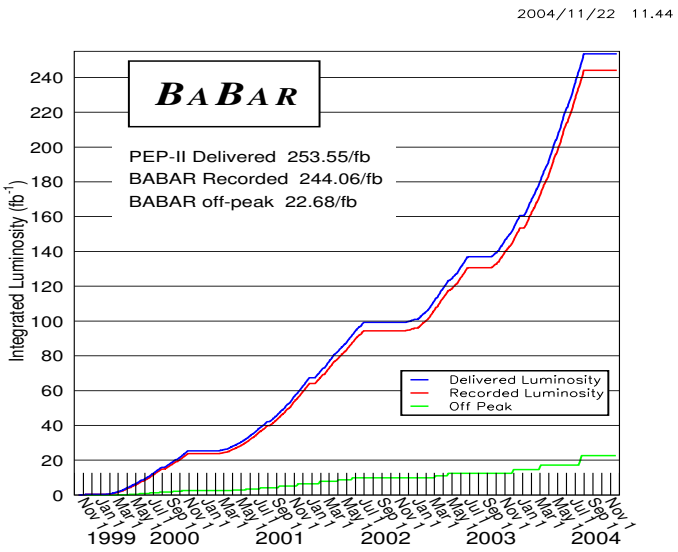

Figure 2.2: PEP-II delivered and *BABAR*-recorded integrated luminosity in RUN1 and RUN4 (from October 1999 to July 2004).

- low noise electronics and data acquisition systems of high flexibility and operational stability;
- high degree of reliability of components and frequent monitoring and automated calibrations, plus control of the environmental conditions to assure continuous and stable operation;
- an on-line computing and network system that can control, process, and store the expected high volume of data;
- detector components that can tolerate significant doses of radiation and operate under high background condition.

2.2 PEP-II

PEP-II is an e^+e^- storage ring system designed to operate at a center of mass energy of $10.58\,\mathrm{GeV}$, corresponding to the mass of the $\Upsilon(4S)$ resonance. The parameters of these energy asymmetric storage rings are presented in table 2.1. PEP-II has surpassed its design luminosity, both in terms of the instantaneous and the integrated daily luminosity, with significantly fewer bunches than

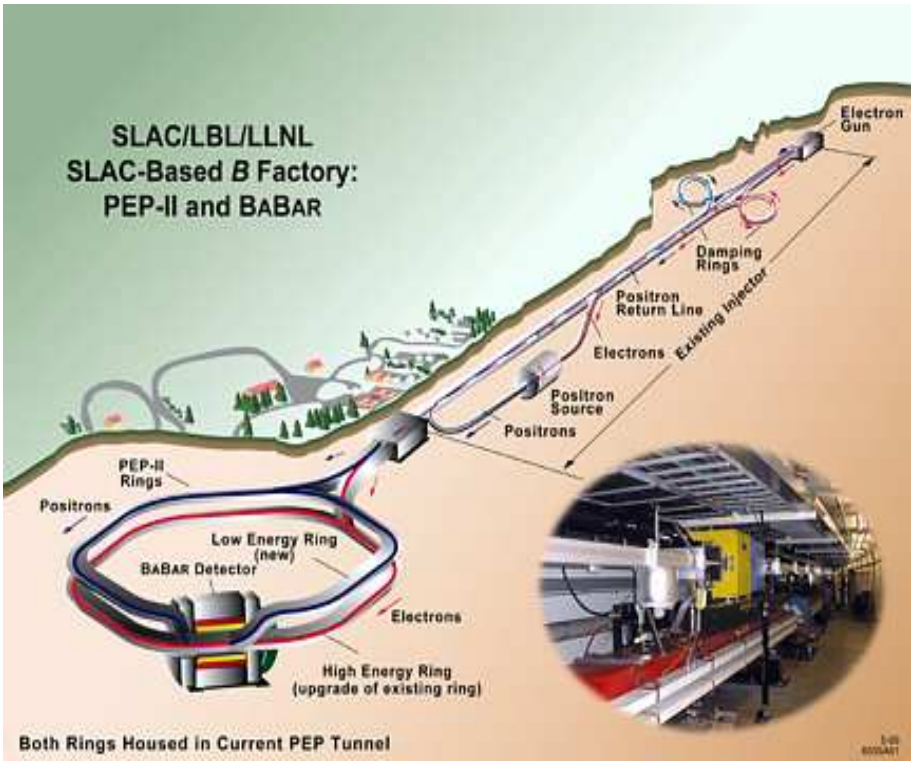

Figure 2.3: PEP-II overview.

anticipated. PEP-II typically operates in a series of 40 minutes fills during which the colliding beams coast. At the end of each fill, it takes about three to five minutes to replenish the beams for the next fill. After a loss of the stored beams, it takes approximately 15 minutes to refill the two beams. *BABAR* divides the data into runs, defined as periods of about two hours duration or less during which beam and detector conditions are judged to be stable. While most of the data are recorded at the peak of the $\Upsilon(4S)$ resonance, some 11% are taken 40 MeV below to allow for studies of the non-resonant background [1].

In order to reduce the dead time due to refill the beams a new approach to keeping the rings full was adopted at the beginning of December 2003, known as trickle injection. The trickle injection scheme in the positron ring adds tiny pulses of particles as soon as the buckets begin to be depleted, maintaining the beam at full brightness around the clock. This approach has a double advantages for data taking: the collision rate does not fall off and, since the detector is desensitized for much less time, it can record up to 20%-30% more events.

[1] mostly from $e^+e^- \to q\overline{q}$ or $e^+e^- \to \ell^+\ell^-$.

Parameters	Units	Design	Typical
Energy HER/LER	GeV	9.0/3.1	9.0/3.1
Current HER/LER	A	0.75/2.15	1.0/1.7
# of bunches		1658	553-829
Bunch spacing	ns	4.2	6.3-10.5
σ_x	μm	110	147
σ_y	μm	3.3	5.6
σ_z	mm	9	9
Luminosity	pb$^{-1}/day$	135	~ 500

Table 2.1: PEP-II beam parameters; values are given both for design and typical colliding beam operation in the first year. HER and LER refer to the high energy e^- and low energy e^+ ring, respectively. σ_x, σ_y and σ_z refer to the horizontal, vertical, and longitudinal r.m.s. size of the luminous region.

2.2.1 Interaction region

PEP-II collides the bunches head-on to avoid the coupling of transverse and longitudinal modes caused by the crossing angle which can limit its luminosity. The energy asymmetry allows to separate the beams magnetically but it is not possible to use different focusing optics for the two beams. The higher energy beam (HER) has indeed more focusing than the other with equal currents, that would result in an asymmetric focusing. To compensate this and obtain a symmetric focusing, the lower energy beam has been designed to have a higher current. It is usually more difficult [25] to obtain a high current electron beam with respect to a positron beam because the positive ions that remain in the beam pipe are attracted by the electron beam and can generate orbit instabilities. This is indeed the reason why the electron beam has been chosen to have the lower current (and the higher energy). However PEP-II experts [25] claim that with the present working conditions the positron beam (the one with higher current) becomes instable at high currents because of a multiplication effect of electrons extracted from the walls of the beam pipe. The large beam currents and the necessity to separate closely-spaced bunches as close as possible to the interaction point (IP), tightly couple the issues of detector design, interaction region layout, and remediation of machine induced background. The bunches are separated magnetically in the horizontal plane by a pair of dipole magnets (B1), followed by a series of offset quadrupoles. The tapered B1 dipoles, located at ± 21 cm on either side of the IP, and the Q1 quadrupoles operate inside the field of the *BABAR* solenoid, while Q2, Q4, and Q5, are located outside or in the fringe field of the solenoid. The interaction region is closed by a water-cooled beam pipe consisting of two thin layers of beryllium (0.83 mm and 0.53 mm) with a 1.48-mm water channel in between. To attenuate synchrotron radiation, the inner surface of the pipe is gold-plated (approximately 4 μm). In addition, the beam pipe is wrapped with 150 μm Ta foil on either side of the IP, i.e., beyond $z = +10.1$ cm and $z = -7.9$ cm. The total thickness of the central beam pipe section at normal incidence corresponds to 1.06 % of a radiation length. The beam pipe, the permanent

magnets and the Silicon Vertex Tracker (SVT) are assembled and aligned and then enclosed in a 4.4-m long support tube. This rigid structure is inserted into the *BABAR* detector, spanning the IP.

2.3 Luminosity, Beam Energies and Position

The beam parameters that are most critical for the *BABAR* data analysis are the luminosity, the energies of the two beams and the position and size of the luminous region.

2.3.1 Luminosity

While PEP-II uses a high-rate process by sampling radiative Bhabha scattering to provide a fast relative measurement of the luminosity for machine operations, *BABAR* derives the absolute luminosity off-line from other QED processes. The best result is obtained from $\mu^+\mu^-$ pairs. For a sample of 1 fb^{-1}, the statistical error is 1.3 % compared to a systematic error of 0.5 % on the relative, and 1.5 % on the absolute value of the luminosity. This error is currently dominated by uncertainties in the Monte Carlo generator and the simulation of the detector. It is expected that with a better understanding of the efficiency the overall systematic error on the absolute value of the luminosity can be reduced by a factor two [26].

2.3.2 Beam Energies

During operation, the mean energies of the two beams are calculated from the total magnetic bending strength (including the effects of off-axis quadrupole fields, steering magnets, and wigglers) and the beam orbits. While the systematic uncertainty in the PEP-II calculation of the absolute beam energies is estimated to be $5 - 10$ MeV, the relative energy setting for each beam is accurate and stable to about 1 MeV [25]. The energy spread of the LER and HER is 2.3 MeV and 5.5 MeV [25], respectively. To ensure that data are recorded close to the peak of the $\Upsilon(4S)$ resonance, the observed ratio of $B\overline{B}$ enriched hadronic events to lepton pair production is monitored on-line. At the peak of the resonance, a 2.5 % change in the $B\overline{B}$ production rate corresponds to a 2 MeV change in the c.m. energy, a value that is close to the tolerance to which the energy of PEP-II can be held. However, a drop in the $B\overline{B}$ rate does not distinguish between energy settings below or above $\Upsilon(4S)$ peak. The sign of the energy change must be determined from other indicators. The best monitor and absolute calibration of the c.m. energy is derived from the measured c.m. momentum of fully reconstructed B mesons constrained with the known B meson mass. An absolute error of 1.1 MeV can be obtained for an integrated luminosity of 1 fb^{-1}. This error is equally limited by the knowledge of the B mass [27] and the detector resolution.

2.3.3 Beam Size and Position

The size and position of the luminous region are critical parameters for the time-dependent analyses[2] and their values are monitored continuously on-line and off-line. The design values for the size of the luminous region are presented in table 2.1 above. The vertical size is too small to be measured directly. It is inferred from the measured luminosity, the horizontal size, and the beam currents; it varies typically by 1-2 μm. The transverse position, size and angles of the luminous region relative to the *BABAR* coordinate system are determined by analyzing the distribution of the distance of closest approach to the z-axis of the tracks in well measured two-track events as a function of the azimuth ϕ. The longitudinal parameters are derived from the longitudinal vertex distribution of the two tracks. The uncertainties in the average beam position are of the order of a few μm in the transverse plane and about 100 μm along the collision axis. Run-by-run variations in the beam position are comparable to these measurement uncertainties, indicating that the beams are stable over the period of a typical run. The measured horizontal and longitudinal beam sizes, corrected for tracking resolution, are consistent with those measured by PEP-II.

2.4 Detector overview

The *BABAR* detector (Fig.2.5) has been designed and built by a collaboration of about 600 physicists of 75 institutions from 10 countries and installed at SLAC in Fall 1998. First data with PEP-II colliding beams were collected in May 1999. The *BABAR* superconducting solenoid which produces a field of 1.5 T axial magnetic field contains a set of nested detectors: a five layers Silicon Vertex Tracker (SVT), a central Drift Chamber (DCH) for charged particles detection and momentum measurement, a quartz-bar Čerenkov radiation detector (DIRC) for particle identification, and a CsI crystal electromagnetic calorimeter for detecting photons and electrons. The calorimeter has a barrel and an endcap which extends it asymmetrically into the forward direction (e^- beam direction), where many of the collision products emerge. All the detectors located inside the magnet have full acceptance in azimuth.

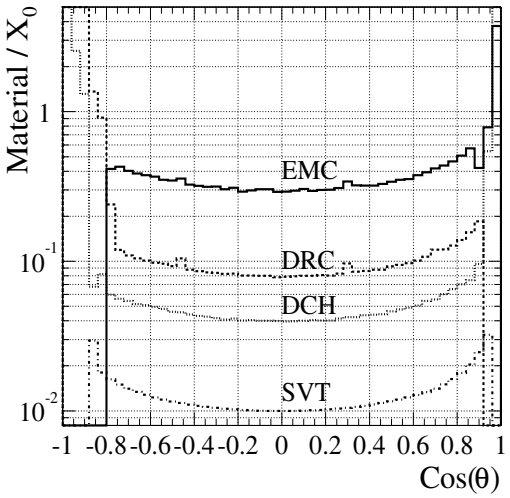

Figure 2.4: Amount of material (in units of radiation lengths) which a high energy particle, originating from the center of the coordinate system at a polar angle θ, traverses before it reaches the first active element of a specific detector system.

[2] or whenever a primary decay vertex is evaluated with the beam-spot constraint.

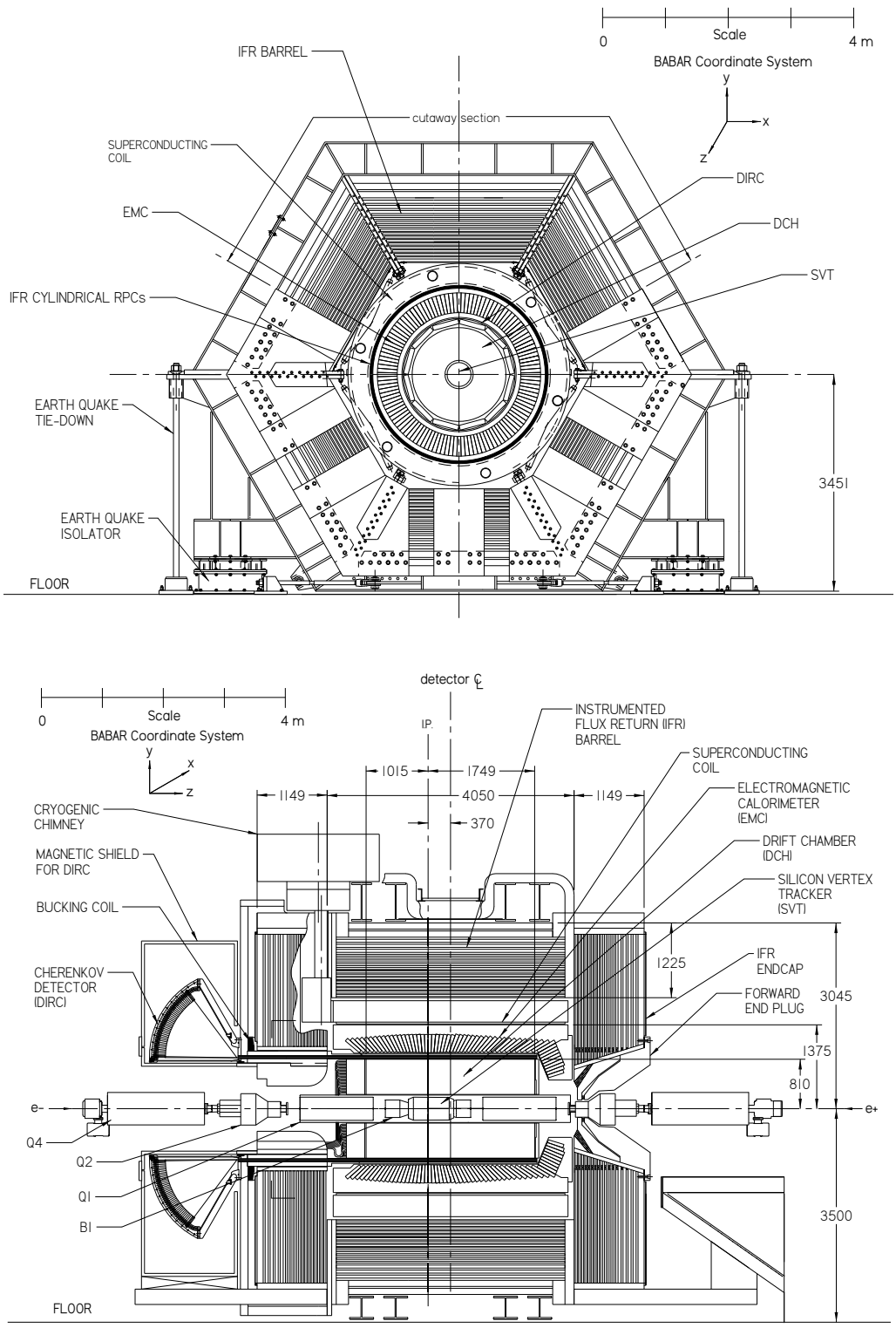

Figure 2.5: *BABAR* detector front view (top) and side view (bottom).

The flux return outside the cryostat is composed of 18 layers of steel, which increase in thickness outwards, and are instrumented with 19 layers of planar RPCs in four sextants and with 12 layers of LSTs in the other two sextants in the barrel and 18 layer of RPCs in the end-caps. The RPCs/LSTs allow the separation of muons and charged hadrons, and also detect penetrating neutral-hadrons. Since the average momentum of charged particles produced in B meson decay is less than 1 GeV, the errors on the measured track parameters are dominated by multiple Coulomb scattering, rather than the intrinsic spatial resolution of the detectors. Similarly, the detection efficiency and energy resolution of low energy photons are severely impacted by material in front of the calorimeter. Thus, special care has been given to keep the material in the active volume of the detector to a minimum. Figure 2.4 shows the distribution of material in the various detector systems in units of radiation lengths. Specifically, each curve indicates the material a particle traverses before it reaches the first active element of a specific detector system.

2.5 Tracking system

The *BABAR* tracking system is composed by two different components: the silicon vertex tracker (SVT) and the drift chamber (DCH).

2.5.1 Silicon vertex detector

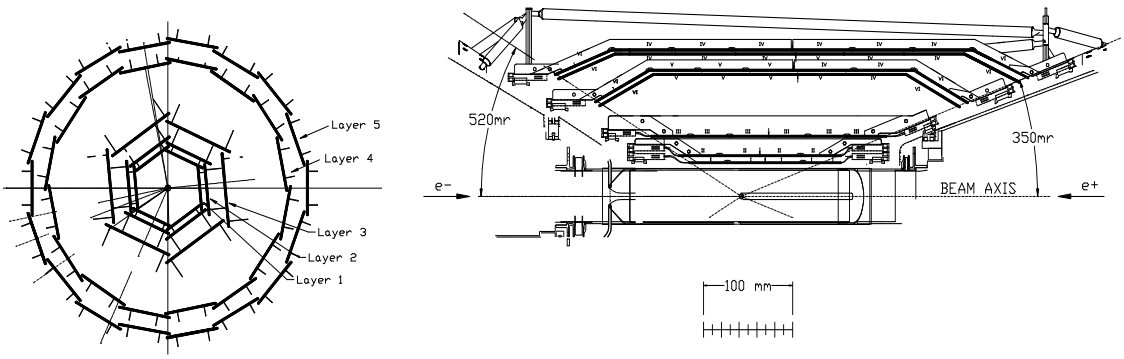

(a) (b)

Figure 2.6: (a) SVT schematic front view, (b) SVT side view.

The silicon vertex tracker (SVT) is used to measure B meson decay vertices. Given the very high resolution achieved on z coordinate ($\sim 110\ \mu m$) this system has the main role in CP asymmetries studies; moreover this is the only detector that can track charged particles with low transverse momentum ($p_T < 120\ \mathrm{MeV}$), that have not enough energy to enter and be detected in the DCH. The SVT layout has been optimized by considering the limitations due to the

PEP-II geometry near the interaction region, namely from the two B1 permanent magnets that split the beam after the collisions. The SVT is the innermost detector and a large technological effort has been put in place in order to make it as radiation hard as possible and, at the same time, with minimum material thickness, in order to reduce multiple scattering. The structure is based on 52 double faced silicon modules, read by low noise front-end electronics. These modules are organized in 5 radial layers: the first three are dedicated to tracking and vertex reconstruction, while the other remaining two are contributing to low energy particle tracking (Fig.2.6). Modules are placed on a carbon-fiber conic structure placed around B1 permanent magnets and beam-pipe. All the SVT and accelerator focusing elements are kept inside a beryllium support that is directly bound to the beam-line mechanical structure. The amount of radiation absorbed by silicon is constantly monitored by a 12 photodiodes system placed nearby the first SVT layer. The SVT acceptance in the polar angle θ is limited by beam-line elements and is $-0.87 < \cos\theta_{lab} < 0.96$.

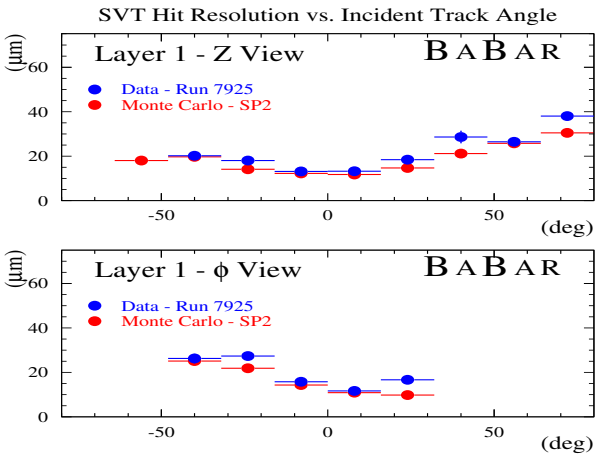

Figure 2.7: SVT single hit resolution (inner layer) as a function of track incidence angle.

2.5.2 Drift chamber (DCH)

The Drift Chamber (DCH) is the main tracking device for charged particles with transverse momenta p_T above $\sim 120\,\mathrm{MeV}$, providing the measurement of p_T from the curvature of the particle traversing the 1.5 T magnetic field. For low momentum particles, the DCH provides particle identification by measurement of ionization loss ($\mathrm{d}E/\mathrm{d}x$). For the helium-isobutane gas mixtures under consideration, a resolution of around 7 % has been attained for the $\mathrm{d}E/\mathrm{d}x$ measurement, allowing π/K separation up to 700 MeV. This capability is complementary to the DIRC in the barrel region, while in the extreme backward and forward directions where there is no dedicated particle identification device, it is the only available device for particle identification. The DCH also allows the reconstructions of secondary vertices, such as decays of K^0_S outside the silicon detector volume. For this purpose, the chamber is able to measure not only the transverse coordinate, but also the longitudinal position of tracks with good ($\sim 1\,\mathrm{mm}$) resolution. Good z resolution also aids in matching DCH and SVT tracks, and in projecting tracks to the DIRC and the calorimeter. Finally, single cell hit information is used for the first level trigger. The Drift Chamber, illustrated in Fig.2.8, consists of a 280 cm-long cylinder with an inner radius of 23.6 cm and an outer radius

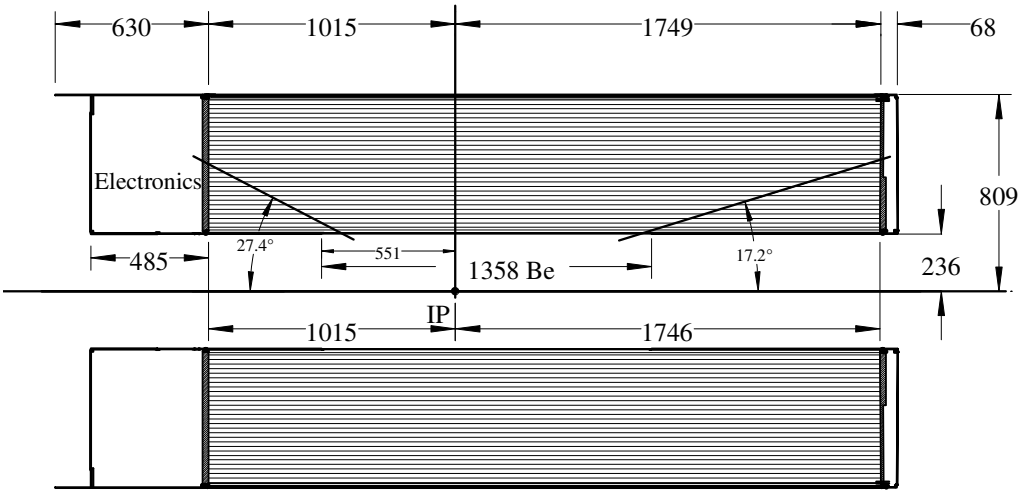

Figure 2.8: *BABAR* Drift Chamber side view.

of 80.9 cm. The DCH is located within the volume inside the DIRC and outside the PEP-II support tube. The center of the chamber is displaced forward by 36.7 cm to improve the forward track length, given PEP's asymmetric boost.

The drift system consists of 7104 hexagonal cells (figure 2.9(a)), approximately 1.8 cm wide by 1.2 cm high, arranged in 40 concentric layers between a radius of 25.3 and 79.0 cm. The active volume provides charged particle tracking over the polar angle range $-0.92 < \cos\theta_{lab} < 0.96$. The 40 layers are grouped into 10 superlayers[3] of 4 layers each, organized with the same orientation for sense and field wires within a given superlayer. Superlayers alternate in orientation, first axial, then a small stereo positive angle, followed by a small stereo negative angle in order to measure also the z coordinate. All superlayers participate in the L1 track finding.

Single cells are made of a tungsten central sense wire working at $1900 \div 1960$ V, surrounded by 6 aluminum wire cathodes (Fig.2.9(b)). The DCH uses, to minimize multiple scattering, a 80%-20% gas mixture of Helium and Isobutane, with a tiny amount of water vapor (3000 ppm) added in order to extend the detector lifetime in presence of high radiation. The mean spatial resolution for a single cell, obtained from all charged tracks in hadronic events is $\sim 125\,\mu\mathrm{m}$ (the design value being $\sim 140\,\mu\mathrm{m}$), as shown in Fig.2.10(a). The chamber hit timing information is reconstructed using TDCs, while flash-ADC are used to monitor the shape of pulse signal as function of time; both information are used to reconstruct the energy deposit inside the cells. The calibration to find corrections for the gain factor is done by injecting a known amount of charge.

[3]Cylindrical layers of cells are grouped four at a time into superlayers. The first 16 layers are shown in Fig.2.9(a). The plus signs, open circles, filled circles and crosses denote sense wires, field wires, guard wires and clearing wires, respectively. Lines have been added between field wires to aid in visualization of the cells. The numbers on the right side give the stereo angles (mrad) of sense wires in each layer. A 1 mm thick beryllium inner cylinder is shown inside the first layer.

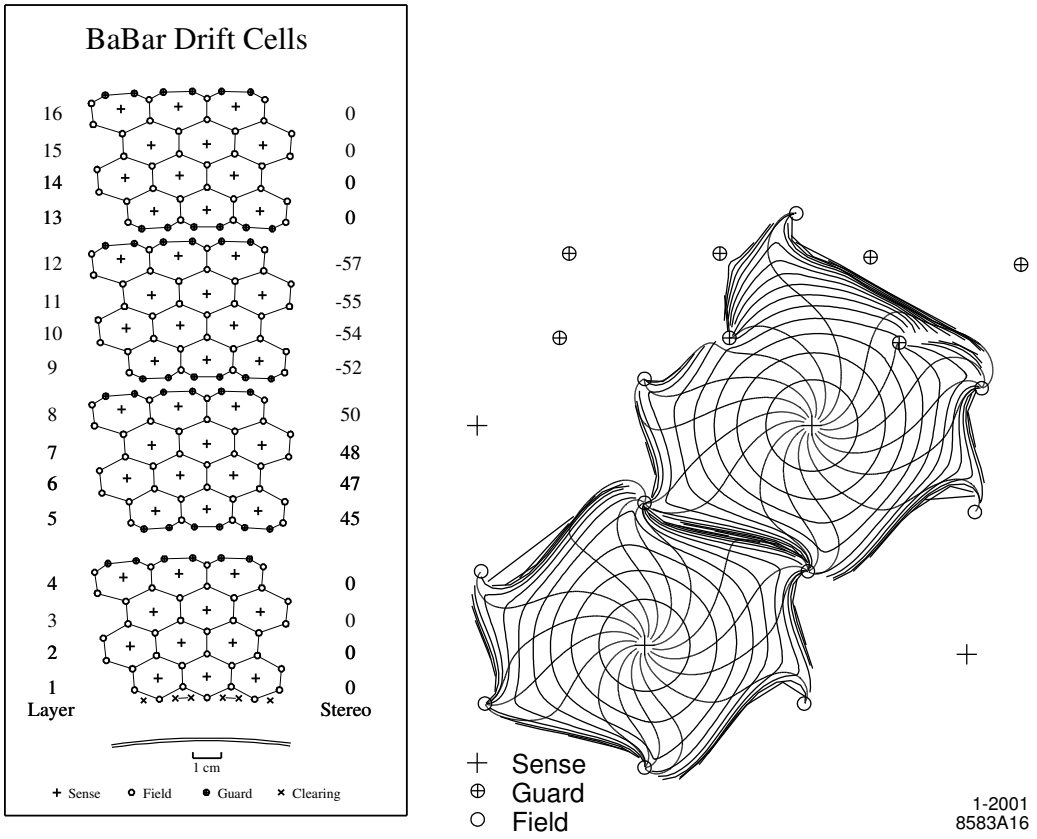

(a) (b)

Figure 2.9: (a) Drift cell configuration of DCH. (b) Isochronal curves for layers 3 and 4 of an axial super-layer are shown: almost round near by the sense wires, they are highly distorted near by field wires.

The p_T resolution is directly related to the resolution of the curvature of the track, and it is well represented by the following linear function (Fig.2.10(b)):

$$\frac{\sigma p_T}{p_T} = (0.13 \pm 0.01)\% \times p_T(\text{ GeV}) + (0.45 \pm 0.03)\% \tag{2.1}$$

The $\mathrm{d}E/\mathrm{d}x$ resolution is computed comparing the measured $\mathrm{d}E/\mathrm{d}x$ with the expected value for *Bhabha* electrons. Fig.2.11(a) shows the distribution of $(dE/dx_{meas} - dE/dx_{exp})\,/dE/dx_{exp}$ from which we obtain the mean $\mathrm{d}E/\mathrm{d}x$ resolution to be 7.5 %, while Fig.2.11(b) shows the distribution of the reconstructed and corrected $\mathrm{d}E/\mathrm{d}x$ from DCH as function of track momenta, with Bethe-Block curves superimposed for individual particle species.

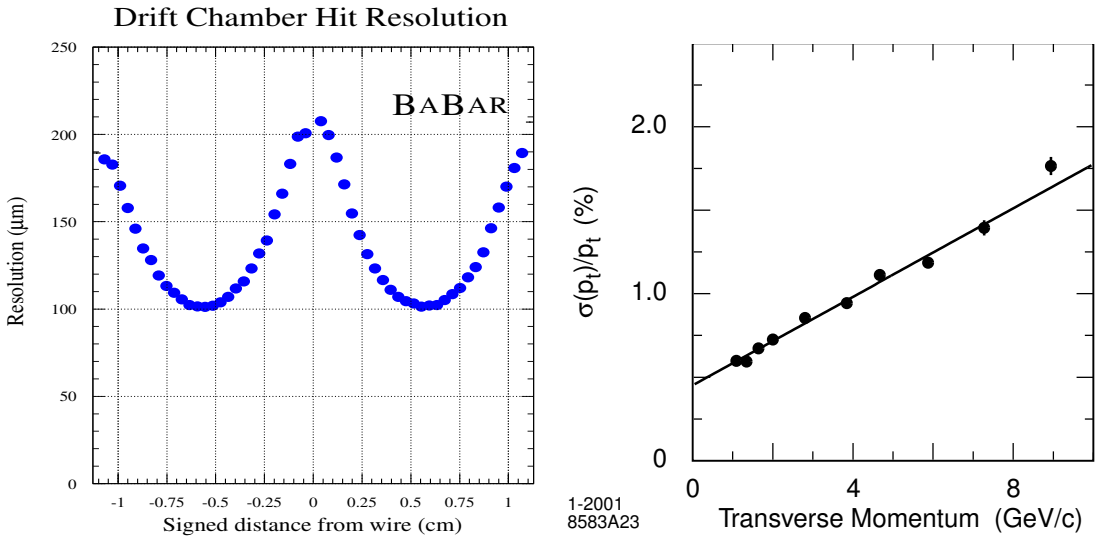

(a) (b)

Figure 2.10: (a) DCH single hit resolution. (b) DCH p_T resolution determined from cosmic rays.

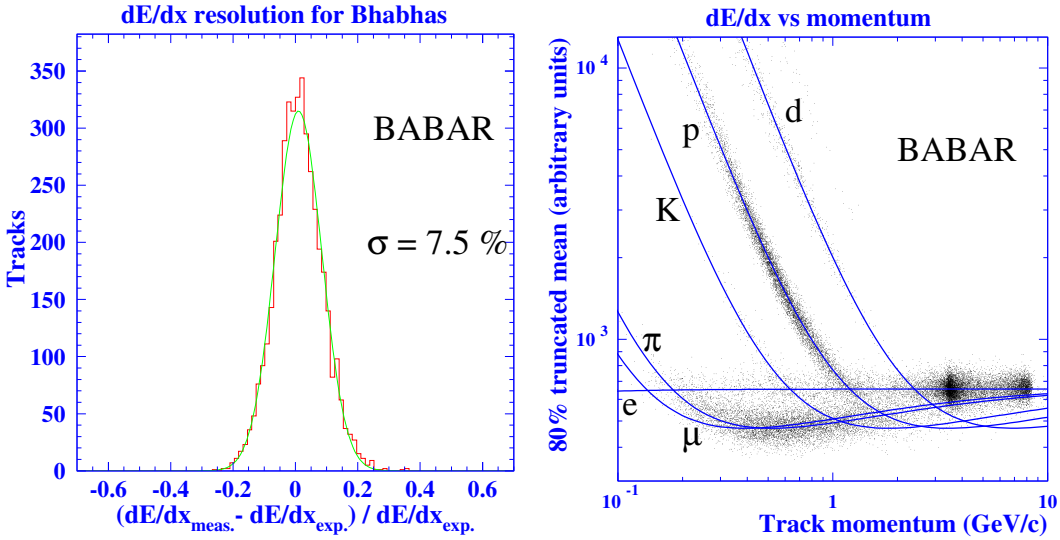

(a) (b)

Figure 2.11: (a) DCH $\mathrm{d}E/\mathrm{d}x$ resolution for *Bhabha* electrons. (b) DCH $\mathrm{d}E/\mathrm{d}x$ as a function of track momentum.

2.6 Čerenkov light detector

In *BABAR* the particle discrimination between π and K is mainly performed by a detector named DIRC (Detector of Internally Reflected Čerenkov light). The particle identification is based on the measurements of the Čerenkov light produced in quartz. Fig.2.12 show the schematic 3-D view of the DIRC. This detector is placed outside the DCH and before the EMC and it is designed

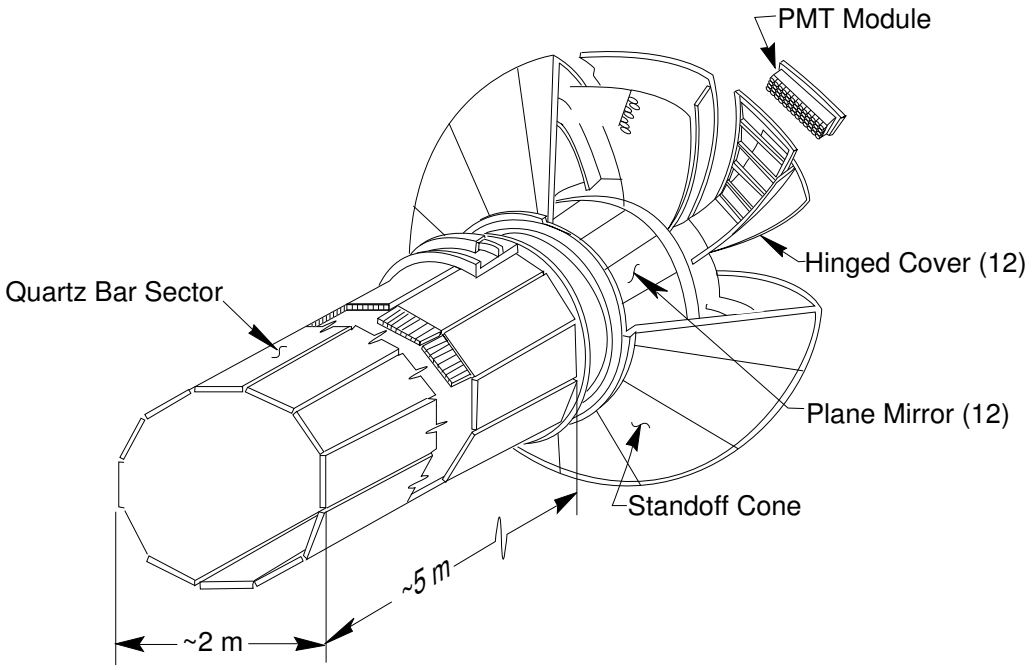

Figure 2.12: 3-D view of DIRC.

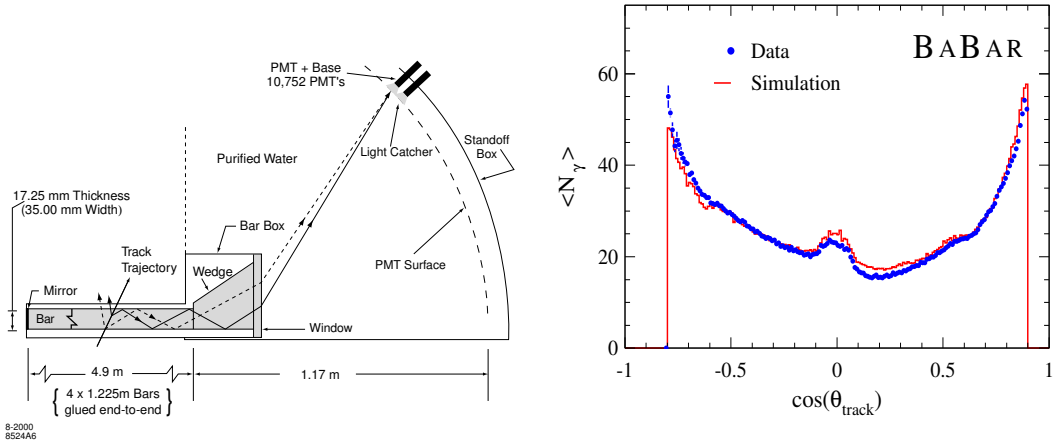

(a) (b)

Figure 2.13: (a) Schematics of the DIRC fused silica radiator bar and imaging region. (b) Number of detected photoelectrons versus track polar angle for reconstructed di-muon events in data and simulation.

to be thin and uniform in term of radiation length in order to minimize the effects on particles that cross it, therefore allowing to minimize the volume and energy resolution of the EMC. The angular coverage of DIRC is $-0.84 < \cos\theta_{lab} < 0.90$, which corresponds to the 87% of the solid angle in the center of mass system. A non-conventional feature of the DIRC is the usage of quartz bars both as light radiator and light guide. The DIRC is composed by a matrix of 144 quartz

bars, placed on a polygon of 12 sides. Each bar is $\sim$ 17 mm thick, $\sim$ 35 mm large and 4.9 m long (in the direction of z axis). The index of refraction of the quartz bars is $n = 1.473$, which correspond to a photon Čerenkov angle $\cos\theta_c = 1/\beta n$. Charged particles traversing quartz bars above the momentum threshold emit Čerenkov radiation which is transported by total reflection (which preserves angle information) inside the bars to a 10752 photo-multipliers matrix placed outside the *BABAR* magnet return joke, in a region where the magnetic filed is low. The photo-multipliers are placed on a semi-toroidal water tank with an inner radius of 1.2 m and an outer of 3 m. In Fig.2.13(a) a schematic view of the DIRC geometry and of the process of reflection , transmission and detection of the emitted Čerenkov radiation. The angle θ_c is obtained matching

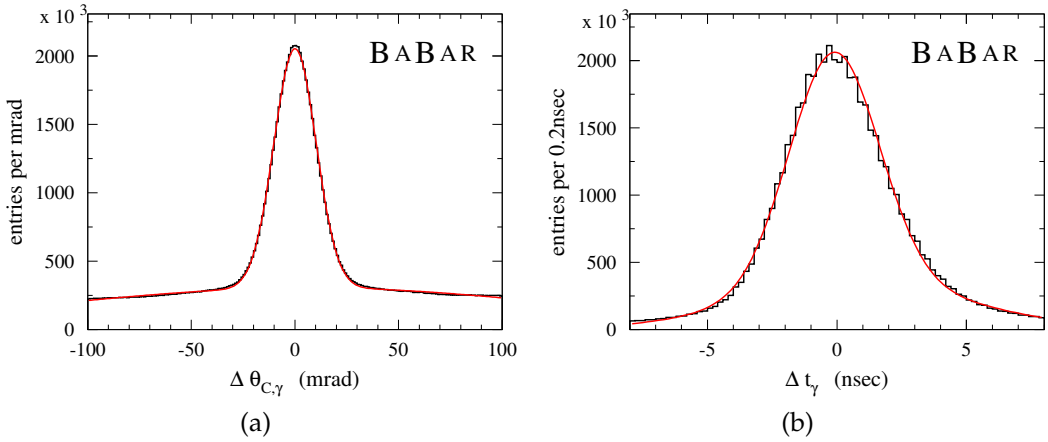

Figure 2.14: (a) Single photon resolution of reconstructed Čerenkov angle. (b) Time distance between measured and expected arrival time.

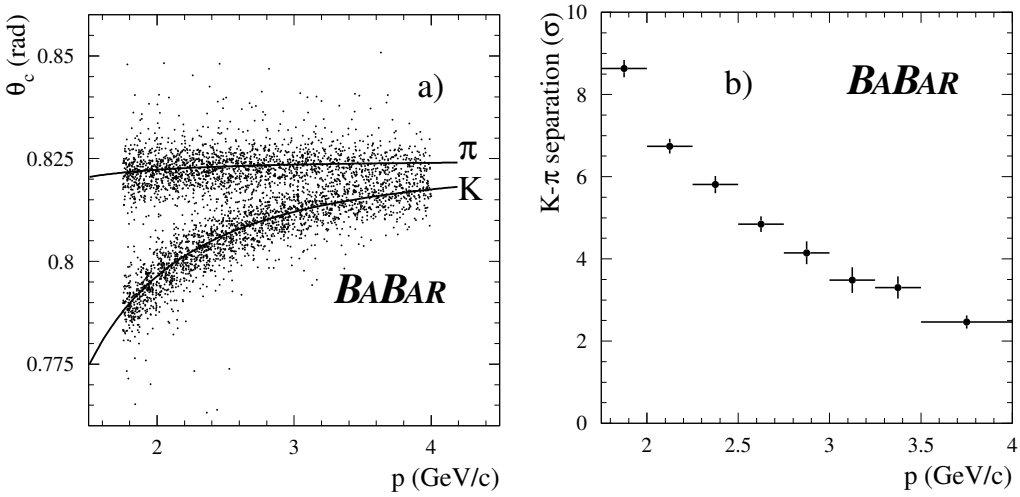

Figure 2.15: (a) Čerenkov angle and (b) $K - \pi$ discrimination power as a function of the momentum for single tracks. Discrimination quoted is computed performing the mean over all the polar angles.

the particle direction obtained by the tracking system and the position of the PMTs that are detecting Čerenkov photons. The information carried by this angle are of fundamental interest for particle identification and in particular for the distinction between charged π and K. The angular resolution for a single photon is $\sim$ 10.2 mrad (Fig.2.14(a)), while the average resolution over the 30 mean photons per track (as shown in Fig.2.13(b)) is reduced at $\sim$ 2.8 mrad. The discrimination between π and K due to the separation between the corresponding Čerenkov angles is greater then 3 standard deviation at about 3 GeV, as shown in Fig.2.15, and higher for lower momenta. Due to the fact that the photons inside the quartz are totally reflected, the association between phototube hits and single track can have more than one solution. These possible ambiguities are solved by measuring the time difference between the hits in phototubes and the expected arrival time of each track with a precision of 1.7 ns (Fig.2.14(b)), which allows to estimate the propagation time for a given Čerenkov angle, and therefore to reduce the background from uncorrelated photons.

2.7 Electromagnetic calorimeter (EMC)

The electromagnetic calorimeter (EMC) is designed to detect photons and electrons with high efficiency in the energy range from 20 MeV to 4 GeV and it provides electron-hadron separation. This energy interval allows to reconstruct low energy π^0 and η particles coming from B decays and other photons and electrons coming from electromagnetic or weak decays. The EMC con-

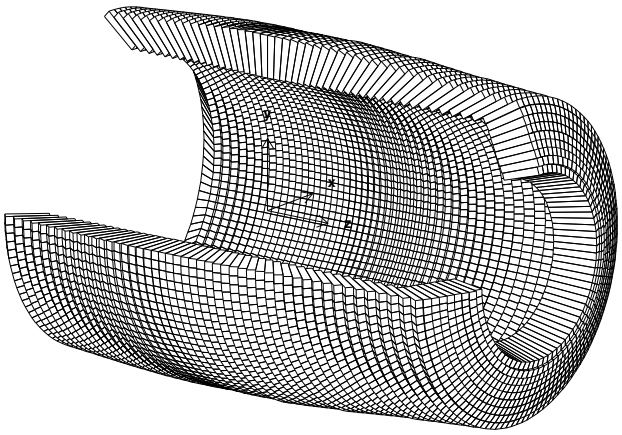

Figure 2.16: The crystal geometry of the Electromagnetic Calorimeter.

sists of 6580 CsI Thallium activated crystal. Each crystal is a truncated trapezoidal pyramid and ranges from 16 to 17.5 radiation length in thickness. The crystals are arranged in a semi-projective barrel structure (inner radius of 90 cm) pointing to the interaction point as shown in Fig.2.16, the structure is divided in 48 θ rows by 120 crystals in azimuth (ϕ). The forward end is closed by a

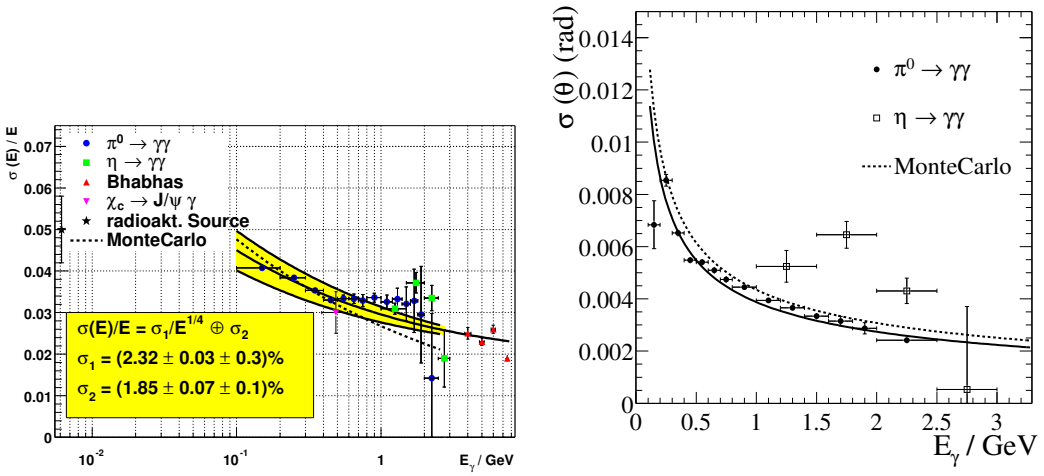

(a) (b)

Figure 2.17: (a) Energy resolution versus energy photon for different calibrations. (b) Angular resolution versus energy photon.

separated structure from the barrel composed by 9 crystal rings. The crystals have typical front and backward dimensions of $\sim 5cm \times 5cm$ and $\sim 6cm \times 6cm$ respectively. Scintillation light is detected by two photodiodes of 2 cm^2 placed on the outer face of the crystal. The covered region of the EMC is $-0.78 < \theta_{lab} < 0.96$. Various calibration systems have been developed for the EMC: 1) a charge pulse is directly injected into the amplifier bound to the photodiodes; 2) light pulses are injected in the backward region of the crystal (*fiber optic/xenon pulser*); and 3) a radioactive liquid that emits 6 MeV photons in each crystal circulates in a dedicated circuit. Data samples of π^0 mesons, radiative (and not) *Bhabha*, $\mu^+\mu^-$ and $\gamma\gamma$ events can be also used for the EMC calibration. The designed energy resolution for EMC is given by:

$$\frac{\sigma(E)}{E(\,\mathrm{GeV})} = \frac{\sigma_1}{(E(\,\mathrm{GeV}))^{1/4}} + \sigma_2 \tag{2.2}$$

where the expected $\sigma_1 \sim 1\%$ and $\sigma_2 \sim 1.2\%$ result to be higher when fitting the results from different methods of calibration as shown in Fig.2.17(a), in fact they result to be: $\sigma_1 = (2.32 \pm 0.03)\%$ and $\sigma_2 = (1.85 \pm 0.07)\%$. These differences come from cross talk effects on the electronic readout. As it is possible to see from Fig.2.17(a), the energy resolution ranges between 2% and 6%. The designed angular resolution is:

$$\frac{\sigma_{\theta,\phi}}{E(\,\mathrm{GeV})} = \frac{\sigma_1}{\sqrt{E(\,\mathrm{GeV})}} + \sigma_2 \tag{2.3}$$

ranging between 3 and 10 mrad (Fig.2.17(b)).

Electron-hadron separation is accomplished by using the shower energy, its lateral moments and the incident track parameters. The comparison of shower energy and incident momentum

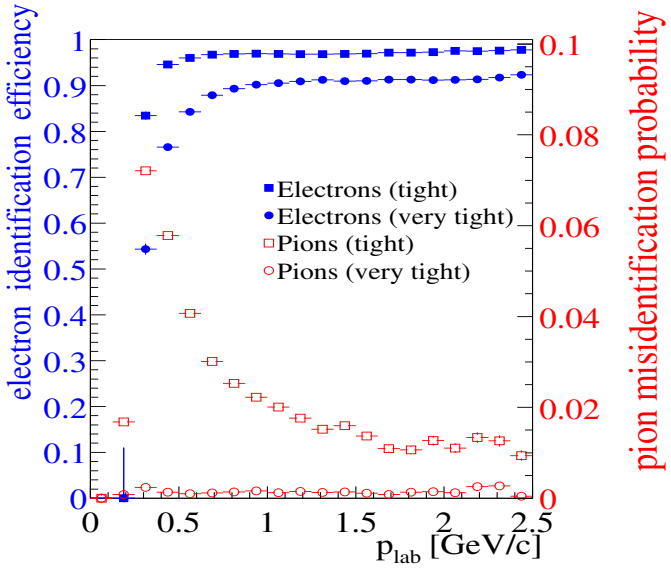

Figure 2.18: The electron efficiency and pion mis-identification rate for different momenta.

(E/p) is the most significant separation variable. Figure 2.18 shows the electron efficiency and pion misidentification rate for different momenta using two different selection algorithms which incorporate EMC and DCH information. The efficiency of electron identification is measured using electrons from radiative Bhabhas and $\gamma\gamma \to e^+e^-$ events. The pion misidentification probability is measured in three prong τ decays. The very tight selector has an efficiency of 90.8% with an average pion misidentification of 0.2%. The electron-hadron separation power meets design expectations.

2.8 Muon detector (IFR)

The IFR (Instrumented Flux Return) has the function of muon an neutral hadron (mainly K_L^0) identification. The detector is obtained instrumenting the gaps of the iron yoke for the magnet flux return with particle detectors. Also the two endcaps that close the magnetic circuit are instrumented. In Fig.2.19 we show the barrel and the two endcaps. The IFR is the outermost detector of *BABAR*. Until summer 2004 the entire IFR was instrumented with Resistive Plate Chambers (RPC) [28]. Due to decreasing efficiencies of the RPCs various improvements were implemented. The RPCs in the forward endcap, which is the region with the highest machine background, were replaced with new RPCs in summer 2001, while in summer 2004 two sextants of the barrel were replaced with Limited Streamer Tubes (LST). The remaining four sextants will be replaced in early 2006. The LST project will be treated in more detail in Chapter 3. In the following, we will describe the four barrel sextants instrumented with RPCs.

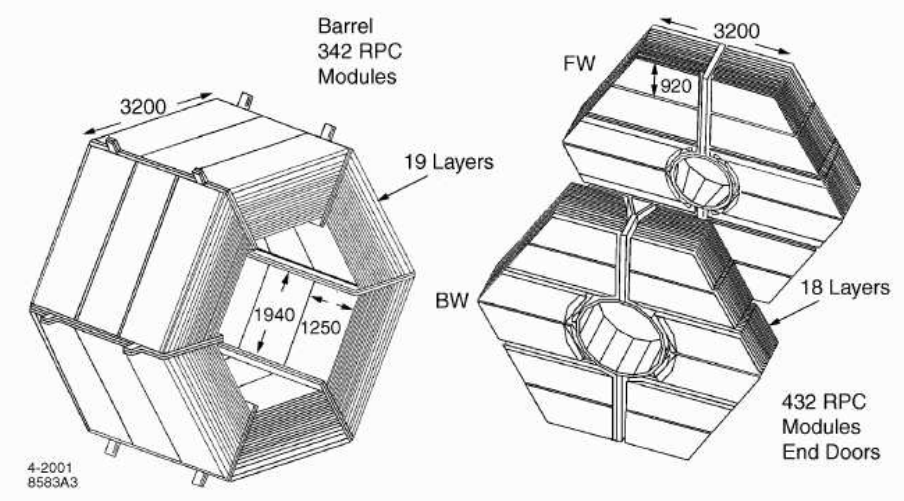

Figure 2.19: IFR view.

The iron barrel surrounds the solenoid and it is made of 6 sectors, named sextants. The barrel is 3.750 m long along the z axis and covers the radial distance between 1.820 m and 3.045 m. The two endcaps cover the forward and backward region. The four sextants of the IFR instrumented with RPCs consist of 19 active layers, each layer is composed by three RPCs which cover whole its surface. The two endcaps have an hexagonal shape and they are vertically subdivided in two halves in order to allow access to inner subsystems. The iron plates have a thickness ranging from 2 cm, for the inner ones, to 10 cm for the outermost ones; the iron has a thickness of $\geq$ 65 cm in total, corresponding to $\sim$ 4 interaction lengths inside the barrel, and $\geq$ 60 cm in the endcaps. The segmentation of the iron is designed in order to have a good distinction between muons, which should cross about all layers, and pions of similar energies, which should stop before. The original K_L^0 detection capability of the IFR resulted in a fine iron segmentation, which has been changed with the new LST layout. For a detailed description of the segmentation of the iron see Chap.3. Two cylindrical RPC layers have also been installed between EMC and the magnet cryostat in order to detect particles exiting the EMC, to increase the K_L^0 efficiency. Cylindrical layers are subdivided in four sectors, each one covering one fourth of the circumference and has four RPC groups with orthogonal readout strips. $u - v$ helicoidal strips are placed inside along the module diagonal while ϕ and z parallel strips are placed outside.

RPCs detect streamers from ionizing particles via capacitive readout strips. They offer the advantage of simple and low cost construction. Further benefits are large signals and fast re-

sponse allowing for simple and robust front end electronics and good time resolution, typically 1-2 ns. The position resolution depends on the segmentation of the readout; few millimeters are achievable. A cross section of an RPC is shown schematically in figure 2.20. The planar RPCs consist of two bakelite (phenolic polymer) sheets, 2 mm thick and separated by a gap of 2 mm. The bulk resistivity of the bakelite sheets has been especially tuned to $10^{11} - 10^{12} \Omega\,\mathrm{m}$. The external surfaces are coated with graphite to achieve a surface resistivity of approximately $100 k\Omega/\Box$. These two graphite surfaces are connected to high voltage (approximately 8 kV) and ground, and protected by an insulating mylar film. The bakelite surfaces facing the gap are treated with linseed oil to improve performance. The modules are operated in limited streamer mode and the signals are read out capacitively, on both sides of the gap, by external electrodes made of aluminum strips on a mylar substrate. The gas used in RPC is a mixture of Argon, Freon and Isobutane with respective fraction of 56.7%, 38.8% and 4.5%.

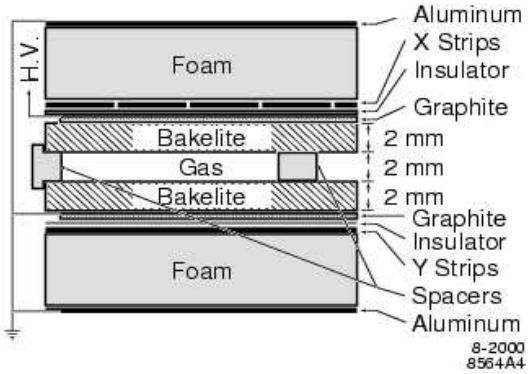

Figure 2.20: Planar RPC section with HV connection scheme.

2.9 Trigger system

The trigger system [24] is designed in order to have high efficiency for the type of events of interest for *BABAR* and to have a high rejection power of background events. The interesting events for *BABAR* are summarized in Tab.2.2. The trigger system has to keep the total rate of events under

Event type	Cross section (nb)	Production Rate (Hz)	Level 1 Trigger Rate (Hz)
$b\overline{b}$	1.05	3.2	3.2
other $q\overline{q}$	3.39	10.2	10.1
e^+e^-	∼40	159	156
$\mu^+\mu^-$	1.16	3.5	3.1
$\tau^+\tau^-$	0.94	2.8	2.4

Table 2.2: Cross sections, production and trigger rates for the principal physics processes at 10.58 GeV for a luminosity of $3 \times 10^{33}\,\mathrm{cm}^{-2}\mathrm{s}^{-1}$. The e^+e^- cross section refers to events with either the e^+, e^-, or both inside the EMC detection volume.

1 kHz. At design luminosity, the beam-induced background rates are typically about 20 kHz. In order to monitor continuously the efficiency, performances and background rejection of the trigger, prescaled samples of special events are selected, such as those failing the trigger selection and

random beam crossings.
The total trigger efficiency is required to exceed 99% for all $B\overline{B}$ events and al least 95% for continuum events. The efficiency for other events like $\tau^+\tau^-$ is in the range 90%-95%. Other requirements for the trigger system is that it has to be robust and it has to be able to operate also with dead electronics channels; moreover, its contribution to the dead time for data acquisition has not to exceed 1%.
The trigger system is composed by two levels: the Level 1 (L1) which is an hardware trigger and the Level 3 (L3) which is a software trigger. The output of L1 is set at about 1 kHz and it is sent to L3 which performs a first selection of the category of events, in order to monitor the luminosity, diagnostic and calibration. At designed luminosity the L3 filter acceptance for physics events is about 90 Hz, while it is about 30 Hz for special types of events. See Fig.4.3 for muon identification and hadron misidentification probability.

2.9.1 Level 1 Trigger

The L1 trigger decision is based on charged tracks in the DCH above a preset transverse momentum, showers in the EMC, and tracks detected in the IFR. The drift chamber trigger (DCT) and electromagnetic calorimeter trigger (EMT) both satisfy all trigger requirements independently with high efficiency, and thereby provide a high degree of redundancy, which enables the measurement of trigger efficiency. The instrumented flux return trigger (IFT) is used for triggering $\mu^+\mu^-$ and cosmic rays, mostly for diagnostic purposes.

The L1 trigger configuration consists of DCT-only, EMT-only, mixed and prescaled triggers. Although most triggers target a specific physics source, they often also select other processes. For example, two-track triggers are not only efficient for Bhabha, $\mu^+\mu^-$, and $\tau^+\tau^-$ events, but are also useful for selecting jet-like hadronic events and some rare B decays. Although triggering on generic $B\overline{B}$ events is relatively easy, it is essential to ensure high efficiencies for the important rare low-multiplicity B decays. A direct study of efficiencies demonstrated that the DCT and the combined EMT/IFT provide fully efficient, independent triggers for most physics processes, although independent triggers for $\mu^+\mu^-$ and $\tau^+\tau^-$ are not individually fully efficient.

For a typical L1 rate of 1 kHz, Bhabha and annihilation physics events contribute $\sim$170 Hz. There are also 100 Hz of cosmic ray and 20 Hz of random beam crossing triggers. The remaining triggers are due to lost particles interacting with the beam pipe, the synchrotron radiation and two-beam background.

2.9.2 Level 3 Trigger

The L3 trigger software comprises event reconstruction and classification, a set of event selection filters, and monitoring. The filters have access to the complete event data for making their decision, including the output of the L1 trigger. L3 operates by refining and augmenting the selection

Event type	Rate (Hz)
Hadrons, $\tau\tau$, and $\mu\mu$	16
Other QED, 2-photon events	13
Unidentified Bhabha backgrounds	18
Beam-induced backgrounds	26
Total physics accept	**73**
Calibration Bhabhas (e^+e^-)	30
$\gamma\gamma$, Radiative Bhabhas ($e^+e^-\gamma$)	10
Random triggers and cosmic rays	2
L1,L3 pass through diagnostics	7
Total calibration/diagnostics	**49**

Table 2.3: Composition of the L3 output at a luminosity of $2.6\times10^{33}\,\mathrm{cm}^{-2}\mathrm{s}^{-1}$.

methods used in L1. For example, better DCH tracking (vertex resolution) and EMC clustering filters allow for greater rejection of beam backgrounds and Bhabha events. High efficiencies are independently achieved for the DCH and EMC based filters applied to simulated hadronic events. The comparison between data and Monte Carlo L3 trigger pass fractions for the various filters also show good agreement when requiring tracking, and EMC based hadronic event selections in turn.

For a typical run on the $\Upsilon(4S)$ peak with an average luminosity of $2.6\times10^{33}\,\mathrm{cm}^{-2}\mathrm{s}^{-1}$, the L3 event composition is tabulated in Tab.2.3. The desired physics events contribute 13% of the total output while the calibration and diagnostic samples comprise 40%.

2.10 *BABAR* Computing

The *BABAR* online computing system comprises the data acquisition chain from the common Front End Electronics (FEE), through the embedded processors in the data acquisition system and the L3 trigger, to the logging of event data. It also includes those components required for detector and data acquisition control and monitoring, immediate data quality monitoring, and online calibration. In Fig.2.21 we show the scheme of the data acquisition chain. The data acquisition chain was designed to meet the following basic performance requirements: it must support a L1 trigger accept rate of up to 2 kHz, with an average event size of $\sim$32 kbytes and a maximum output (L3 trigger accept) rate of 1 kHz. While performing these functions it should not contribute more than a time-averaged 3% to deadtime during normal data acquisition.

The online system is also required to be capable of performing data acquisition simultaneously on independent *partitions* —sets of detector system components— to support calibrations and diagnostics. Following standard practice, the event data acquired by the system are subjected to monitoring. Such monitoring is configurable by experts and designed to detect anomalies in

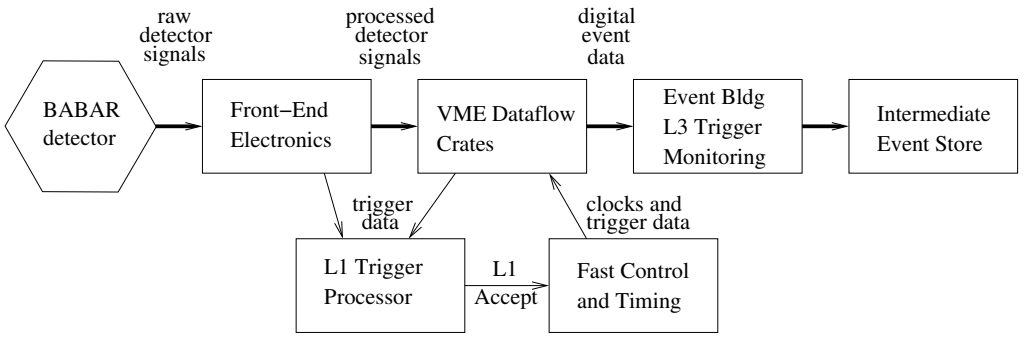

Figure 2.21: Data acquisition schematic diagram.

the detector systems which, if present, are reported to operators for rapid assessment and, if necessary, corrective action.

Environmental conditions of the detector, such as the state of low and high voltage power, the purity of gas supplies, and the operating conditions of the accelerator, such as beam luminosity and currents, are measured and recorded in a fashion that permits the association with the event data logged. Conditions relevant to data quality are monitored for consistency with specified standards. Operators are alerted if these are not met. Data-taking is inhibited or otherwise flagged if conditions are incompatible with maintaining the quality of the data.

Operational configurations, calibration results, active software version numbers, and routine messages and error messages are also recorded. During data analysis or problem diagnosis, these data help in reconstructing the detailed operating conditions.

2.10.1 System Components

The online computing system is designed as a set of subsystems using elements of a common software infrastructure running on a dedicated collection of hardware.

The major subsystems are:

- Online Dataflow (ODF)—responsible for communication with and control of the detector systems' front-end electronics, and the acquisition and building of event data from them;
- Online Event Processing (OEP)[29]—responsible for processing of complete events, including L3 (software) triggering, data quality monitoring, and the final stages of calibrations;
- Logging Manager (LM)—responsible for receiving selected events sent from OEP and writing them to disk files for use as input to the *Online Prompt Reconstruction* processing;
- Online Detector Control (ODC)—responsible for the control and monitoring of environmental conditions of the detector systems;

- Online Run Control (ORC)—ties together all the other components, and is responsible for sequencing their operations, interlocking them as appropriate, and providing a *graphical user interface* (GUI) for operator control.

The entire system is coded primarily in the C++ language, with some use of Java for graphical user interfaces. Object-oriented analysis and design techniques have been used throughout. This has been an important feature, enhancing development speed, maintainability, and extensibility.

2.10.2 Performance

The online system has exceeded its data acquisition performance goals. It is capable of acquiring colliding beam events, with an average size of 28 kbytes, at a $\sim 2500 Hz$ L1 trigger rate and reducing this rate in L3 to the required $\sim 1 kHz$ limit. This provides comfortable margins, since under normal beam conditions the L1 trigger rate is 800–1000 Hz.

The system is capable of logging data at much higher rates; the nominal 200 Hz figure represents a compromise between data volume and its consequential load on downstream processing and archival storage, and trigger efficiency for low multiplicity final states. During normal data-taking, the online system routinely achieves an efficiency of over 98%, taking both data acquisition livetime and the system overall reliability into account. There are several hardware options for enhancing ODF capacity. Currently most read out modules (ROM) receive more than one fiber from the FEE. These fibers could be distributed over more ROMs to add processing power.
Current background projections indicate that fragment level CPU, segment level memory bus bandwidth, and network event building bandwidth are the most likely bottlenecks for future running. Increases in the L1 trigger rate or in the background occupancy and complexity of events are expected to necessitate additional capacity for OEP, principally for L3 triggering. The online farm machines could be replaced with faster models. More machines could be added, at the expense of increases in coherent loading on various servers and of additional management complexity.

Chapter 3

The IFR-LST Detector

3.1 The motivation for a new barrel muon detector

Since the initial operations, the barrel muon detector IFR composed by RPC showed a decrease of efficiency, as it is shown in Fig.3.1, where the efficiency versus time is reported [32]. Different facts could contribute to the decrease of efficiency. A first problem was the high temperature of the iron. During initial *BABAR* operations, the temperature of the iron increased to as much as 34^oC, in part due to the lack of cooling for RPC electronics. Inside RPC, the trapped linseed oil decreased in viscosity and leaked out of the spacer cavities into the active volume of the chamber. This oil under the electrostatic forces formed bridges between the anode and the cathode planes with a resistance of about $1/40^{th}$ of the value expected for the fresh linseed oil: as a direct consequence there was a decreasing of efficiency around these region of the chamber. Although cooling was installed shortly thereafter, reducing the operating temperature to 24^oC, efficiencies have continued to decline at the rate of approximately 1.2% per month as shown in Fig.3.1. The RPC continued to show a decrease of the efficiency with an increase of the currents, then also the HV system could not be efficient as well. Other problems came from gas system and electronic readout. During the year 2002 a "remediation" [1] procedure was tried in order to recover the efficiency of the RPC, but it did not give good results. One of the main problems is the fast aging of the RPC, due to the high particle rate [2], which causes a high accumulated charge in short time. This fact was also noticed in new RPC installed in the forward endcap in the year 2002, especially for those in the outer layer (17 and 18) which shown a low decrease of efficiency of about 10% after a period of 500 days.

To exploit the complete physics program of the *BABAR* experiment a high efficiency muon detector is needed. So the collaboration decided to upgrade the barrel IFR detector. Three different choices were proposed: (1) LST, (2) RPC and (3) Scintillators. After about one year of R&D on

[1] Remediation was a procedure that allows RPC to draw high current in argon atmosphere with both normal and reversed voltages.

[2] $0.2 - 0.5 Hz/cm^2$ in the barrel and $5 - 20 Hz/cm^2$ in the endcap.

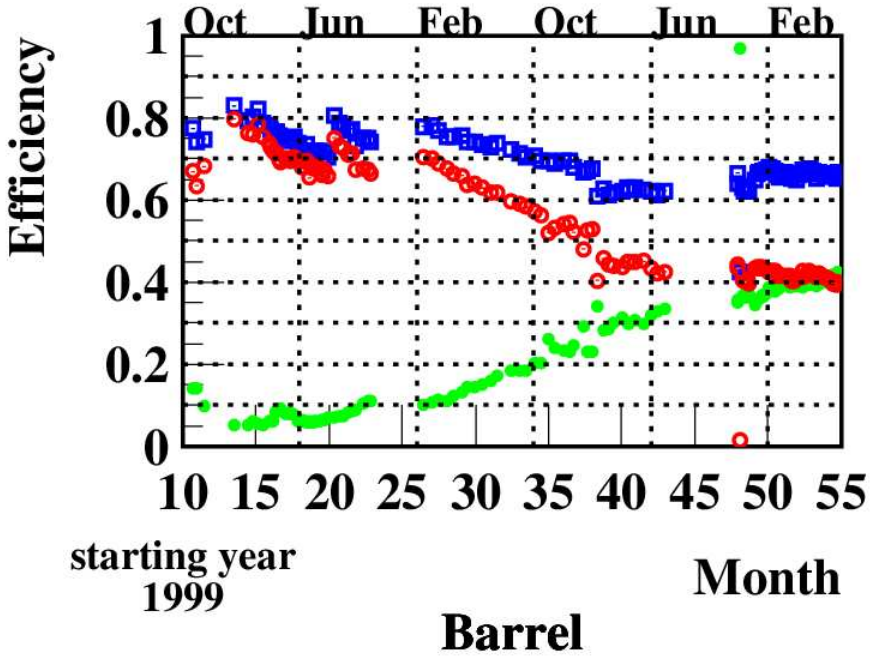

Figure 3.1: Average efficiency of the barrel RPC chambers as a function of date, in month since June 1999. Squares (blue) are all RPCs with efficiency grater than 10%, open circles (red) are all RPCs and full circles (green) are all RPCs with efficiency less than 10%.

prototypes of LST the committee choose the LST as new detector for the IFR barrel. The motivations are that LSTs are conceptually well understood and they have been used in other HEP experiments showing very good performances and very low mortality [36], while the chemistry of RPC detector remains poorly understood. The proposal of scintillators requires a lot of R&D and a high cost.

3.2 Working principles of the LST

The limited streamer tube, also known as Iarocci tube [35], is generally composed by square cells opened on one side and with the other walls coated with graphite plastic. In some cases all four sides are present and conductive. The LST used for the IFR upgrade are of the type with 3 conductive walls as shown in Fig.3.2. In the center of the cell there is a wire, connected to a positive HV, while the conductive walls are at ground. Inside the cells a specific gas mixture flows, which will be discussed later. The LST works in the region of limited streamer, which means that the discharge produced by the passage of a charged particle does not propagate along the wire, but with a particular configuration of voltages and gas mixture the discharge becomes limited around the zone of the wire reached by first ionization electrons. The region of limited streamer is situated between the proportional region and the Geiger-Muller region, as shown in Fig.3.3 [30].

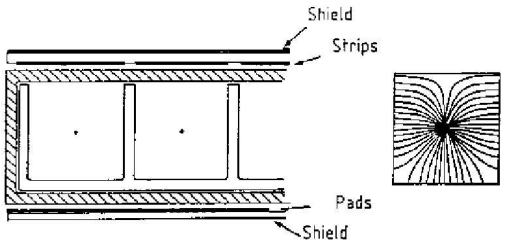

Figure 3.2: Line's field in a LST coverless.

The gas mixture must have an high power of absorption of ultraviolet photons in order to limit the discharge, then an high fraction of quencher gas has to be in the mixture. Moreover for safety reasons the mixture has to be non-flammable, then generally high fraction of CO_2 is used. Various mixtures have been used in past experiment, for example ZEUS and SLD used a ternary mixture of $CO_2/C_4H_{10}/Ar$ with the compositions (88/9.5/2.5)% and (89/8/3)% [36], respectively. The signal collected on the wire can be extracted in order to have information of the two coordinates: the coordinate along the wire and the coordinate orthogonal to the wires. The coordinate orthogonal to the wires can be read directly from the wires with an adequate decoupling circuit in order to decouple HV voltage from the readout system. Another way to readout the coordinate orthogonal to the wires is to use external strips parallels to the wires: the discharge accumulated in a restricted region on the wire will induce a positive signal on an external strip near the wire. This method is mainly used to readout the coordinate along the wires with a system of strips orthogonal to the wires.

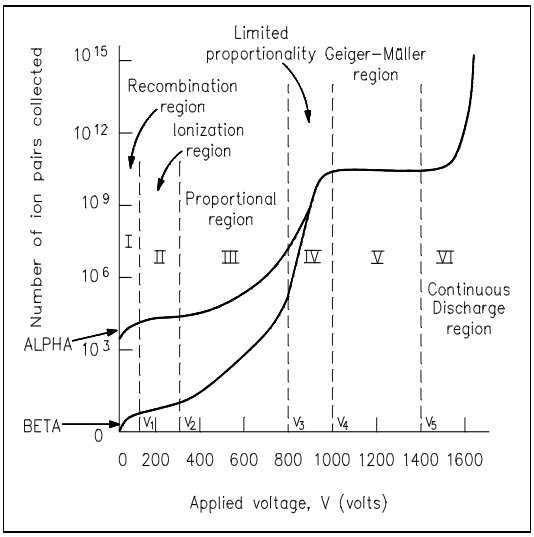

Figure 3.3: Collected charge versus voltage [30].

3.3 Proposal of a new muon detector with LST

After extensive detector R&D [37] the LST team [31] confirmed the high reliability of this detector. This is very important, because the access to the barrel region will continue to be difficult and in same cases impossible. The idea is to instrument the barrel region with high modularity, in order to have the chance to replace some modules in case that this operation results necessary. This modularity can be easily obtained assembling modules of two or three LSTs. Moreover major

Experiment	tubes	length (m)	mortality	comments
ZEUS	3400	10	$\approx 6\%$ 2%	- first 2 years due to short conditioning - last 7 years
DELPHI	19000	≤ 4.1	$\approx 1\%$	infant mortality
OPAL	6700	$3 \div 7.3$	6%	in 10 years
SLD	10000	$1.9 \div 8.6$	10% in 10 years 3%	- for the barrel, low initial experience and mechanical problems during installation. -for the endcaps (shorter tubes).
MACRO	6000	12	$\approx 0.1\%$	infant mortality of wires, only 6 wires out of 49536 disconnected per year. 2.9×2.7 cm^2 cell section

Table 3.1: Summary of LSTs used in past HEP experiments [36].

HEP experiments in recent years used LSTs and the experience with these detectors showed that LSTs work with high efficiency and reliability over many years. As example we can refer to ZEUS, LEP, MACRO, CLEO, SLD and PHENIX experiments [36]. In Tab.3.1 we show the mortality experienced with other HEP experiments.
LST Team studied two different options for the new LSTs: a single-layer of large cell and an alternative configuration of a double-layer of smaller cells. As we will describe later the collaboration chose to use the single layer large cell configuration after a detailed comparison between the two types.

3.3.1 Single-Layer Large-Cell tube

The single-layer large cell is designed to have cell size of 15×17 mm^2, as shown in Fig.3.4(a). Two sets of tubes are needed for the modularity (see section 3.3.4): a set of tubes with 8 cells and a sets of tubes with 7 cells. In the first set each pair of cells will be connected at a HV supply, then each 8-cell tube has 4 independent HV channels. Also the 7-cell tube has 4 HV channels, but in this case 3 HV channels supply 3 pairs of cells and the forth supplies a single cells. The Φ coordinate will be readout by signals from wires, while Z coordinate will be measured by a system of external strips.

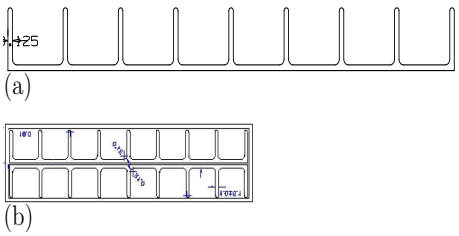

Figure 3.4: (a) The large-cell profile. (b) The double-layer small-cell design: two small cell profiles in one large sleeve.

3.3.2 Double-Layer Small-Cell tube

In the double-layer small-cell design, two profile are inserted back to back into a single large sleeve as shown in Fig.3.4(b). Due to the constriction of the gap dimension in the IFR the cells have to be the dimensions of 8×9 mm^2. This configuration is designed to be redundant: in case that one tube fails, the other layer will recover this inefficiency. Adopting a high resistivity graphite coating the coordinate readout will be given by Φ and Z strips. Clearly this solution implies to use a more complicated HV system than the single-layer solution.

3.3.3 Comparison between Large and Small cells

In order to compare the two solutions we have to consider various aspects, that we can group in three categories: performance, cost and schedule.

Performance

Concerning performances we are interested in the more relevant aspects, which are reliability, efficiency, drift time and occupancy.

Reliability

Usually the mortality of a LST is associated with an increase of the dark current, that leads to a non recoverable damage. The major causes of this behavior can occur as consequence of bad regularity of the cell shape, a wrong displacement of the wire along the cell and defects or non-homogeneous graphite coating, like pinnacles, rough surface and so on. It is clear and also demonstrated by past experience that when cells are larger the effects coming from the construction defects listed before are smaller. In fact standard LSTs with 9×9 mm^2 cells show a mortality of about 0.5% per year, while, for example, MACRO experiment, which used larger cells (2.9×2.7 cm^2), shows a mortality of the order of 0.1%. The large cell is less sensitive than small cell to small displacements of the wire from the center of the cell, this leads to an electrostatic design much more favorable. A direct consequence of a misplacement of the wire could be a reduction of the width of the plateau: in a small cell this reduction is higher than in a large cell. Another important aspect is the wire holder used in the different two configurations. In small cell the holders are melted around the wire, while in large cell the holders are bigger and equipped with plastic clips that guarantee a more reproducible and precise wire position. Concerning the loss of efficiency coming from the die of one HV channel and considering the same failure rate, one can calculate that the double-layer configuration would be 2.5 times more reliable than the large-cell option. But we know that large-cell has a failure rate which is at least 3 to 5 times better than that for small-cell, then we can conclude that the two configurations have about the same reliability.

Efficiency

The efficiency of different cell configurations have been studied by Monte Carlo simulation. Three different cell type have been treated: standard small-cell 9×9 mm^2, small-cell for double layer 9×8 mm^2 and large-cell 15×17 mm^2. The results are shown in Fig.3.5, where the inefficiency is plotted as a function of the minimum track path inside the cell required to generate sufficient ionization to produce a signal (≈3 mm are sufficient). Both options result to have a low inefficiency, and also the overall efficiency of the detector results similar.

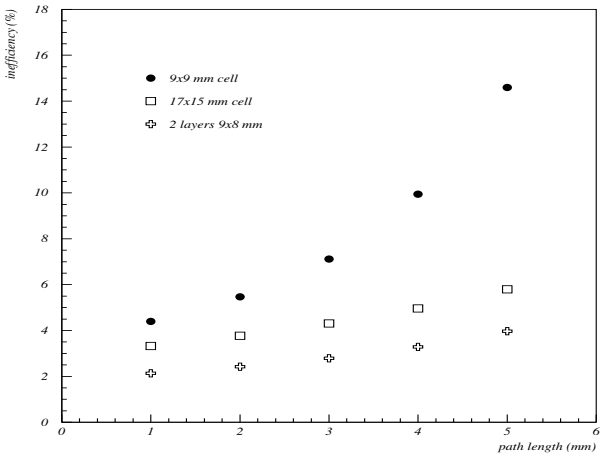

Figure 3.5: Monte Carlo results for inefficiency versus path length for various cell geometries: 9×9 (●), 15×17 (□) and double layer 9×8 (+).

Drift time and occupancy

The longer drift time (up to ≈300 ns) of the large cell is not expected to cause any significant increase of random coincidences with the first level trigger. The low level of background expected in barrel IFR (< 2 Hz/cm^2) could at least cause an occupancy less than 0.5% in the innermost layers.

Costs, Schedule and Conclusions

The single-layer large cell option results about 30% cheaper than the double-layer solution and also the production time for the first option is shorter than for the second one. Both solutions satisfy all requirements for an upgrade, but the last considerations led to the decision of instrument the IFR with single-layer large-cell LSTs.

3.3.4 LSTs modularity design

Installation procedure, possible substitution of installed tubes and dimensions of the gaps of the Barrel IFR require a specific modularity of the LSTs. In order to achieve the desired modularity, LSTs have been built of three different types: 7 and 8 cells, long type (358 cm) and 8 cells, short type (318 cm). Modularity requires also to assemble the tubes in different mod-

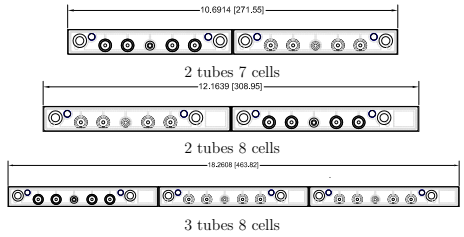

Figure 3.6: Front view of the three designed modules of large cell LSTs: 2×7 cells (top), 2×8 cells (middle), 3×8 cells (bottom).

ules: modules of 2 8-cell short and long LSTs, modules of 2 7-cell LSTs and modules of 3 8-cell long LSTs have been assembled. Fig.3.6 shows the three kind of modules. Each layer of Barrel IFR will be instrumented with a specific combination of the modules as shown in Fig.3.7. The layer 18, which is closed by a flux iron bar, need to be instrumented with the modules made by short LSTs. Tab.3.2 shows the required modules for each layer. In order to replace in total 72 layers with new detector the total number of LSTs to be produced is 1379: the various types are reported in Tab.3.3.

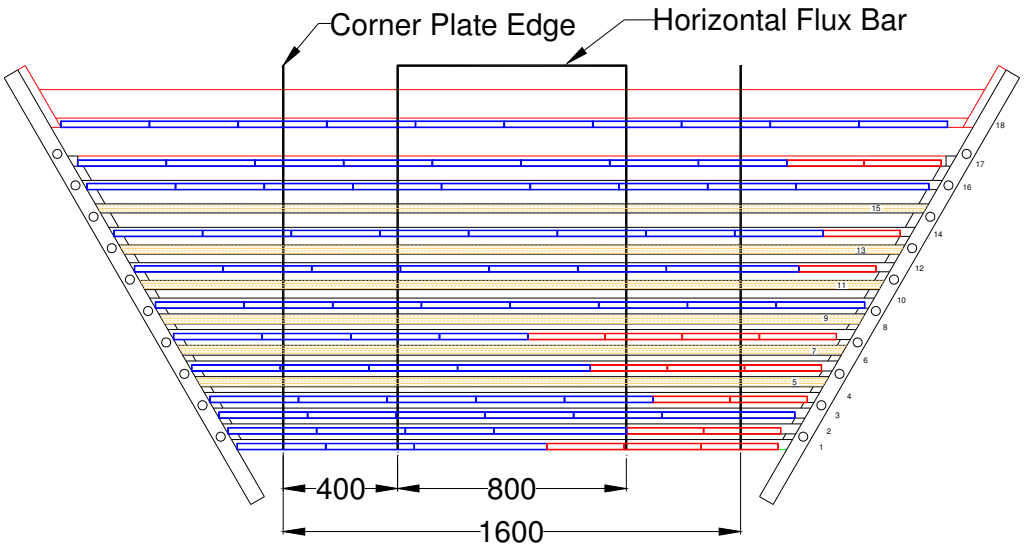

Figure 3.7: Front view of the composition of module array in a sextant: 3×8 and 2×8 modules (blue), 2×7 modules (red) and brass absorber (yellow).

Layer	♯ modules long 2×8-cell	♯ modules long 3×8-cell	♯ modules long 2×7-cell	♯ modules short 2×8-cell
1	2	1	3	0
2	3	1	2	0
3	5	1	0	0
4	5	0	2	0
5	brass	×	×	×
6	3	1	3	0
7	brass	×	×	×
8	4	0	4	0
5	brass	×	×	×
10	8	0	0	0
11	brass	×	×	×
12	6	1	1	0
13	brass	×	×	×
14	8	0	1	0
15	brass	×	×	×
16	8	1	0	0
17	8	0	2	0
18	0	0	0	10

Table 3.2: LSTs modules association to each layers. See section 3.4.1 for a detailed description of the shown brass absorber configuration.

Length (cm)	Cells	Quantity
358	8	972
318	8	150
358	7	257

Table 3.3: Number and kind of LST produced for IFR barrel upgrade.

3.4 Monte Carlo simulation for performance study

Detailed studies concerning the thickness of the absorber in the IFR barrel have been performed in order to find some possible improvement in the performances of the detector. Here we will discuss different brass absorber configurations and efficiency for muon detection for the selected option.

3.4.1 Study of brass absorber configurations

The Barrel IFR must provide a good muon and also K_L^0 identification, in order to maximize the efficiency of detection of the decays with K_L^0 in the final state, such as $B^0 \rightarrow J/\psi K_L^0$ [32]. This fact required an absorber configuration with high degree of longitudinal segmentation in first 10 layers of the IFR: between these layers the iron absorbers is only 2 cm. In order to have also a good muon identification an extra layer (19^{th}) was installed, reaching a configuration with a total of 5.07 λ_{int} before layer 19, where the largest increments in material are within the last few layers, as shown in Fig.3.8. Since the layer 19 is not accessible, the replacement of old RPCs with new detector cannot involve layer 19. Without layer 19, in the barrel region the total amount of material before last active layer (18^{th}) is less than 5 interaction length, as shown in Fig.3.8. This value is at the lower end of what is desirable for a muon ID system at the $\Upsilon(4S)$ energy range, in fact the majority of muons in IFR range between 4 and 10 λ_{int} as shown in Fig.3.9(a). Fig.3.9(b) shows a GEANT Monte Carlo simulation for muon range as a function of momentum. The muon range is linearly related to the momentum as can be obtained from Fig.3.9, which gives the following relation:

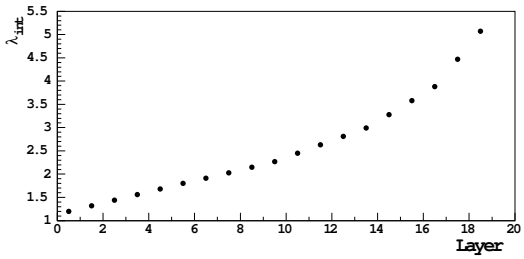

Figure 3.8: Interaction length versus layer number in old absorber configuration.

$$\frac{L}{\lambda_{int}} \approx 5 \cdot \frac{|\vec{p}|}{1\ \mathrm{GeV}} \tag{3.1}$$

The replacement of Barrel IFR detector is an opportunity to improve the configuration of the absorbers. For this purpose three different benchmark designs have been studied, named BD1, BD2 and BD3. In these designs some of the active detector layers are replaced with brass plate

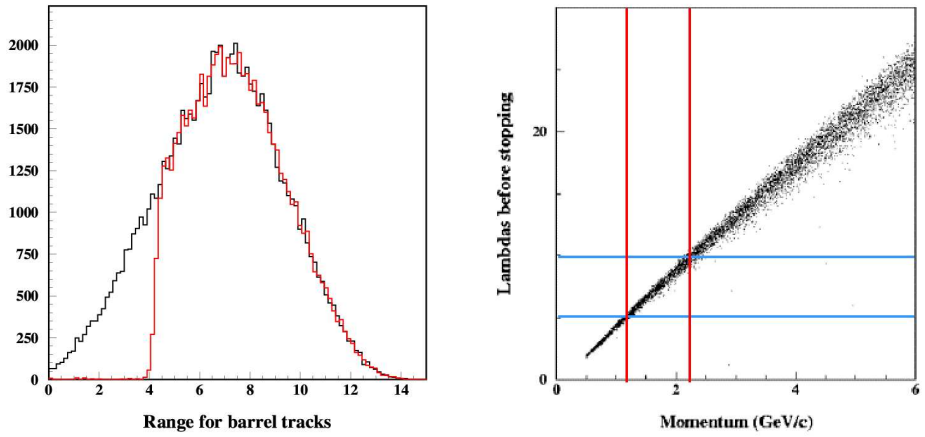

(a) (b)

Figure 3.9: (a) Distribution of expected muon range expressed in nuclear interaction lengths, for muons from inclusive $B \rightarrow X_u l\nu$. The red histogram corresponds to muon with momentum grater than 1 GeV. (b) GEANT Monte Carlo simulation for muon range as a function of momentum. The horizontal blue lines are drawn at 5 and 10 interaction lengths.

Configuration	Layers with absorbers	Expected λ_{int} at 90^o
BD1	8,10,12,14,16 (13 active layers)	5.1
BD2	5,7,9,11,13,15 (12 active layers)	5.3
BD3	2,3,4,5,7,9,11,13,15 (9 active layers)	5.7

Table 3.4: Description of the three proposed absorber configurations.

2.2 cm thick. In BD1 the replaced layers are: 8, 10, 12, 14 and 16. In BD2 six absorbers are added in layers: 5, 7, 9, 11, 13 and 15. In BD3 the configuration has been chosen with 9 layers replaced by absorbers: in this configuration the K_L^0 identification is compromised and it does not satisfy the earthquake requirement. The three different configurations are described in Tab.3.4, while in Fig.3.10 we compare the three different configurations with the initial configuration. The figure shows the absorber configurations (Fig.3.10(a)), last hit layer distribution (Fig.3.10(b)), map of the amount of material versus $\cos\theta$ (Fig.3.10(c)) and the pion fake rate as a function of efficiency of muon ID (Fig.3.10(d)). All this study have been obtained with Monte Carlo simulation under the assumption that all detectors inside IFR have 95% of efficiency.

In order to identify the best solution we look at the simulation results. The BD3 configuration has the best performance for muon identification, but it compromise the K_L^0 identification and it does not satisfy the earthquake requirements, then it is excluded from the possible available configurations. Both BD1 and BD2 are good designs with a K_L^0 efficiency of the order of 30%, but BD2 is the preferred configuration, because it has a better muon identification.

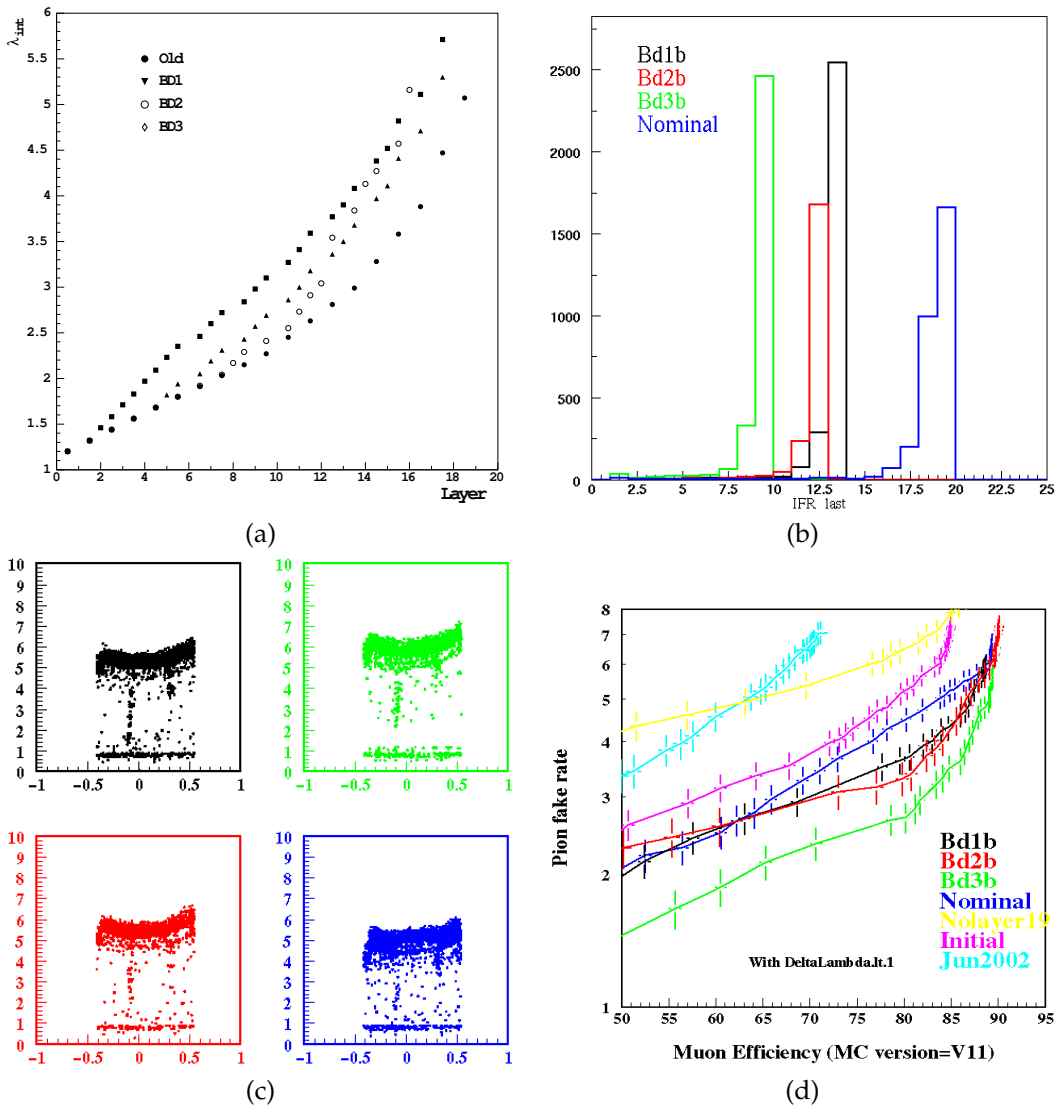

Figure 3.10: Comparison between the old and the three proposed absorber configuration: (a) interaction versus number layer; (b) distribution of the last layer reached by the particles; (c) interaction length versus θ; (d) fake pion rate versus muon efficiency.

3.4.2 Results for μ detection efficiency for IFR barrel with LST in BD2 configuration

In order to study the efficiency detection for IFR barrel with LST, the LST geometry have been implemented in the standard GEANT *BABAR* simulation and the code reconstruction have been used to select muons and calculate the detection efficiency as a function of θ in various configurations. The efficiency obtained from LST configuration is compared with that from ideal RPC configuration. The design of LST configuration is discussed in section 3.4.1. Fig.3.11 [38]

shows the efficiency for muon detection as a function of θ for LST and compared with ideal RPCs. The comparison of efficiency versus θ between long and short tubes shows that the moving back of the sensitive volume of 5 cm of the tube from very forward end of the plate lead to a very small loss of efficiency in this region (around 1 rad). This suggests that a dead space up to 5 cm in the forward region of the barrel (needed for LST services) should not affect the μ detection efficiency in a sensible way. Also the efficiency variation due to the strip multiplicity has been studied. The strip multiplicity has been changed both in z and ϕ view and the cases with only the fired strip on and with three strips on average for each particle have been compared and result that the muon identification shows only a very small dependence with this parameter. Also pion misidentification results comparable between LSTs and ideal RPCs.

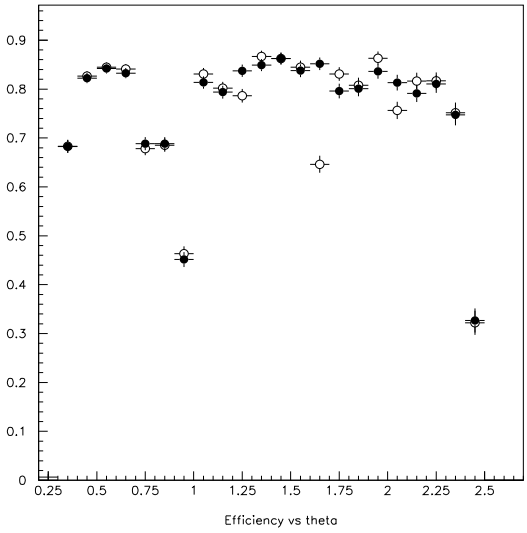

Figure 3.11: Muon efficiency versus θ for LST (•) and for ideal RPC (○) [38].

3.5 R&D of LST

About one year before the beginning of the LSTs production various prototypes of LST were produced by Pol.Hi.Tech. in order to allow us to study these detectors. The extensive R&D [37] was necessary in order to reach a good knowledge about LST and in order to improve all details of construction for the production. That means that tests were done to choose the gas mixture, the working voltages and so on. All observations which came out from tests on prototype were used to set the quality requirements for the production, requirements that were checked during this phase by the quality control infrastructure realized by INFN-US people.

A large amount of studies were done on LST prototypes. In this section we will illustrate just the more important tests done before the production. The first double-layer LST prototypes with non-standard cells of 9×8 mm^2 were used for wire and graphite coating quality studies, wire displacements and in general for detailed issues on construction. Other single-layer LST prototypes with standard cells of 9×9 mm^2 and single-layer large cell LST prototypes were used for studies on gas mixture, electric anode-wire field, plateau, aging and source scan tests.

3.5.1 Graphite coating quality

The firsts double-layer prototypes with non standard cells of 9×8 mm^2 produced by Pol.Hi.Tech. did not show good behavior, it was not possible to obtain good plateau curve, then it was decided to open the prototype. Opening the prototype it was found that the graphite coating showed various defects on painting and also the presence of debris was noticed. With this experience LST collaborations required high quality control on graphite coating on the other prototypes used for following test. Moreover LST collaboration decided to implement a graphite coating quality control for each tube during the production, in order to have final LSTs with good graphite coating.

3.5.2 Anode-wire

The first double-layer prototype with non standard cells of 9×8 mm^2 produced by Pol.Hi.Tech. showed bad anode-wire displacement, as shown in Fig.3.12, where the distances between anode-wire and the bottom of the graphite coating are reported. This bad displacement was due to the

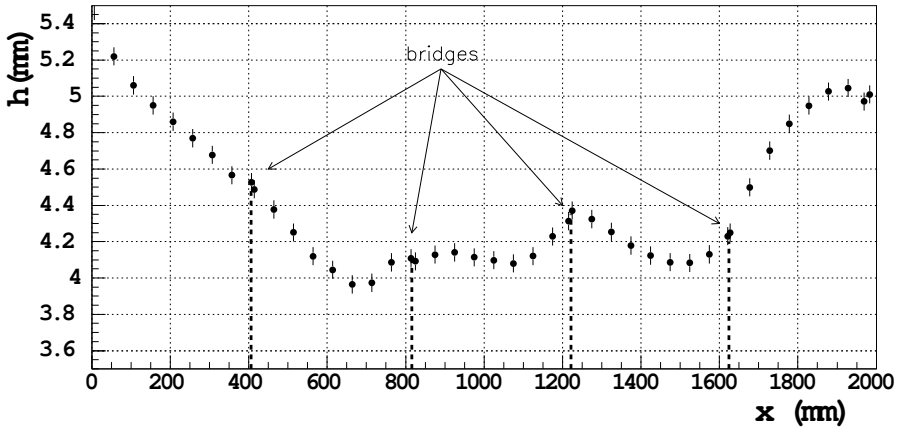

Figure 3.12: Distances between anode-wire and bottom graphite measured on a first double layer 9×8 mm prototype produced by Pol.Hi.Tech..

fact that the first non-standard cell prototypes (9×8 mm^2) were constructed modifying the standard profile (9×9 mm^2) and also the standard wire holders were modified: the bad manipulation of this small parts caused the bad displacement. Displacements of the anode-wire cause variation on the electric field, then changes the LST behavior. In Tab.3.5 we show the variation of the electric field due to displacements of wire. We can notice that a little displacement of 1 mm causes high variation of the voltage. Concerning the quality of the wire for the production, it was decided to make some test on a sample of each spool of wire. The wires used for the production have been found of good quality.

	$E_{max}\ (V/m)$ on anode wire surface	$E_{min}\ (V/m)$ on anode wire surface	E_{mean}	$\Delta E_{mean}/E_{mean}$	$\Delta V(V)$ (V=5 kV)
Normal LST 9×9 mm	2.001×10^7	1.967×10^7	1.985×10^7	0%	0
Anode wire up 0.5 mm from center	1.966×10^7	1.93×10^7	1.949×10^7	-1.8%	-90
Anode wire up 1.0 mm from center	1.929×10^7	1.89×10^7	1.910×10^7	-3.8%	-190

Table 3.5: Effects of wire displacements on electric field.

3.5.3 Source scan test

In an assembled LST detector very small defects on graphite coating like small spots or pinnacles and displacements of the anode wire can be found scanning the cells with a radioactive source and reading the drawn current during the scan. In zones of graphite without defects we will have a constant current, while in correspondence of a pinnacle it is possible to have a spike of current. Also a displacement of the anode wire will be recognized by a variation of current from the mean value. In Fig.3.19 we show examples of source scan test made on large cell LST. This test has been implemented in the production.

3.5.4 Gas mixture effects on plateau and efficiency

Various gas mixture have been tested on LST prototypes, in order to check the differences on plateau curves and on efficiencies. LST collaboration tested four main different gas mixtures of $Ar/C_4H_{10}/CO_2$: 1) (3.5/8/88.5)%, 2) (3.5/9.5/87)%, 3) (9/9/82)% and 4) (9/16/75)%. In Fig.3.13 we show the plateau curves of large cell LST obtained with the four different gas mixtures. We no-

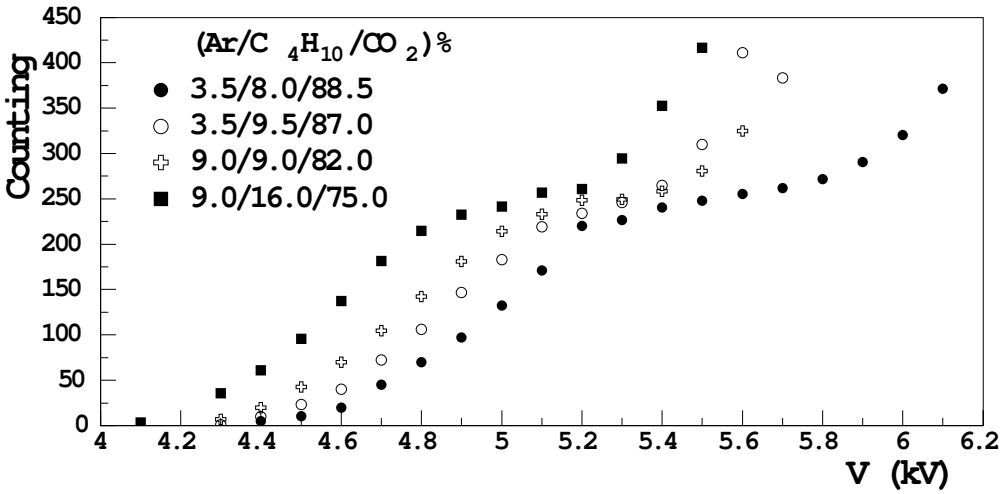

Figure 3.13: Plateau curves obtained with 4 different gas mixtures on large cell prototype.

ticed that the mixture with high fraction of Ar shifts the plateau region at lower voltage. A similar plateau was obtained for the standard cell (9×9 mm^2) with the SLD gas mixture ($Ar/C_4H_{10}/CO_2$ (2.5/9.5/88)%). The measurements of plateau was one of the main test during the production.

3.5.5 Aging test

The aging test has the purpose of check the functionality of a LST after the accumulation of high charge dose greater than the charge that will accumulate on *BABAR* detector during next years.

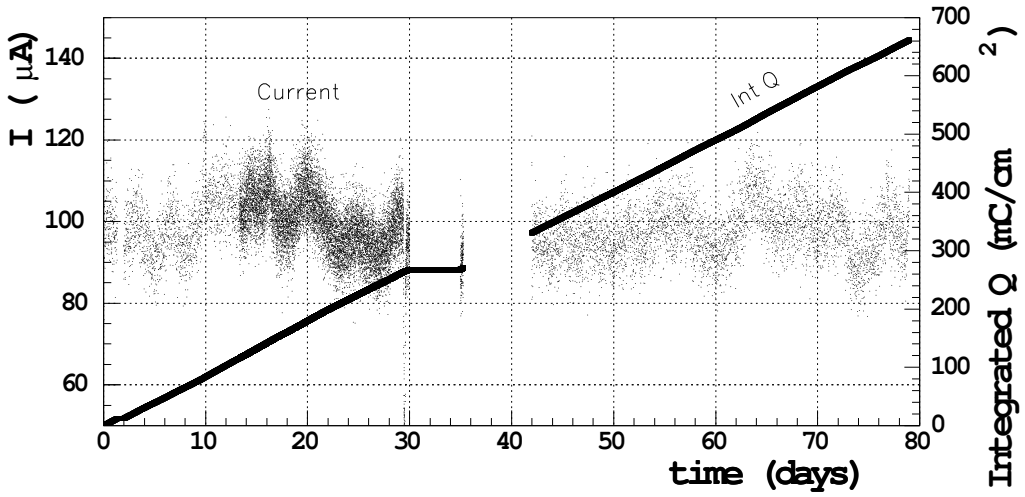

Figure 3.14: Current (left y axis) and integrated charge (right y axis) as a function of time of the LST under aging test.

In order to simulate in a small period of time a fast aging a LST is exposed at a radioactive source. We assume an accumulated charge of about 150 pC/track on LST, then the worst expected dose by the year 2010 is about 100 mC/cm^2. With the aging test we have accumulated about 650 mC/cm^2, more than six times the expected value, and just a smooth decrease in current appeared, without any big drop in signals or self-sustaining discharge. After such accumulated dose the tubes still running smoothly as it is possible to see from Fig.3.14, where we plot the current and the accumulated dose as a function of time.

3.6 Production of the LST for new barrel IFR

The total number of required LSTs for the Barrel IFR replacement is 1379 (see section 3.6), about 10% more than this number have been produced in order to have spare LSTs. Each produced LST has been tested with the quality control infrastructure.

3.6.1 Quality Control during the production

The production of all LSTs was done by Pol.Hi.Tech. in Carsoli (AQ), Italy and it toke several months between November 2003 and July 2004. The LST collaboration required high quality LSTs and for this purpose LST peoples developed a quality control system used during the production [33]. The infrastructure for this system was designed, developed and maintained by LST collaboration. The basic feature of this infrastructure was to be very user friendly, in order to allow all Pol.Hi.Tech. people to use QC stations without complicated training. The software used for the QC stations was LabView based and the communication between the operator and the computer was based on the readout of standard EAN-13 barcode.
With quality control system we inspected and tested all LSTs during the production, to reject those tubes which do not satisfy the QC requirement and also to record all data from quality control in order to have all useful information available for a classification of tubes useful for final installation.
The QC protocol requires the following tests:

1. Check of the integrity of all small parts: clips, wire holders, PCB holders and endcaps.
2. Visual inspection of the graphite coating of the profile.
3. Measurements of the resistivity on the bottom and on the walls of the graphite.
4. Record of the wire spool used in the tube.
5. Leakage test of the tube.
6. Conditioning procedure.
7. Measurements of the plateau.
8. Source scan test.
9. Long Term test.
10. Measurements of the capacitance.

The first issue does not need more explanation, then we proceed with a description of the other quality controls. All quality control stations provide a record of the results of the test which are stored on a database. This idea has been introduced in order to have a detailed history of each tube produced. From the results of all tests it is possible to do a classification of each LST, in order to choose the best LST to be installed in the most critical zone of the IFR. For example it is preferable to install the best LSTs in layer 18 (the outer layer), which is the most important for muon ID. Moreover the available history of each LST can be used to understand the causes of a

possible bad behavior.

Graphite coating inspection

After the painting of the profiles they were visually inspected in order to find rough surface, small spots, pinnacles and all other kind of defects that it is possible to find on the graphite coating. The found defects are repaired if necessary, otherwise if a defect appear not dangerous it is recorded in the database.

Resistivity measurements

After the graphite inspection the resistivity measurements on the bottom and on the walls of each profile are performed. A dedicated automatic machine (shown in Fig.3.15) has been built in order to measure the resistivity on the bottom of the cells every 50 cm. Before every session of measurements the machine starts with the measurements on a sample of coated kapton and on a sample of graphite in order to take into account variation of resistivity due to temperature and humidity variations. The measurements of the resistivity on the walls were made by hand with a dedicated probe and the measured values are recorded on the database in automatic mode. Also these measurements were done every 50 cm.

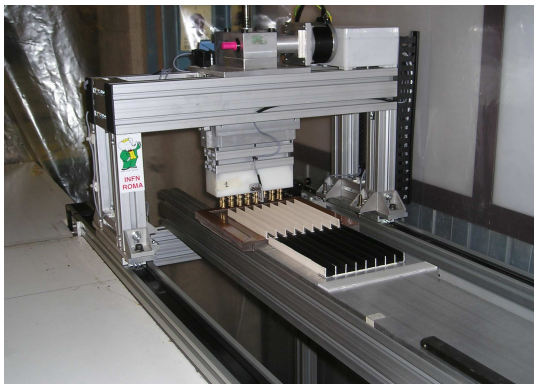

Figure 3.15: Machine for resistivity measurements on bottom of the cells.

Record of the spools

After the resistivity measurements the assembling phase starts. When the anode-wires are positioned the number of the spool corresponding to each cell is recorded in order to know which wire has been used for that cell.

Leakage test

After the assembling phase the tube is closed and then a check of possible leakage is performed putting the tube in a water tank and flowing air inside. This test has no record on database, because if a leak was found the tube was repaired, then no leak is expected at the end of the

production.

Conditioning procedure

The assembled tubes without leaks start with the high voltage test. First the LST were conditioned. The conditioning procedure is necessary in order to burn little debris inside the tube and to eliminate little spots on graphite. The procedure consists of a HV rump up in order

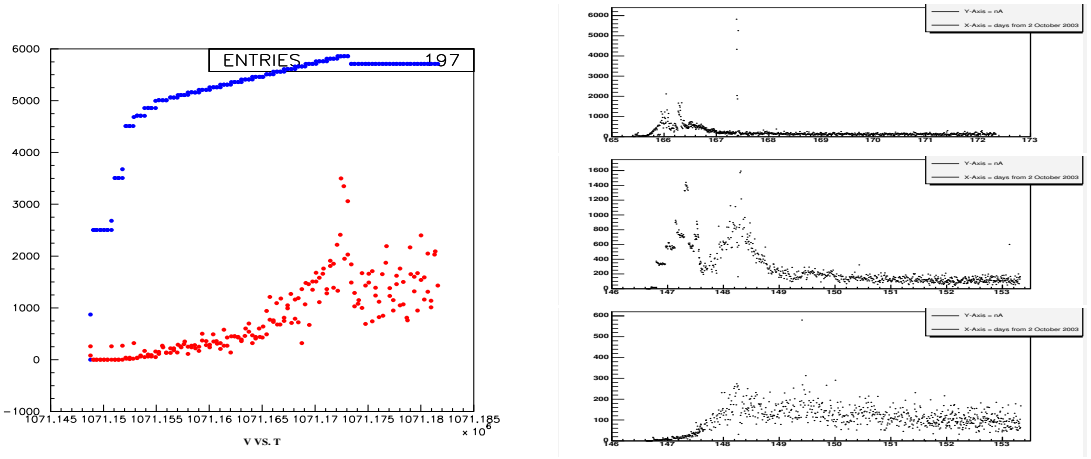

(a) (b)

Figure 3.16: Conditioning procedure:(a) Voltage (blue) and current(red) versus time. (b) Three examples of current versus time during a conditioning procedure.

to reach the maximum allowed voltage drawing a current less than 250 nA at the end of the procedure. A successful conditioning starts at 4500 V and end at 5900 V and is divided in 15 steps, each step can be repeated if the behavior of the tube is not so good. After the final step the tube kept under HV at 5700 V for a couple of days. The total conditioning procedure need about one week and it was controlled by a dedicated station. In Fig.3.16(a) we report an example of voltage and current versus time in a conditioning procedure, while Fig.3.16(b) shows three examples of current versus time during the conditioning procedure on three LST during the production. It is possible to see that the current decreases during the time: at the end of the conditioning all impurities inside the tube are burned and the current becomes low.

Plateau measurements

The plateau measurements were done on those tubes that successfully passed the conditioning. The plateau curve is obtained measuring the counting rate as function of HV, between 4900 V and 5900 V, with steps of 50 V. From the plateau curve we determine the width and the position of

the flat region and of the knees in order to have a first evaluation of the quality of the tubes. In Fig.3.17 we report examples of the plateau obtained at Pol.Hi.Tech. during the production.

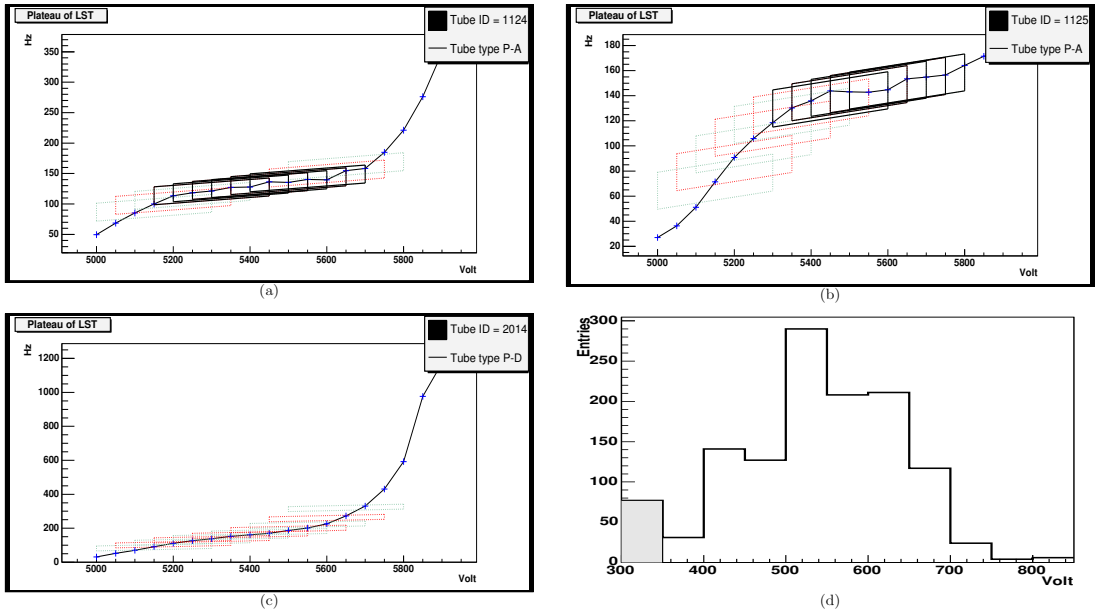

Figure 3.17: Examples of plateau curves obtained during production:(a) and (b) show good plateau; (c) shows a bad plateau; (d) is the distribution of the plateau width, LST in first bin were rejected.

Source scan test

The tubes showing a good plateau were tested with a radioactive source in order to find some defects not detected during previous phases. From the source scan test we check the presence of spikes during the scan and the presence of self-sustained discharges which can indicate a defect in the tube. In Fig.3.19 we show examples of different results from source scan test at Pol.Hi.Tech. during the production with the automatic machine showed in Fig.3.18. Fig.3.19(a) shows a good behavior of a tube without problem. Fig.3.19(b) shows the presence of a spike in current along the cell, this could be due to the presence of a pinnacle on the graphite coating. Fig.3.19(c) shows the presence of a self-sustained discharge, in fact the current still high also without the source. The causes of this effect can be various, for example a very bad surface of

Figure 3.18: Machine for source scan test.

graphite, or a large displacement of the wire or the presence inside the tube of some impurities that was not burned during the conditioning.

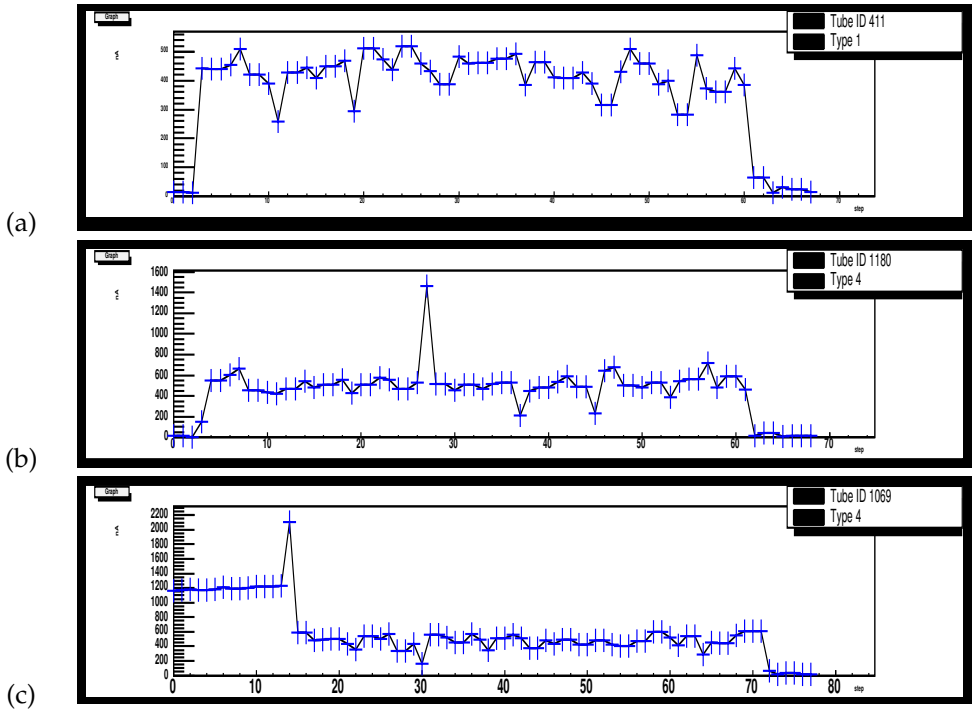

Figure 3.19: Example of source scan test during the production: (a) shows a good scan, where it is possible to see the effect of the wire holder in correspondence of a drop in current. (b) shows a scan with a spike in current, maybe due to a pinnacle on graphite coating. (c) shows a self-sustained discharge, in fact the current still high also without source on tube, as it is possible to see on the left side of the plot after the end of the tube.

Long term test

After the source scan test the tubes have been put in shipping boxes. Before the shipment the tubes undergo the long term test. The goal of this test is to keep for one month the LST at a voltage near the end of the plateau, in order to stress the tube. During this month the current is monitored in order to see if a tube tends to rise the current or if it is working with a constant current. In Fig.3.20 we show two examples of long term test: (a) shows a successful long term test characterized by low current during whole month, while (b) shows a failed long term test characterized by a large increase of the current about at the 15^{th} day, the bad situation was not recoverable, then tubes like this one were rejected.

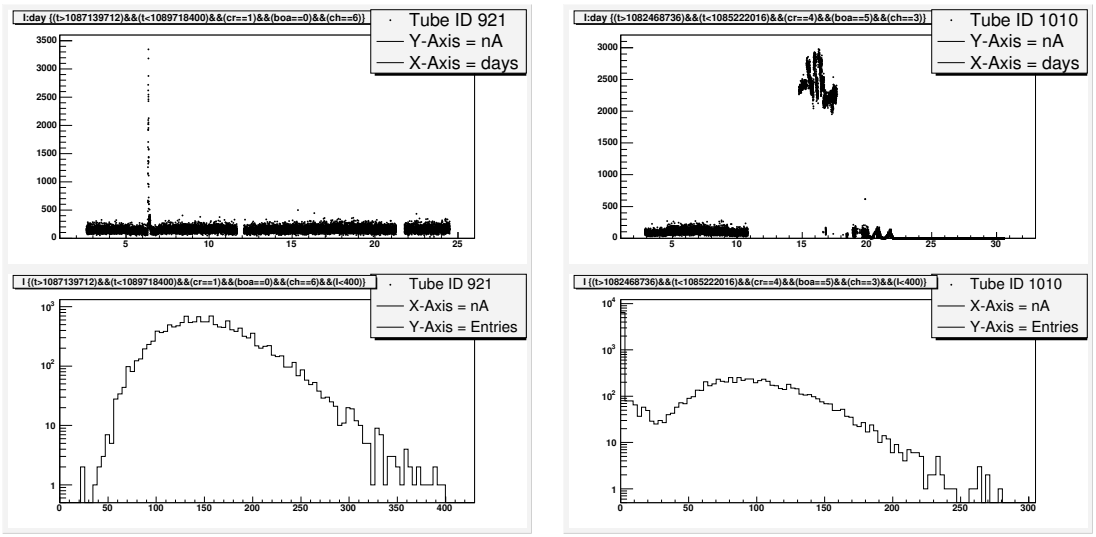

(a) (b)

Figure 3.20: Two LSTs under long term test: upper (a) and (b) show current versus time, while lower (a) and (b) show current distribution during the month of long term test. (a) good LST, (b) bad LST.

Capacitance measurements

The last operation made on LST before the shipment is the measurements of the capacitance, whose value is measured also after the shipment to check for possible damages during the sea freight.

3.7 Installation and performance of the first two sextants

During the *BABAR* summer shutdown 2004 the RPCs of two sextants of the IFR were replaced by the new detectors (the upper and the lower one). The LSTs were assembled in modules of two or three tubes in order to have the best modularity for the installation. Before the installation of the tubes the *Z*-strips were installed inside the gaps of the IFR.

3.7.1 Electronic system readout

The electronic system readout was designed and realized in order to avoid the presence of active circuits inside the iron of the detector [34]. This design allows easy access to the front end electronics. The signals for Φ coordinates are extracted from wires with decoupling circuits from HV system and they are transmitted by cables from the detector inside the iron to the crates of the front end cards. Also the induced signals on *Z*-strips plane installed below the LSTs are transmitted to the crates of front end cards by cables. The front end cards (LST-FE) provide the

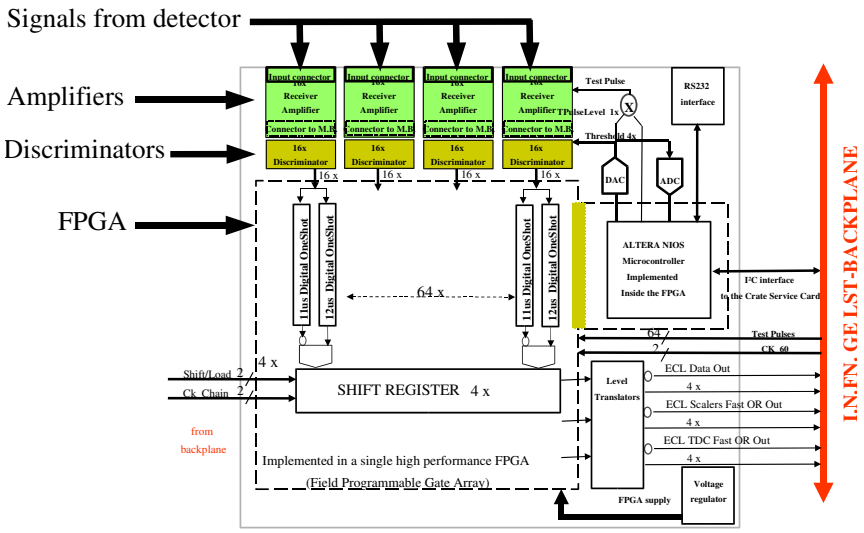

Figure 3.21: Schematic diagram of the Front End Card used for LST readout.

amplification and discrimination of the signals coming from the detector (see Fig.3.21). The front end cards have the feature of programmable thresholds. The mother board containing the front end cards is also equipped with an FPGA (Filed Programmable Gate Array) component, which provides the needed latency and time-windowing for the generation of the hit information. The FPGA also controls the transmission of the hit information in response to the DAQ-driven readout control signals. In Fig.3.21 we report the block scheme of the front end cards, where it is possible to see the different stages: amplification, discrimination, manipulation of hit information and transmission.

3.7.2 Tuning of the thresholds

In order to choose the best threshold to optimize the signal to noise ratio we looked at the single rate and noise rate, due to cosmics rays as a function of the thresholds. In Fig.3.22 we report the results obtained from the threshold scan made after the installation of the two sextant of LSTs. It appears clear that the plateau region starts at 600 mV for the signal rate, while the noise is low up to 300 mV.

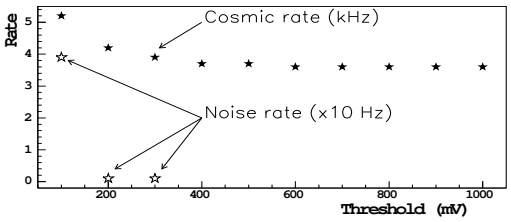

Figure 3.22: Rate for cosmics signal and noise versus threshold.

3.7.3 Plateau curves and efficiency

Concerning the performances of the two sextants with LSTs we show in Fig.3.23 typical singles rate measurements for some LST versus HV values and in Fig.3.24 the efficiency of different layers as function of HV. From these plots we can see that the performances of LSTs installed are very good. Up to now (Feb 2005) the two new sextants of the barrel with LSTs have not yet tested with beam, because an accident happened at SLAC three month ago which causes a delay in the startup of the new run of the *BABAR* experiment.

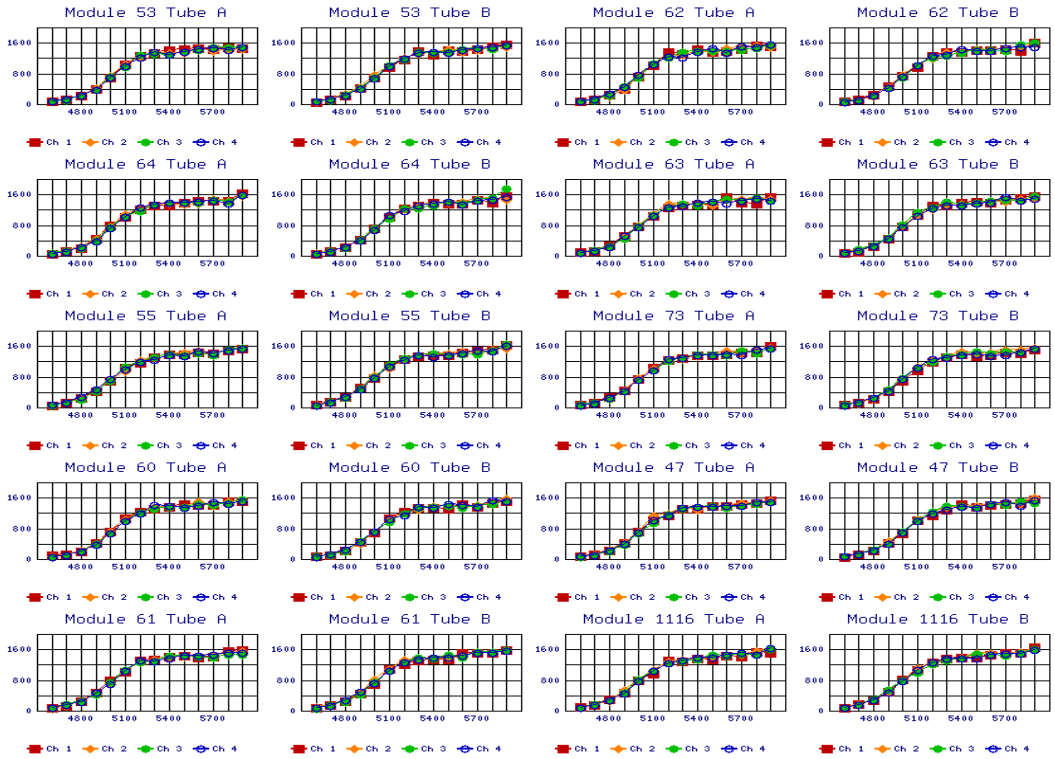

Figure 3.23: Plateau measurements with cosmics of all layers with LSTs.

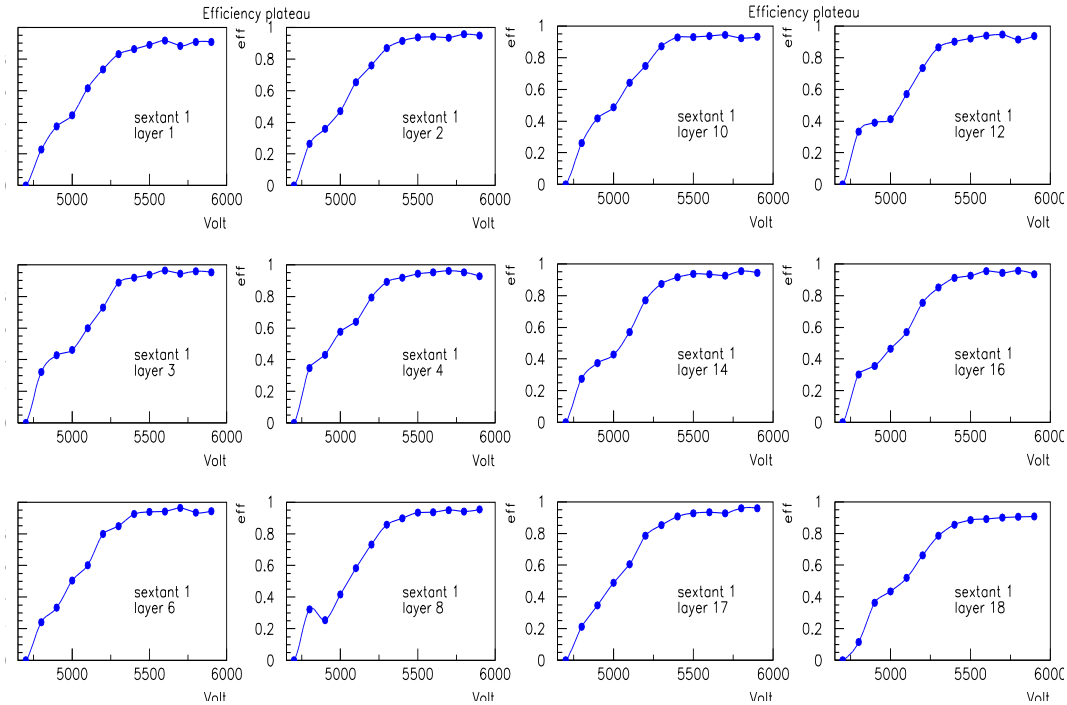

Figure 3.24: Efficiency measurements of layers with LSTs (top sextant).

Chapter 4

Study of the partially reconstructed $D^{*-}\ell^{+}\nu_{\ell}$ decay

In this chapter we will describe the technique developed in order to reconstruct the $D^{*-}\ell^{+}\nu_{\ell}$ final state using only the lepton and the soft pion from the D^{*} decay. The detection of the correct pion in the final state is crucial for this analysis.

4.1 Event reconstruction

The aim of the analysis is to select $B^0 \to D^{*-}\ell^{+}\nu_{\ell}$ decays using the partial reconstruction of the D^{*} on the recoil of a fully reconstructed B. The requirement of a fully reconstructed B will reduce the selection efficiency, resulting in a higher statistical error, while the systematic errors will be reduced by the partial reconstruction of the D^{*}. Reconstructing the D^{*} with the soft pion only means that we do not have to reconstruct the D^0, then we do not introduce systematic errors due, for instance, to the reconstruction of the particles coming from the D^0 decay. Therefore the partial reconstruction of D^{*} mesons, in events with one fully reconstructed B, gives higher statistical error and lower systematic error with respect to the exclusive D^{*} reconstruction [1] , but the statistical error can be decreased as more data will be collected. The exclusive reconstruction of D^{*} mesons gives measurements which are already systematically limited.
One of the variables useful to identify $B^0 \to D^{*-}\ell^{+}\nu_{\ell}$ decays is the squared invariant mass of the neutrino (M_{ν}^2) which has to be equal to zero. It can be calculated from p_{ν}:

$$p_{\nu} = p_B - p_{D^*} - p_l \tag{4.1}$$

where p_B is calculated from the 4-momentum of the fully reconstructed B (B_{reco}) and the 4-momentum of the Υ: $p_B = p_{\Upsilon} - p_{\overline{B}}$. The lepton 4-momentum is known, while the 4-momentum of the D^{*} is calculated by reconstructing the meson in the $D^{*} \to D^0\pi_s$ decay by using only the

[1] technique commonly used in previous measurements.

momentum of the π_s . The event reconstruction is based on two main steps: the full reconstruction of one B and the partial reconstruction of the signal on the recoiling B. The reconstruction of the lepton and the partial reconstruction of D^* by means of the soft pion are the core of the analysis. In the next two subsections we will describe the full reconstruction of one B and the lepton selection, while a dedicated section will follow concerning the partial reconstruction of the D^*.

4.1.1 The fully reconstructed B

The full reconstruction of one B (B_{reco}) is obtained by looking at its hadronic decays [42]. B_{reco} decays are of the type $B \rightarrow \overline{D}Y$, where D refers to a charm meson and Y represents a collection of hadrons with a total charge ± 1, composed as follows:

$$n_1\pi^{\pm} + n_2K^{\pm} + n_3K_s^0 + n_4\pi^0 \tag{4.2}$$

where $n_1 + n_2 < 6$, $n_3 < 3$ and $n_4 < 3$. Using D^- and D^{*-} ($\overline{D}^0$ and $\overline{D}^{*0}$) as seeds for B^0 (B^+) decays, about 1000 different decay chains are reconstructed. All decay chains are grouped into 53 categories of decays which are characterized by different signal purity, depending on the multiplicity and on the composition of the hadrons making up the Y system. In events with more than one reconstructed B decay, the decay mode with the highest *a priori* purity is selected. The total number of modes is given by the sum over the four charm seeds of the product of the number of decay modes of a given seeds (d_i) by the number of decay modes of the associated Y system for this seed (y_i): $\sum_{i=1}^{4} d_i y_i$. The decay modes are sorted and accumulated in order of decreasing purity, then four subsamples differentiated by *integrated purity* P_I of the events are created:

- **superblock-1** with decays of $P_1 > 80\%$
- **superblock-2** with decays of $P_2 > 50\%$
- **superblock-3** with decays with single mode purity $> 10\%$
- **superblock-4** all remaining modes.

The full reconstruction efficiency is 0.3% and 0.5% for $B^0\overline{B}^0$ and B^+B^- events respectively. The kinematic consistency of a B_{reco} candidate is checked using two variables, the beam-energy-substituted mass ($m_{\rm ES}$) and the energy difference (ΔE) defined as:

$$m_{ES} = \sqrt{\tfrac{s}{4} - \vec{p}_B^{\,2}} \tag{4.3}$$

$$\Delta E = E_B - \tfrac{\sqrt{s}}{2} \tag{4.4}$$

where $\sqrt{s}$ is the total energy in the $\Upsilon(4S)$ center of mass frame, $\vec{p}_B$ and E_B are respectively the momentum and energy of the B in the same frame. For correctly reconstructed B decays, the $m_{\rm ES}$ distribution peaks at B meson mass, while ΔE is consistent with zero ($\Delta E = 0$ will be

required within three standard deviations). The number of events characterized by a correctly reconstructed B and background events from continuum and wrong particle combinations are extracted performing a fit to the $m_{\rm ES}$ distribution with the sum of a Crystal-Ball function for the peak and an ARGUS function for the background. For a detailed description of the $m_{\rm ES}$ fit see App.B. In the analysis we use all events contained in **superblock-3**.

4.1.2 Lepton reconstruction

The reconstruction of the lepton coming from the B recoiling against a fully reconstructed B will be used in order to select the total number of semileptonic events and for the signal selection. The lepton reconstruction of the *BABAR* detector is very efficient. Using the Monte Carlo simulation we find that 98% of the leptons in the acceptance region are reconstructed as good tracks, with the same efficiency for electrons and muons. The lepton daughter of B needs to be discriminated from the leptons coming from the semileptonic decays of secondary particles, like D mesons. A good discrimination can be obtained by looking at the momentum distribution of the lepton coming from B compared with other leptons. Fig.4.1(a) shows the momentum distribution for leptons

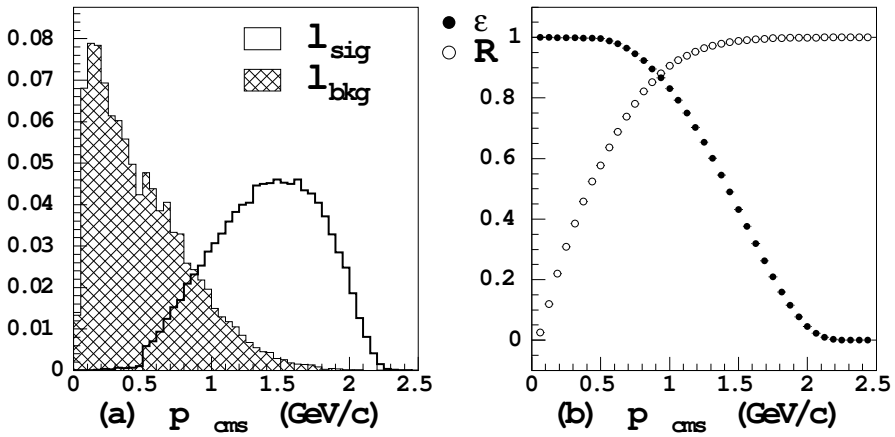

Figure 4.1: (a) Center of mass momentum distribution for lepton daughter of B (white area) and for lepton non-directly coming from B (cross-hatched area). (b) Efficiency for signal leptons selection ($\bullet$ ϵ) and rejection of background leptons ($\circ$ R) as a function of the lepton momentum lower cut.

from a B (white area) and for other leptons (cross-hatched area) in the center of mass frame. From this plot it is clear that the requirement $|\vec{p}^{\,\ell}_{cms}| > 1$ GeV allows to reject an high fraction of wrong leptons. In Fig.4.1(b) we report the efficiency for good leptons ($\bullet$ ϵ) and the rejection factor ($\circ$ R) for wrong leptons as a function of the lower limit on lepton momentum. Using $|\vec{p}^{\,\ell}_{cms}| > 1$ GeV we obtain a selection efficiency for good leptons of about 85% and a rejection factor for wrong leptons of about 90%. In order to select the right lepton in events in which more candidates satisfy the momentum cut we select the highest momentum lepton. From Monte Carlo simulation we obtain

that the lepton coming from B has the highest momentum in 98% of the events with more than one lepton.

4.1.3 Lepton identification

Charged leptons, pions and kaons are identified by building selectors which combine different particle identification criteria (PID):

- Specific ionization ($\frac{dE}{dx}$) inside the SVT and the DCH;
- Čerenkov angle and number of photons inside the DIRC;
- $\frac{E}{p}$ ratio, where E is the energy released inside the EMC and p is the momentum of the track associated to the cluster (this method is mainly used for electron identification);
- The path traveled by a given particle inside the iron and its relative cluster multiplicity in the IFR (mainly used for pion and muon identification).

Different lists of particles can be defined accordingly to the requirements applied by PID selectors: for instance, a tight selection for lepton produces the $eMicroTight$ or $muMicroTight$ lists, for electrons and muons respectively, while a kaon tight selection performed with a neural network algorithm produces the $NNTight$ list. Tight lists are commonly used when the combinatorial background is expected to be high, for instance, in the reconstruction algorithm of B candidates with high multiplicity modes, and the corresponding loss of efficiency results in a high gain in purity.

Electron Identification

Electrons are identified using a likelihood-based selector [41], which uses a number of discriminating variables:

- E_{cal}/p_{lab}, the ratio of E_{cal}, the energy deposited in the EMC, and p_{lab} the momentum in the laboratory rest frame measured using the tracking system;
- LAT, the lateral shape of the calorimeter deposit defined in eq.4.6;
- $\Delta\Phi$, the azimuthal distance between the centroid of the EMC cluster and the impact point of the track on the EMC;
- N_{cry}, the number of crystals in the EMC cluster;
- dE/dx, the specific energy loss in the DCH;
- the Čerenkov angle θ_C and N_C, the number of photons measured in the DIRC.

First, muons are eliminated based on $d\mathrm{E}/dx$ and the shower energy relative to the momentum. For the remaining tracks, likelihood functions are computed assuming the particle is an electron, pion, kaon, or proton. These likelihood functions are based on probability density functions that are derived from data control samples of high purity for each discriminating variable. For hadrons, we take into account the correlations between energy and shower shapes. Using combined likelihood functions

$$\begin{aligned} L(\xi) &= P(E/p, LAT, \Delta\Phi, dE/dx, \theta_C|\xi) \\ &= P_{Emc}(E/p, LAT, \Delta\Phi|\xi)\ P_{Dch}(dE/dx|\xi)\ P_{DRC}(\theta_C|\xi) \end{aligned}$$

for the hypotheses $\xi \in \{e, \pi, K, p\}$, the fraction

$$F_{\mathrm{e}} = \frac{f_{\mathrm{e}} L(\mathrm{e})}{\sum_\xi f_\xi L(\xi)}\ , \tag{4.5}$$

is defined where, for the relative particle fractions, $f_{\mathrm{e}} : f_\pi : f_{\mathrm{K}} : f_{\mathrm{p}} = 1 : 5 : 1 : 0.1$ is assumed. A track is identified as an electron if $F_{\mathrm{e}} > 0.95$. The lateral shape of the calorimeter deposit (LAT) is defined as follows:

$$LAT = \frac{\sum_{i=3}^{N} E_i r_i^2}{\sum_{i=3}^{N} E_i r_i^2 + E_1 r_0^2 + E_2 r_0^2} \tag{4.6}$$

where N is the number of crystals associated to the electromagnetic shower, $r_0 \sim 5\ cm$ is the mean distance between two crystals, E_i is the energy associated in the i-th crystal and r_i is the distance between the center of the shower and the center of the i-th crystal in the plane perpendicular to the line pointing from the interaction point to the shower center. The electron identification effi-

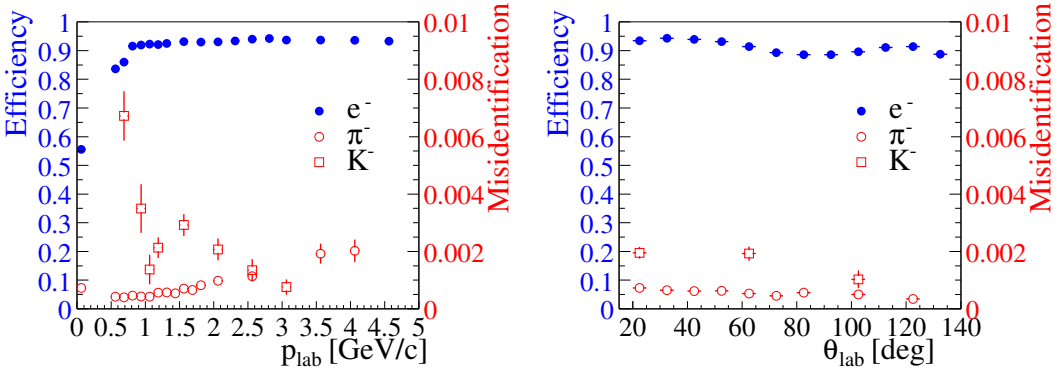

Figure 4.2: Electron identification and hadron misidentification probability for the likelihood-based electron selector as a function of momentum (a) and polar angle (b). Note the different scales for identification and misidentification on the left and right ordinates, respectively. The measurements are for luminosity-averaged rates for data taken from year 1999 to 2003.

ciency has been measured using radiative Bhabha events, as a function of laboratory momentum p_{lab} and polar angle θ_{lab}. The misidentification rates for pions, kaons, and protons are extracted from selected data samples. Pure pions are obtained from kinematically selected $K^0_S \to \pi^+\pi^-$ decays and three prong $\tau^\pm$ decays. Two-body Λ and D^0 decays provide pure samples of protons and charged kaons. The performance of the likelihood-based electron identification algorithm is summarized in Fig.4.2, in terms of the electron identification efficiency and the probability that an hadron is misidentified as an electron.

Muon Identification

The muon selection procedure is as follows:

- tight criteria on tracking are applied: $p_\perp > 0.1$ GeV, $N_{Dch} \geq 12$, $0.360 < \theta_{lab} < 2.37$ and $p_{lab} > 1.0$ GeV
- the energy deposited in the EMC is required to be consistent with a minimum ionizing particle, $50 \text{ MeV} < E_{cal} < 400 \text{ MeV}$;
- the number of IFR layers that have an hit associated to the track (N_L) has to be $N_L \geq 2$.
- the interaction length of material traversed by the track has to be $\lambda_{meas} > 2.2$. The number of interaction lengths expected for a muon of the measured momentum and angle to traverse the IFR is estimated by extrapolating the track up to the last *active* layer of the IFR. This estimate takes into account the RPC efficiencies which are routinely measured and stored. For the difference $\Delta\lambda = \lambda_{exp} - \lambda_{meas}$ we require $\Delta\lambda < 1.0$, for tracks with momentum greater than 1.2 GeV. For track momenta between 0.5 GeV and 1.2 GeV, a variable limit is placed: $\Delta\lambda < [(p_{lab} - 0.5)/0.7]$.
- The *continuity* of the IFR cluster is defined as $T_c = \frac{N_L}{L-F+1}$, where L and F are the last and first layers with hits. This variable is mainly used to reject events in which spurious hits from machine background, mainly appearing in the forward region, are associated to a pion cluster: in this case the number of interaction lengths becomes similar to the one expected for a muon, but the continuity of the track can still discriminate between the fake muon, $T_c \leq 1$, and a true muon penetrating an ideal detector, for which T_c is expected to be 1.0. We thus require $T_c > 0.3$ for tracks with $0.3 < \theta_{lab} < 1.0$.
- The observed number of hit strips in each RPC layer is used to impose the conditions on the average number of hits, $\bar{m} < 8$, and the standard deviation, $\sigma_m < 4$.
- The strip clusters in the IFR layers are combined to form a track and fit to a third degree polynomial, with the quality of the fit selected by the condition $\chi^2_{fit}/DOF < 3$. In addition,

the cluster centroids are compared to the extrapolated charged track, with the requirement $\chi^2_{trk}/DOF < 5$.

The muon identification efficiency has been measured using $\mu^+\mu^-(\gamma)$ events and two-photon production of $\mu^+\mu^-$ pairs. The misidentification rates for pions, kaons, and protons are extracted from selected data samples. The performance of the muon identification algorithm is summarized in Fig.4.3, in terms of the muon identification efficiency and the per track probability that a hadron is misidentified as a muon. Only tracks in the fiducial volume, i.e. with a polar angle in the range $20.6 < \theta_{lab} < 135.9°$, are considered. The errors shown are statistical only, the systematic error is dominated by variations in the performance of the IFR as a function of position and time.

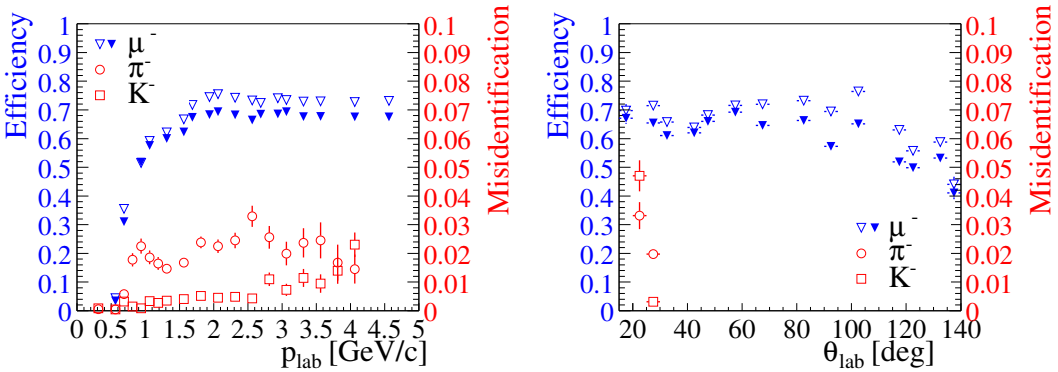

Figure 4.3: Muon identification and hadron misidentification probability for the tight muon selector as a function of momentum (a) and polar angle (b). The solid markers indicate the efficiency in 2000, the empty markers the efficiency in 2001. Note the different scales for identification and misidentification on the left and right ordinates, respectively.

4.2 Partial reconstruction of D^* mesons

The partial reconstruction of the D^* using only soft pion information is based on some approximations, which can be studied in order to choose the best one. In laboratory frame the soft pion is produced in a restricted cone around the direction of the D^*. Therefore, it is a good approximation to consider the soft pion to have the same direction of the D^*. This assumption allows us to calculate the boost of D^* in laboratory frame from the measured momentum of the soft pion in the same frame:

$$\begin{pmatrix} E^{lab}_{D^*} \\ \vec{p}^{\,lab}_{D^*} \end{pmatrix} = \begin{pmatrix} \gamma_{D^*} & \gamma_{D^*}\beta_{D^*} \\ \gamma_{D^*}\beta_{D^*} & \gamma_{D^*} \end{pmatrix} \begin{pmatrix} m_{D^*} \\ \vec{0} \end{pmatrix} \tag{4.7}$$

β_{D^*} can be calculated solving one the two equations 4.8 which contain the momentum of the soft pion in the laboratory frame:

$$\begin{pmatrix} E^{lab}_{\pi_s} \\ \vec{p}^{\,lab}_{\pi_s} \end{pmatrix} = \begin{pmatrix} \gamma_{D^*} & \gamma_{D^*}\beta_{D^*} \\ \gamma_{D^*}\beta_{D^*} & \gamma_{D^*} \end{pmatrix} \begin{pmatrix} E^{*}_{\pi_s} \\ \vec{p}^{\,*}_{\pi_s} \end{pmatrix} \tag{4.8}$$

where $E^*_{\pi_s}$ is the energy of soft pion in the D^* rest frame:

$$E^*_{\pi_s} = \frac{m^2_{D^*} - m^2_{D^0} + m^2_\pi}{2m_{D^*}} = 145 \text{ MeV} \tag{4.9}$$

The first equation of 4.8:

$$E^{lab}_{\pi_s} = \gamma_{D^*} E^*_{\pi_s} + \gamma_{D^*}\beta_{D^*}\vec{p}^*_{\pi_s} \tag{4.10}$$

has the following two solutions for β_{D^*}:

$$\beta^\pm_{D^*} = \frac{E^{lab}_{\pi_s}\left|\vec{p}^{lab}_{\pi_s}\right| \pm E^*_{\pi_s}\left|\vec{p}^*_{\pi_s}\right|}{E^{*2}_{\pi_s} + \left|\vec{p}^{lab}_{\pi_s}\right|^2} \tag{4.11}$$

A different approximation can be used assuming $\vec{p}^*_{\pi_s} \approx 0$, then we can calculate the boost of D^* with this simple relation:

$$\gamma^{app}_{D^*} = \frac{E^{lab}_{\pi_s}}{E^*_{\pi_s}} \tag{4.12}$$

From Monte Carlo we know the real boost of D^*, then we can determine which solution gives the smallest uncertainty. In Fig.4.4 we compare the distributions of the γ factors obtained from the three calculations.

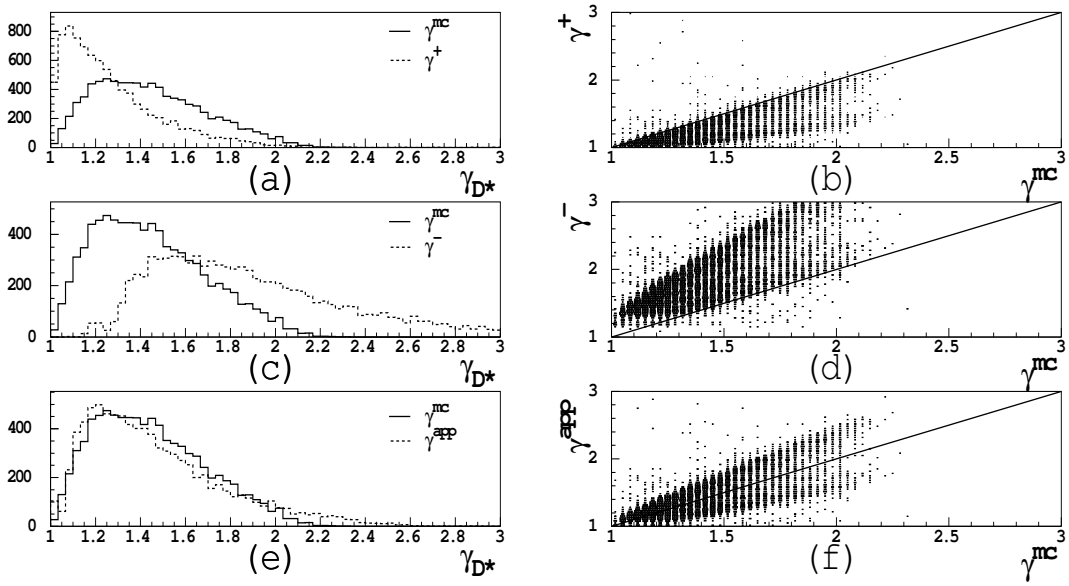

Figure 4.4: Distribution of γ_{D^*}: solid line indicates $\gamma^{mc}_{D^*}$, dashed line $\gamma^{reco}_{D^*}$, where $reco$ means the three different solutions. (a) and (b) comparison between $\gamma^{mc}_{D^*}$ and $\gamma^+_{D^*}$, (c) and (d) comparison between $\gamma^{mc}_{D^*}$ and $\gamma^-_{D^*}$, (e) and (f) comparison between $\gamma^{mc}_{D^*}$ and $\gamma^{app}_{D^*}$.

From Fig.4.4 the distribution of $\gamma^{app}_{D^*}$ appears more similar to the distribution of $\gamma^{mc}_{D^*}$ than the distribution of the other solutions, but for a better understanding we have to look at the differences $|\gamma^{mc}_{D^*} - \gamma^{reco}_{D^*}|$ shown in Fig.4.5. From Fig.4.5(a) it appears that the distribution of $\left|\gamma^+_{D^*} - \gamma^{mc}_{D^*}\right|$

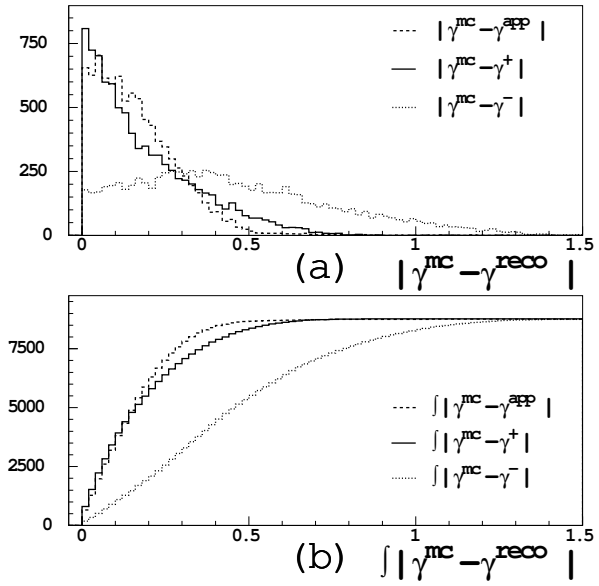

Figure 4.5: (a) Distribution of $|\gamma^{mc}_{D^*} - \gamma^{reco}_{D^*}|$, (b) distribution of $\int |\gamma^{mc}_{D^*} - \gamma^{reco}_{D^*}|$: solid, dashed and dotted lines indicate $|\gamma^{mc}_{D^*} - \gamma^{app}_{D^*}|$, $\left|\gamma^{mc}_{D^*} - \gamma^{+}_{D^*}\right|$ and $\left|\gamma^{mc}_{D^*} - \gamma^{-}_{D^*}\right|$ respectively.

is narrow than the others, but we can note that this distribution has more tail than the distribution of $|\gamma^{app}_{D^*} - \gamma^{mc}_{D^*}|$, then in order to understand which is the best calculation we can look at the integral of the previous distribution as a function of the value of $|\gamma^{reco}_{D^*} - \gamma^{mc}_{D^*}|$, showed in Fig.4.5(b) This function tells us the numbers of events which have $|\gamma^{reco}_{D^*} - \gamma^{mc}_{D^*}|$ less than a given value. From the integral we see that for a given value of $|\gamma^{reco}_{D^*} - \gamma^{mc}_{D^*}|$ we have more events for the approximate solution than for the positive one.
From the above discussion the best solution seems to be the approximate one, but we have to stress that γ is needed in order to calculate the invariant mass of the neutrino. In the calculation of M^2_ν we have contributions not only from γ, but also from the reconstruction of the lepton and the B_{reco}, so we have to compare the M^2_ν calculated with the three solutions with the value of M^2_ν calculated with the real value of γ in order to determine the best approximation. Fig.4.6 shows four different M^2_ν distributions: positive solution (solid line), negative solution (dotted line), approximate solution (dashed line) and the real value γ_{MC} (cross-hatched area).

The distribution of M^2_ν calculated with the positive solution of eq.4.11 appears narrower than the other distributions. A comparison of the $\left|M^2_{\nu det} - M^2_{\nu mc}\right|$, where $M^2_{\nu det}$ is computed with the three solutions and $M^2_{\nu mc}$ uses the real boost of D^* taken from Monte Carlo, is shown in Fig.4.7. As before we also show the integral of the distributions.

In order to find the best solution to use in the final analysis we look at the fraction of events which has the minimum values of $\left|M^2_{\nu det} - M^2_{\nu mc}\right|$ between the three different calculation of

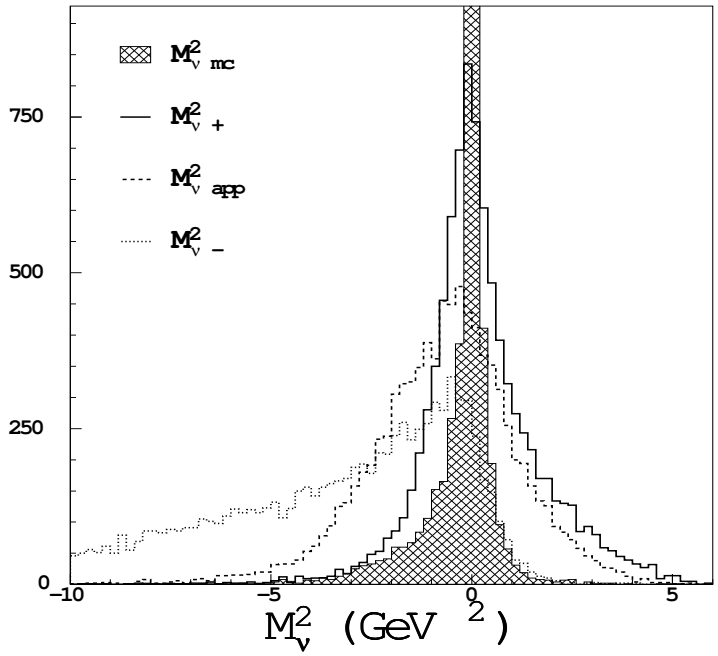

Figure 4.6: M^2_ν distributions for different solutions: positive solution (solid line), negative solution (dotted line), approximate solution (dashed line) and distribution obtained from real value of γ_{MC} (cross-hatched area).

$M^2_{\nu det}$. The fraction of events where each solution is closer to the generated values of γ and M^2_ν are shown in Tab.4.1 and Tab.4.2 respectively.

Solution type	Fraction (%) with best $\gamma^{reco}_{D^*}$ between three solutions	Fraction (%) with best $\gamma^{reco}_{D^*}$ between two solutions $\pm$
$\gamma^{+}_{D^*}$	38.4 ± 0.7	73.1 ± 0.9
$\gamma^{-}_{D^*}$	18.4 ± 0.5	26.9 ± 0.6
$\gamma^{app}_{D^*}$	43.3 ± 0.7	

Table 4.1: Fraction of events where the calculated γ is closest to the real one for $D^{*-}\ell^+\nu_\ell$ events, for the three calculations described in the test.

Solution type	Fraction (%) with best $M^2_{\nu reco}$ between three solutions	Fraction (%) with best $M^2_{\nu reco}$ between two solutions $\pm$
$M^{2+}_{\nu det}$	53.1 ± 0.8	74.7 ± 0.9
$M^{2-}_{\nu det}$	18.8 ± 0.5	25.3 ± 0.5
$M^{2App}_{\nu det}$	28.1 ± 0.6	

Table 4.2: Fraction of events where the calculated M^2_ν is closest to the real one for $D^{*-}\ell^+\nu_\ell$ events, for the three calculations described in the test.

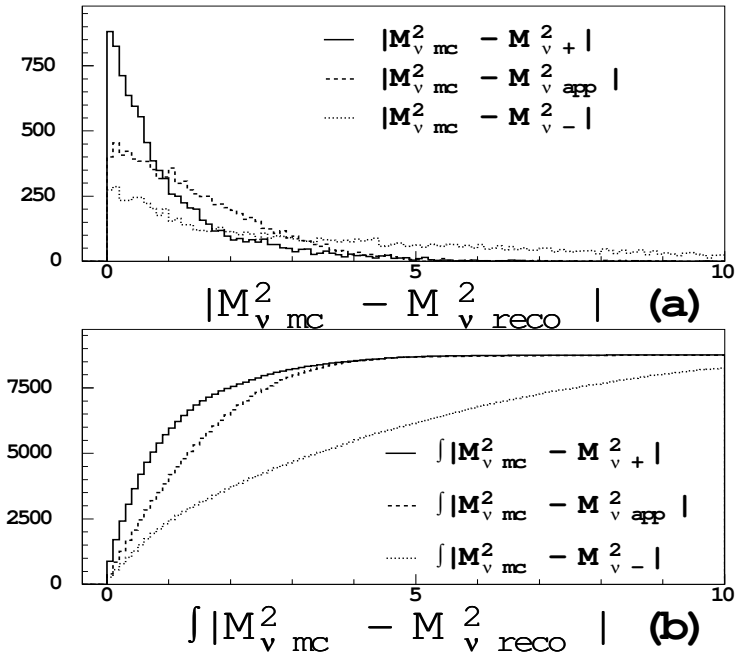

Figure 4.7: (a) Distribution of $\left|M^2_{\nu,mc} - M^2_{\nu,reco}\right|$, (b) distribution of $\int \left|M^2_{\nu,mc} - M^2_{\nu,reco}\right|$: solid, dashed and dotted lines correspond to $M^2_{\nu,app}$, $M^2_{\nu,+}$ and $M^2_{\nu,-}$ respectively.

From the above discussion it appears that the value of γ which gives the value of M^2_ν closest to the value calculated from Monte Carlo simulation is the positive solution. Therefore we decide to choose the positive solution for γ in the final analysis.

4.3 Soft pion studies

We need a specific technique in order to distinguish the soft pion coming from D^* from other pions in the final state, for example pions from D decays.

4.3.1 Reconstruction efficiency of the soft pion

In order to calculate the reconstruction efficiency for pion tracks coming from D^* in a $B^0 \to D^{*-}\ell^+\nu_\ell$ decay we compare the number of detected pions (reconstructed as good tracks) with the total number of pions, requiring that all pions are in the geometrical acceptance ($0.410 < \theta < 2.54$).

We find that the soft pion is not reconstructed in 35% of the events. The reconstruction efficiency is a function of the pion momentum, in fact as we can see from Fig.4.8(c)(d) the efficiency increases with increasing momentum. Fig.4.8(a)(b) shows in solid-line the distribution of p_{cms} for all pions generated in the acceptance region, while the same distribution for the detected pions is shown

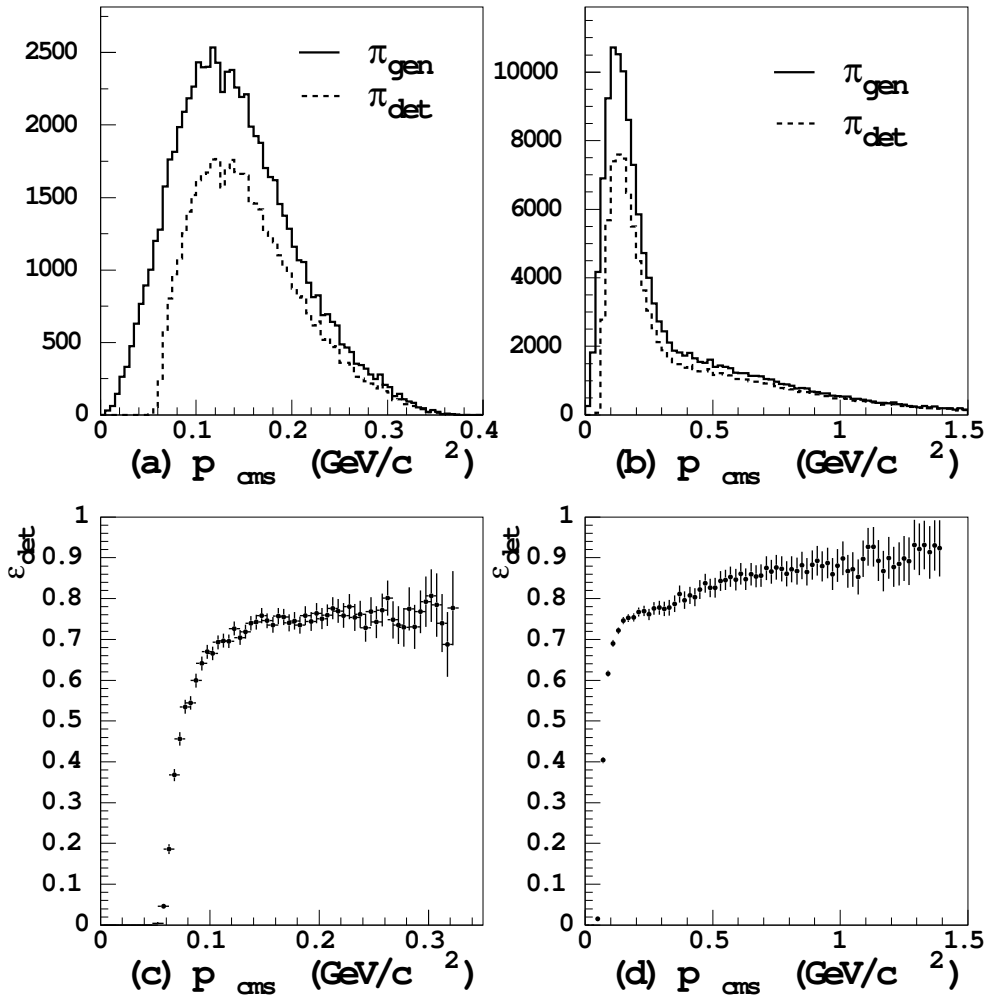

Figure 4.8: Center of mass momentum distribution of π_s from (a) $D^{*-}\ell^+\nu_\ell$ events and (b) all pions: generated momentum (solid line) and detected momentum (dotted line). Detection efficiency as a function of momentum for π_s from (c) $D^{*-}\ell^+\nu_\ell$ and (d) all pions, respectively.

in dashed-line; (a) corresponds to the soft pion in $D^{*-}\ell^+\nu_\ell$ decays, while (b) corresponds to all pions. The ratio between these distributions is the efficiency versus p_{cms} shown in Fig.4.8(c)(d). It is clear from this figure that it is hard to reconstruct pions with momentum lower than 80 MeV, where a non-negligible fraction of signal events is located.

4.3.2 Characterization of π_s and other pions

In order to have a discrimination between detected soft pions coming from D^* in $B^0 \to D^{*-}\ell^+\nu_\ell$ decays and background pions we can use two variables: the pion momentum (p_{cms}) in CMS frame and M_ν^2 . In Fig.4.9(a) and (b) we compare the distributions of p_{cms} and M_ν^2 respectively, for the

detected soft pions coming from D^* in a $B^0 \to D^{*-}\ell^+\nu_\ell$ decays and for background pions; scatter plots of M_ν^2 versus p_{cms} are shown in Fig.4.9(c)(d). Fig.4.10 shows the pion selection efficiency and the rejection factor for background pions as a function of an upper cut on p_{cms} and as a function of a lower cut on M_ν^2 .

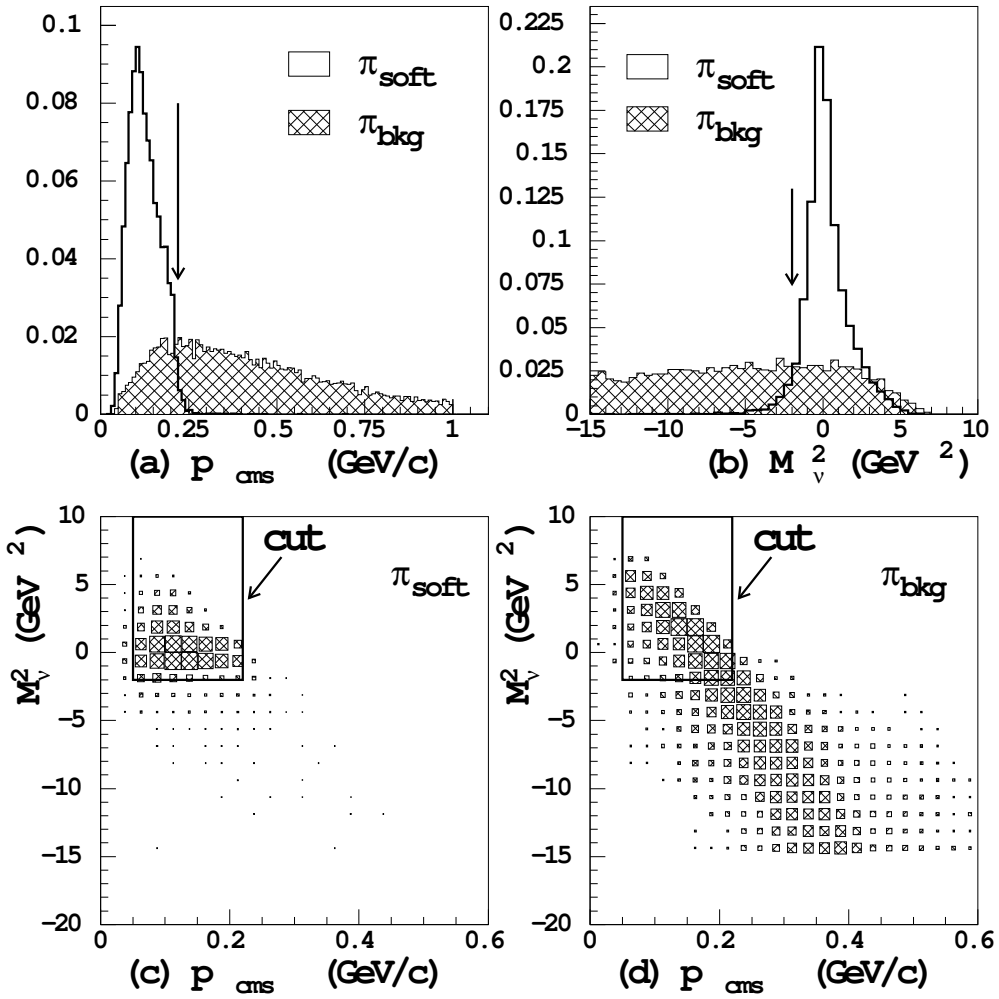

Figure 4.9: (a) Center of mass momentum distribution and (b) M_ν^2 distribution calculated with right π_s (white area) in $D^{*-}\ell^+\nu_\ell$ events and with a wrong pion (cross-hatched area) in all events. (c) and (d) scatter plot for p_{cms} (x axis) and M_ν^2 (y axis) for signal and background events respectively.

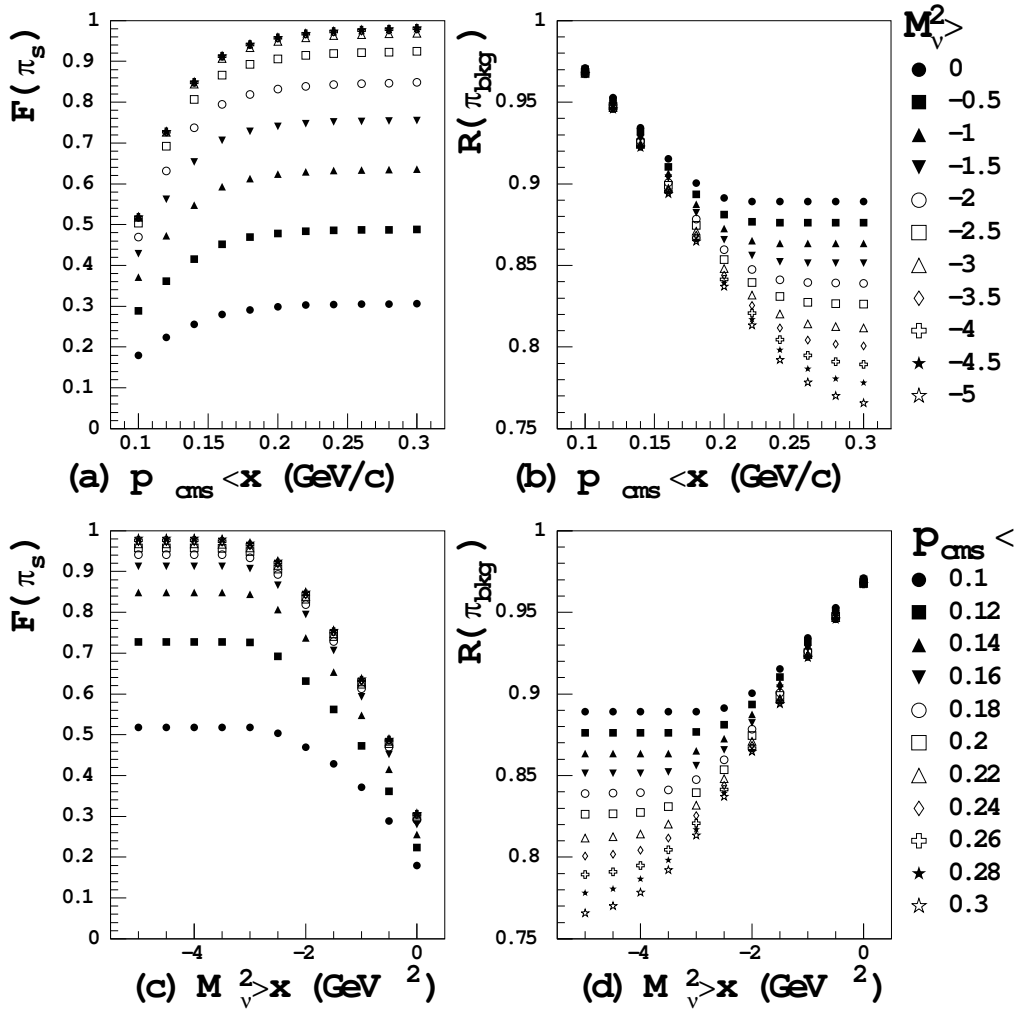

Figure 4.10: (a) and (b) Fraction of surviving π_s and rejected background pions, respectively, as a function of cut on p_{cms} for different values of cut on M^2_ν . (c) and (d) Fraction of surviving π_s and rejected background pions, respectively, as a function of cut on M^2_ν for different values of cut on p_{cms}.

4.4 Optimization of the soft pion selection

As shown in the previous section the cuts on p_{cms} and on M_ν^2 allow to reject a significant amount of background pions, but do not allow to select the soft pion from other background pions which survive the cuts in the same event. There is not an optimal method which can be used in order to select the best pion with a 100% signal efficiency. We studied 4 different methods using p_{cms} and M_ν^2 to select a single candidate pion per event:

- Method 1.1: we choose the charged track with $p_{cms,min}$, then we apply the cuts on p_{cms} and M_ν^2 .
- Method 1.2: we choose the charged track with $p_{cms,min}$ between those tracks that satisfy cuts on p_{cms} and M_ν^2 .
- Method 2.1: we choose the charged track with $M^2_{\nu,min}$ (closest to zero), then we apply the cuts on p_{cms} and M_ν^2 .
- Method 2.2: we choose the charged track with $M^2_{\nu,min}$ between those tracks that satisfy cuts on p_{cms} and M_ν^2 .

In order to compare the four methods, choose the best one and optimize the selection criteria on p_{cms} and M_ν^2 we have to study in detail the composition of the selected events, the selection efficiency for signal events and the background rejection. An useful variable to choose the best method and the best values for the cuts on p_{cms} and M_ν^2 is the ratio between the number of selected signal events and the sum of selected signal and background events:

$$SB = \frac{N_{sel}^{Sig}}{\sqrt{N_{sel}^{Sig} + N_{sel}^{bkg}}} \tag{4.13}$$

the maximum of this variable will correspond to the optimal selection criteria.

Concerning the composition of the selected sample, it can be shown that the four methods are equivalent. First we divide the signal events in 5 different samples, defined in terms of different outcomes for the soft pion selection π_{sel}:

1. $\pi_s = \pi_{sel}$: the selected pion is the soft pion from D^* decay; this happens in $\alpha_1 \approx 80 - 85\%$ of the events.
2. a π_s is detected, but $\pi_s \neq \pi_{sel}$ and $\pi_{sel} = \pi$, i.e. the selected pion is a real pion coming from background ($\alpha_2 \approx 1 - 4\%$)
3. a π_s is detected, but $\pi_s \neq \pi_{sel}$ and $\pi_{sel} \neq \pi$, i.e. is not a pion ($\alpha_3 \approx 1 - 3\%$)
4. a π_s is not detected, then $\pi_s \neq \pi_{sel}$ and $\pi_{sel} = \pi$ ($\alpha_4 \approx 2 - 10\%$)

5. a π_s is not detected, then $\pi_s \neq \pi_{sel}$ and $\pi_{sel} \neq \pi$ ($\alpha_5 \approx 1 - 5\%$)

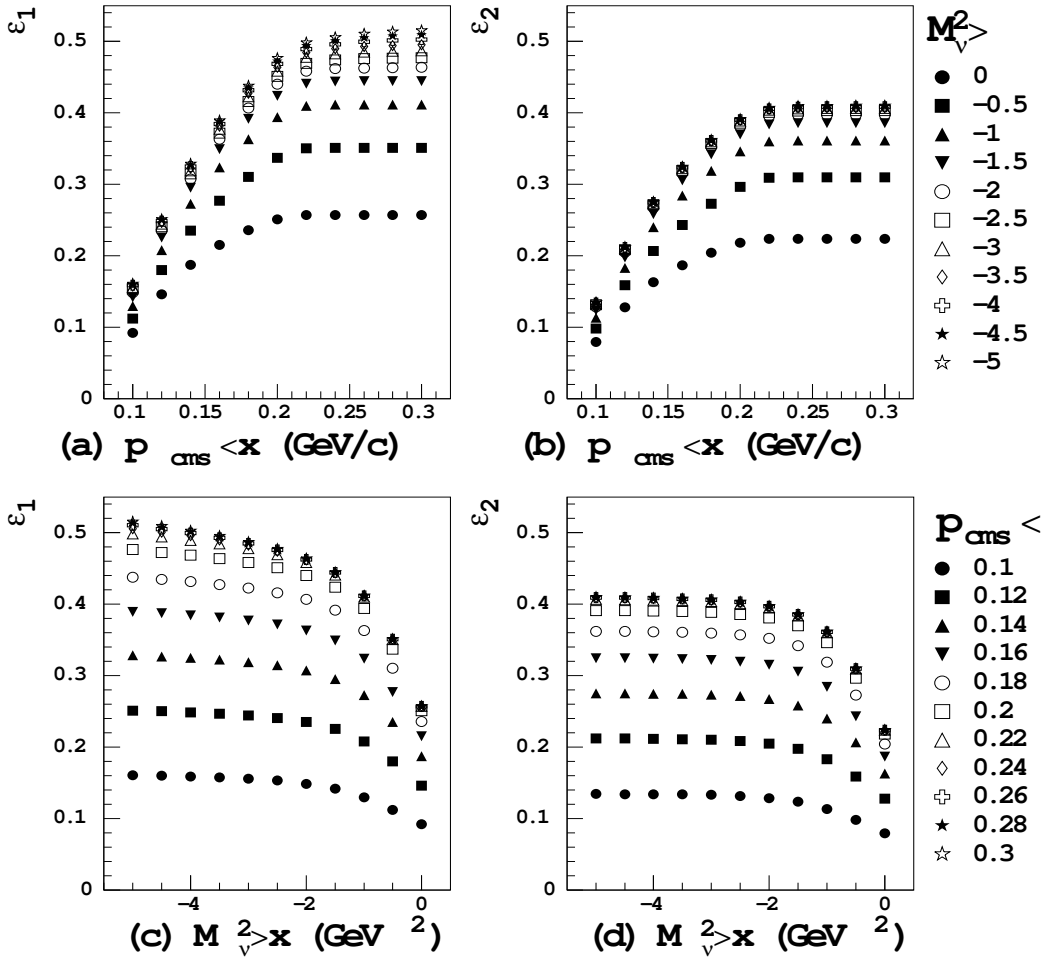

Figure 4.11: (a) and (b) Selection efficiency for Method 1.1 as a function of cut on p_{cms} for different values of cut on M_ν^2 on signal definition 1 and 2 respectively. (c) and (d) Selection efficiency for Method 1.1 as a function of cut on M_ν^2 for different values of cut on p_{cms} on signal definition 1 and 2 respectively.

The coefficients α_i indicate the ratio between the correspondent sample i and the total number of signal events, the range indicated above for each of them is due to different values of the cuts on p_{cms} and M_ν^2 . All four methods which select the best pion give about the same fractions α_i. Looking at the composition given above we can define the number of signal events in 2 different ways: $N_1^{Sig} = \sum_{i=1}^{5} N_i$, i.e. all selected signal events regardless of the correctness of the soft pion selection, and $N_2^{Sig} = N_1$, i.e. the number of signal events with the corrected selected soft pion. In the final selection we will use the first definition of the signal as we will explain later. Calculating the signal selection efficiency at different values of the cuts on p_{cms} and M_ν^2 we obtain a plateau

at about 50% and 40% for N_1^{Sig} and N_2^{Sig} definitions respectively. Fig.4.11 shows the efficiencies ϵ_1 and ϵ_2 as a function of p_{cms} and M_ν^2 for the Method 1.1. No substantial differences appear by using the other 3 methods. It can be shown that the four Methods are equivalent also concerning the background rejection with rejection factors varying from 7% to 25%, depending of cuts on p_{cms} and M_ν^2 . The ratio SB between number of selected signal events and the square root of the

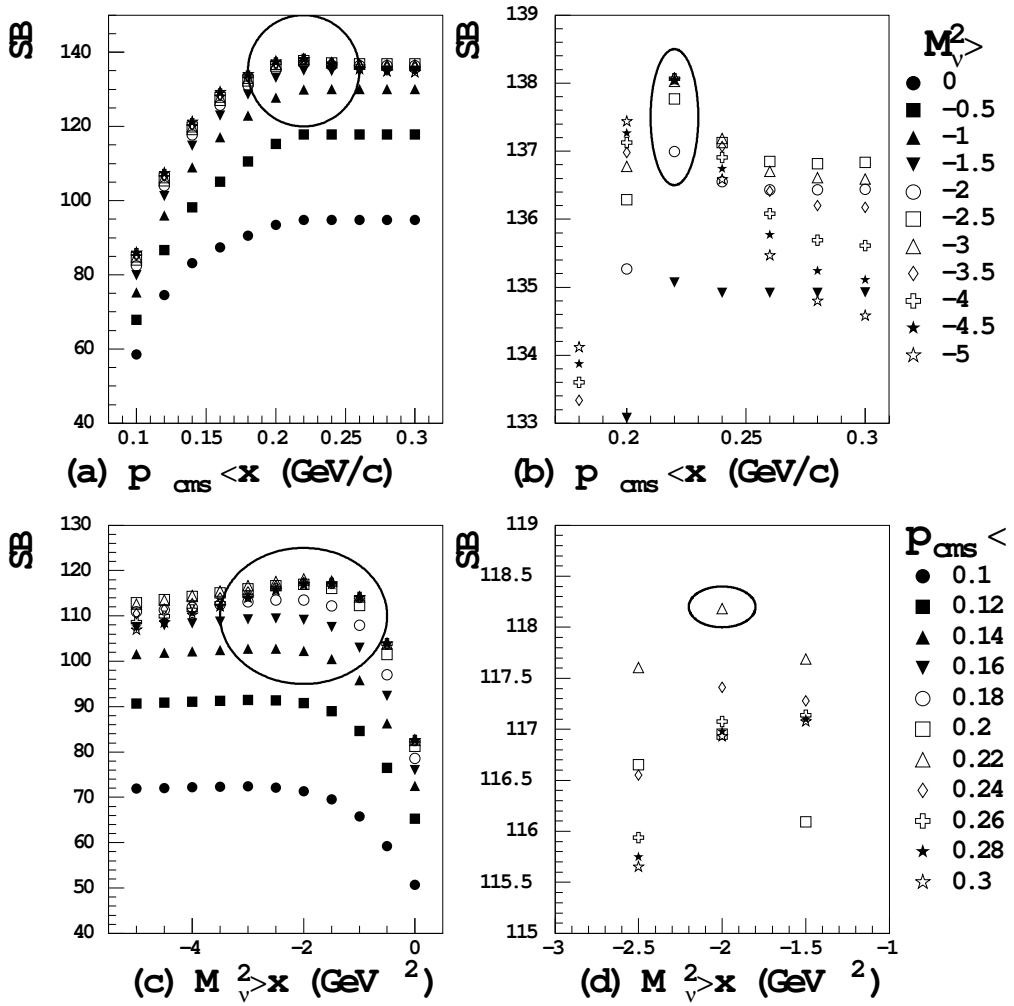

Figure 4.12: (a) Ratio SB for signal definition 1 as a function of cut on p_{cms} for different values of cut on M_ν^2 , (b) is the enlargement of interested zone of (a). (c) Ratio SB for signal definition 2 as a function of cut on M_ν^2 for different values of cut on p_{cms}, (d) is the enlargement of interested zone of (c).

sum of selected signal and background has been computed in two ways, corresponding to the two different definitions of the signal, N_1^{Sig} and N_2^{Sig}. In Fig.4.12 we plot the ratio as a function of different values of p_{cms} and M_ν^2 for the method 1.1; similar results from the other ones can be obtained. Fig.4.12(a) shows the SB ratio versus the p_{cms} cut for different values of the M_ν^2 cut. In

Fig.4.12(b) we report the same plot zoomed in the x axis in order to show that the maximum value of SB corresponds at $p_{cms} \leq 0.220$ GeV. From Fig.4.12(a) it is also possible to see that for signal definition N_1 the SB ratio as a function of cut on M_{ν}^2 reaches a plateau after $M_{\nu}^2 > -2$ GeV ^{2}. This behavior suggests to use as lower cut on M_{ν}^2 the value -2, but in order to have a confirmation of this value we can look at the SB ratio for the signal definition N_2. Fig.4.12(c) shows the SB ratio for signal N_2 as a function of cut on M_{ν}^2 for different values of cut on p_{cms}. Fig.4.12(d) shows the same plot zoomed in x axis, from which it is possible to see that the SB ratio has maximum value for $M_{\nu}^2 = -2$ GeV ^{2}. Looking at efficiency, rejection and ratio signal/background the 4 Methods to select the best pion in the event, result equally powerful, but since it is necessary to use data at low values of M_{ν}^2 in order to perform the background subtraction (see Chapter 5) we choose the Method 1.1, for which the best cuts on p_{cms} and M_{ν}^2 result to be:

$$50 \text{ MeV} \leq p_{cms} \leq 220 \text{ MeV} \tag{4.14}$$

$$M_{\nu}^2 \geq -2.0 \text{ GeV}^2 \tag{4.15}$$

Chapter 5

Determination of $\mathcal{B}\left(B^0 \to D^{*-}\ell^+\nu_\ell\right)$

In the previous chapter we have described the methods for lepton identification and for the partial $D^{*-}\ell^+\nu_\ell$ reconstruction on the recoil of a fully reconstructed B. In this chapter we will show in detail how the measurement of the branching ratio $\mathcal{B}\left(B^0 \to D^{*-}\ell^+\nu_\ell\right)$ is performed.

5.1 Formula for the determination of $\mathcal{B}\left(B^0 \to D^{*-}\ell^+\nu_\ell\right)$

In order to cancel systematic effects, we choose to determine experimentally the branching ratio $\mathcal{B}\left(B^0 \to D^{*-}\ell^+\nu_\ell\right)$ relative to the total B^0 semileptonic branching ratio. Since we are selecting the number of events $B^0 \to D^{*-}\ell^+\nu_\ell$ where $D^{*+} \to D^0\pi^+$, the branching fraction $\mathcal{B}\left(B^0 \to D^{*-}\ell^+\nu_\ell\right)$ will be calculated as:

$$\mathcal{B}\left(B^0 \to D^{*-}\ell^+\nu_\ell\right) = \frac{\mathcal{B}\left(B^0 \to Xl\nu\right)}{\mathcal{B}\left(D^{*+} \to D^0\pi^+\right)} \times \frac{N_{sel}^{D^*l\nu}}{N_{sel}^{SL,B^0}} \times \frac{1}{\epsilon^{cut}} \times \frac{\epsilon_{SL}^{Breco,SL}}{\epsilon_{sig}^{Breco,SL}} \tag{5.1}$$

The branching ratios $\mathcal{B}\left(B^0 \to Xl\nu\right) = (10.5 \pm 0.8)\%$ and $\mathcal{B}\left(D^{*+} \to D^0\pi^+\right) = (67.7 \pm 0.5)\%$ are taken from PDG [4]. $N_{sel}^{D^*l\nu}$ is the selected number of $B^0 \to D^{*-}\ell^+\nu_\ell$ events with $D^{*\pm} \to D^0\pi^\pm$ after the background subtraction and an additional Monte Carlo correction (see section 5.3). N_{sel}^{SL} is the number of selected $B^0 \to Xl\nu$ events. ϵ^{cut} is the final selection efficiency for signal respect to the semileptonic selection, while $\epsilon_{SL}^{Breco,SL}$ and $\epsilon_{sig}^{Breco,SL}$ are the product of the B_{reco} and the semileptonic selection efficiencies on B^0 semileptonic events and signal events respectively. The detailed derivation of the terms described above will be done in the following sections.

5.2 Semileptonic selection

In order to calculate the branching fraction of $B^0 \to D^{*-}\ell^+\nu_\ell$ by using the above formula 5.1, we need to determine also the total number of B^0 semileptonic decays. This is obtained requiring:

1. $P_{cms}^{\ell} > 1$ GeV.
2. $B_{charge}^{reco} = 0$.

3. correlation between B flavor and lepton charge ($B^0 - \ell^+$ or $\overline{B}^0 - \ell^-$).

The selected number of events (N_{sel}^{SL}) will be the sum of four terms: the number of real B^0 semileptonic events (N_{sel}^{SL,B^0}), the number of B^+ semileptonic events with B^+ reconstructed as B^0 ($N_{sel}^{SL,B+}$), the number of events coming from B^0 decays where the lepton is not the real daughter of the B^0 (N_{sel}^{SL,l_w}) and the number of events with a fake lepton ($N_{sel}^{SL,l_{fake}}$):

$$N_{sel}^{SL} = N_{sel}^{SL,B^0} + N_{sel}^{SL,B+} + N_{sel}^{SL,l_w} + N_{sel}^{SL,l_{fake}} \tag{5.2}$$

From Monte Carlo we can calculate the correction factor to apply to N_{sel}^{SL} in order to determine N_{sel}^{SL,B^0} as follows:

$$N_{sel}^{SL,B^0} = \frac{N_{sel}^{SL}}{K^{SL}} = \frac{N_{sel}^{SL}}{1 + K_{B^+} + K_{lw} + K_{lfake}} \tag{5.3}$$

where:

$$K_{B^+} = \frac{N_{sel}^{SL,B+}}{N_{sel}^{SL,B^0}} \quad = (3.6 \pm 0.4)\% \tag{5.4}$$

$$K_{lw} = \frac{N_{sel}^{SL,l_w}}{N_{sel}^{SL,B^0}} \quad = (0.16 \pm 0.02)\% \tag{5.5}$$

$$K_{lfake} = \frac{N_{sel}^{SL,l_{fake}}}{N_{sel}^{SL,B^0}} = (6.21 \pm 0.12)\% \tag{5.6}$$

The Factor K^{SL} is calculated from 656.7 fb^{-1} of $B^0\overline{B}^0$ and 668.2 fb^{-1} of B^+B^- Monte Carlo events and results to be:

$$K^{SL} = 1.100 \pm 0.004(stat_{mc}) \tag{5.7}$$

The number of calculated B^0 semileptonic events is comparable within the errors with the true number from Monte Carlo:

$$N_{sel,MC}^{SL,B^0} = 96079 \pm 528(stat_{mc}) \tag{5.8}$$

$$N_{true}^{SL,B^0} = 94666 \pm 397(stat_{mc}) \tag{5.9}$$

$$\tag{5.10}$$

When applying this method on 210.5 fb^{-1} of real data we obtain:

$$N_{sel}^{SL,B^0} = 21504 \pm 202(stat_{dat}) \pm 80(stat_{mc}) \tag{5.11}$$

5.3 Signal extraction and background subtraction

Signal events are extracted applying the following requests:

1. $B_{charge}^{reco} = 0$.

2. Correlation between B flavor and charge of lepton ($B^0 - \ell^+$ or $\overline{B}^0 - \ell^-$).

3. $P^{\ell}_{cms} > 1$ GeV.
4. Correct charge correlation between lepton and soft pion ($\ell^+ - \pi^-$ or $\ell^- - \pi^+$).
5. If more than one pion is found, choose the one with minimum p^{π}_{cms}.
6. 50 MeV $\leq p^{\pi}_{cms} \leq 220$ MeV.
7. $M^2_{\nu} \geq -2.0$ GeV^2.

The cuts 1, 2 and 3 are the same as in the semileptonic selection, while the others are specific for signal selection. As seen in the previous chapter the selection is not able to reject all background events, then a background subtraction has to be developed. For this purpose the requests 4 and 7 can be used by reversing them, that means wrong charge correlation between lepton and soft pion and $M^2_{\nu} < -5.0$ GeV^2. The idea is that the background at $M^2_{\nu} > -2.0$ GeV^2 can be described from wrong sign combinations, whose relative normalization to right sign events can be determined in a region where there is no signal, namely at $M^2_{\nu} < -5.0$ GeV^2. In the following sections we will use the notation: $N^{\alpha,\beta}_{sel}$, where $\alpha = RS$ or WS for right or wrong charge correlation respectively, while $\beta = 2$ or 5 for $M^2_{\nu} \geq -2.0$ GeV^2 or $M^2_{\nu} < -5.0$ GeV^2 respectively. We will see that the background subtraction procedure involves also a small portion of signal events, then we have to perform a correction for signal events in addition to background subtraction.

The number of corrected signal events ($N^{D^* l\nu}_{sel}$) is calculated with the following relation:

$$N^{D^* l\nu}_{sel} = \frac{1}{K_{MC}} \times \left(N^{RS,2}_{sel} - NF^5 \times N^{WS,2}_{sel} - MC_{corr} \right) \tag{5.12}$$

see App.A(eq.A.9) for the derivation of this formula. $N^{RS,2}_{sel}$ and $N^{WS,2}_{sel}$ are the selected number of events with right and wrong sign at $M^2_{\nu} \geq -2.0$ GeV^2, respectively. NF^5 is the ratio between the selected number of events with right and wrong sign at $M^2_{\nu} < -5.0$ GeV^2. MC_{corr} and K_{MC} are Monte Carlo corrections which take into account possible discrepancies between RS/WS samples, and the small fraction of signal events subtracted by the subtraction procedure, respectively. In order to understand how to subtract the background we have to study the composition of the selected events, discussed in the next sections.

5.3.1 Sample composition

The selected events are composed by signal and background events which satisfy the selection cuts, signal events in which the selected pion is not the real soft pion and signal events in which the D^{*+} decays into $D^+\pi^0$ with a background pion reconstructed as soft pion. The background

events will be of different kinds, therefore different methods have to be involved for the subtraction. In summary, the selected samples of events are:

1. $D^{*-}\ell^+\nu_\ell$ events with $D^{*+} \to D^0\pi^+$ and $\pi_{sel} = \pi_s$
2. $D^{*-}\ell^+\nu_\ell$ events with $D^{*+} \to D^0\pi^+$ and $\pi_{sel} = \pi_{wrong}$
3. $D^{*-}\ell^+\nu_\ell$ with $D^{*+} \to D^+\pi^0$ with a charged pion reconstructed as soft pion
4. Physical background: all semileptonic and non-semileptonic B events
5. Continuum background ($c\overline{c}$ and uds)
6. Combinatorial background in B decays

The selected events will be the sum of these six samples, but the signal that we have to extract is the sample 1 ($N^{RS,2}_{sig(\pi_s)}$) or alternatively the sum of samples 1 and 2 ($N^{RS,2}_{sig}$). Sample 3 will be taken into account by Monte Carlo simulation. The continuum and combinatorial backgrounds are subtracted with a fit in $m_{\rm ES}$, before the physical background subtraction. Other Monte Carlo corrections will also be introduced.

5.3.2 Continuum and combinatorial backgrounds subtraction

The continuum and combinatorial backgrounds are subtracted by a fit on $m_{\rm ES}$ [42]. The $m_{\rm ES}$ distribution, in the range $5.2 \div 5.3$ GeV, is fitted with a Crystal-Ball function for the signal and an Argus function for the background (see App.B for the definition of Crystal-Ball and Argus functions). The contribution of continuum and combinatorial backgrounds under the $m_{\rm ES}$ peak is the area of the fitted Argus function above 5.27 GeV, the area of the Crystal-Ball gives the number of signal events (see App.B for more details). In Fig.5.1(a), (b) and (c) we plot respectively the $m_{\rm ES}$ fit for all generic Monte Carlo events, signal events and physical background events, after applying signal selection. From Fig.5.1 it is possible to see that the region below 5.27 GeV is more populated in background events than in signal events, but a non negligible fraction of physical background events have also an $m_{\rm ES}$ distribution similar to the signal above 5.27 GeV. This is the reason why a method for physical background subtraction has to be performed after the $m_{\rm ES}$ fit as we will describe in next subsection.

5.3.3 Physical background subtraction

The physical background is composed by non-semileptonic B decays and by semileptonic B decays different from the signal. Tab.5.1 shows a list of the Monte Carlo simulated samples. The contamination from physical background is estimated by normalizing the selected WS events at $M^2_\nu > -2$ with the ratio between RS and WS selected events at $M^2_\nu < -5$, assuming that for background events the ratio RS/WS would be the same for $M^2_\nu > -2$ and for $M^2_\nu < -5$. This

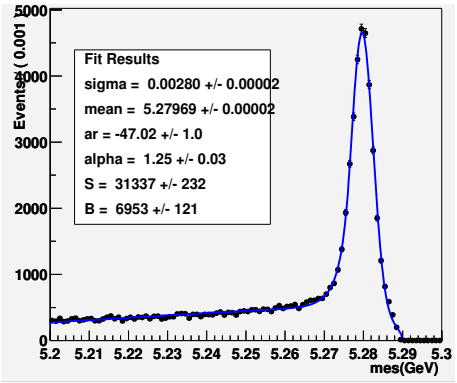

(a)

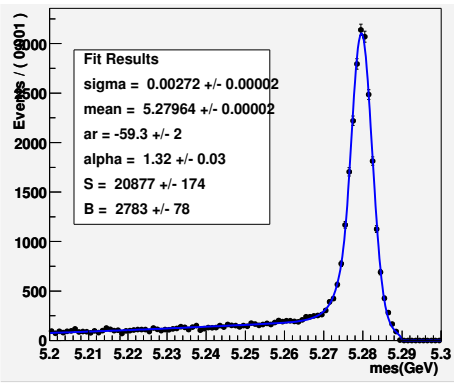

(b)

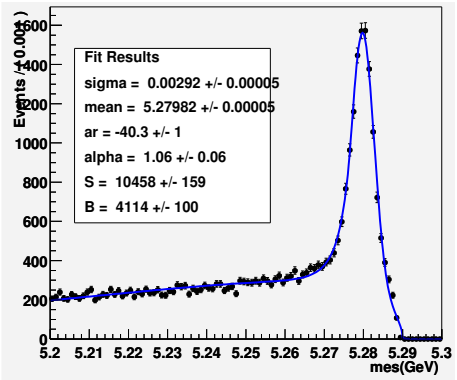

(c)

Figure 5.1: $m_{\rm ES}$ fit on generic Monte Carlo. (a) All events, (b) signal events, (c) physical background events.

assumption is not true for all backgrounds, then corrections have to be applied in order to take into account this deviation. As described in detail in App.A the number of calculated background events at $M_\nu^2 > -2$ can be obtained as:

$$N_{bkg,calc}^{RS,2} = NF^5 \times N_{sel}^{WS,2} + MC_{corr} \tag{5.13}$$

where $NF^5 = N_{sel}^{RS,5}/N_{sel}^{WS,5}$ and $MC_{corr} = \sum_{i,i\neq sig}(NF_i^2 - NF^5)N_i^{WS,2}$, with $NF_i^2 = N_i^{RS,2}/N_i^{WS,2}$, if we use Monte Carlo. On real data MC_{corr} is expressed by eq.5.14. A total of 14 background samples are generated in generic Monte Carlo and they will be numbered as indicated in Tab.5.1. Concerning this subtraction applied on real data the sum over Monte Carlo samples needs to be rescaled taking into account the relative luminosities of simulation and data. In practice, the sum over the first seven samples will be rescaled with the ratio $\mathcal{L}_{data}/\mathcal{L}_{MC}^{B^0}$ and the sum over the last seven samples will be rescaled with the ratio $\mathcal{L}_{data}/\mathcal{L}_{MC}^{B^+}$ as indicated in the following equation:

$$MC_{corr}^{dat} = \frac{\mathcal{L}_{data}}{\mathcal{L}_{MC}^{B^0}} \sum_{i=1}^{7}(NF_i^2 - NF^5)N_i^{WS,2} + \frac{\mathcal{L}_{data}}{\mathcal{L}_{MC}^{B^+}} \sum_{i=8}^{14}(NF_i^2 - NF^5)N_i^{WS,2} \tag{5.14}$$

Type of decay	Index for decays from B^0	Index for decays from B^+
Non-SL	1	8
Other SL	2	9
$D^0, D^+ l\nu$	3	10
$D^{*0} l\nu$	4	11
$D_2^* l\nu$	5	12
$D_1 l\nu$	6	13
other $Dl\nu$	7	14

Table 5.1: Numbering scheme of background samples studied from generic Monte Carlo. SL means semileptonic.

In order to evaluate this method for background calculation it is interesting to compare each single NF_i^2 with the overall normalization factor NF^5 (both for MC and data) as plotted in the upper plot of Fig.5.2(a). This evaluation cannot give us all information concerning the correction,

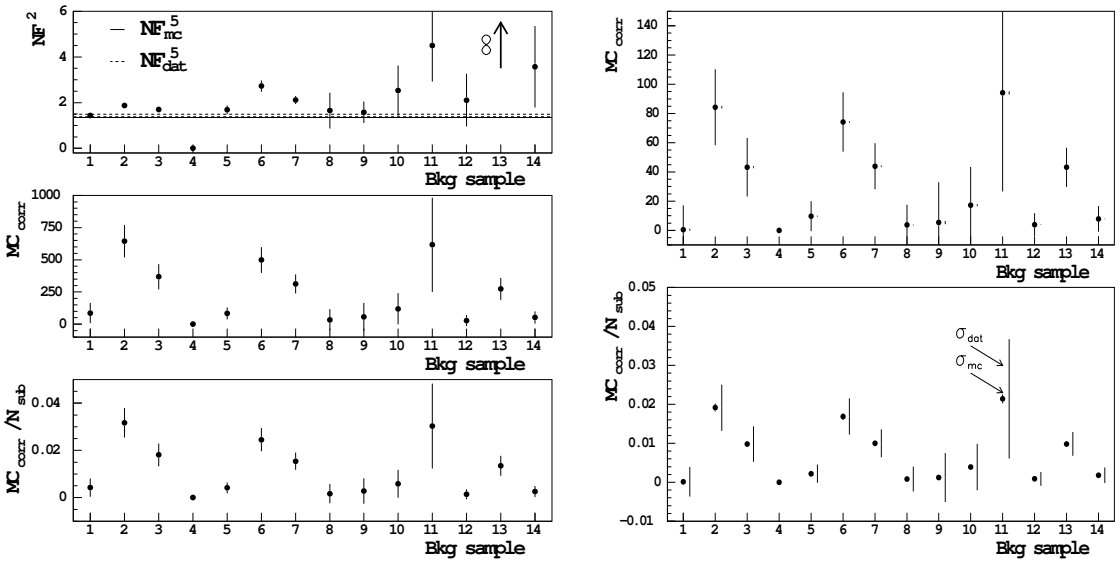

(a) (b)

Figure 5.2: (a) Study of MC_{corr} calculated on Monte Carlo. Top plot: relative normalization at $M_\nu^2 > -2$, NF_i^2 of each background samples. Middle plot: number of events to be corrected (MC_i) for each background samples. Bottom plot: $MC_i/(N_{sel}^{RS,2} - NF^5 \times N_{sel}^{WS,2})$ of each background samples. (b) Study of MC_{corr}^{dat} applied on data. Top plot: MC_i of each background samples. Bottom plot: $MC_i/(N_{sel}^{RS,2} - NF_{data}^5 \times N_{sel}^{WS,2})$ of each background samples. The indicated σ_{mc} and σ_{data} errors are Monte Carlo and data statistical errors respectively.

in fact it is possible to have an NF_i^2 very different from NF^5, but if the number $N_i^{WS,2}$ is very low, the contribution of this term could be negligible for the final calculation. For this reason it is more important to look at the contribution of each term $MC_i = (NF_i^2 - NF^5)N_i^{WS,2}$ to the final calculation as shown in the middle plot of Fig.5.2(a). From these two plots it is possible

to see for instance, that NF^2_{13} tends to be very high, then the contribution of the MC correction from sample 13 will be just the number of events $N^{RS,2}_{13}$, in fact for an $NF^2_i >> NF^5$ the factor $NF^2_i - NF^5 \approx NF^2_i$, then the corresponding $MC^i_{corr} \approx N^{RS,2}_i$. In the lower plot of Fig.5.2(a) we show the ratio $MC_i/(N^{RS,2}_{sel} - NF^5 \times N^{WS,2}_{sel})$, in order to evaluate each single contribution of the MC correction in the final calculation. This plot gives us the information concerning the weight of each background samples. In the upper plot of Fig.5.2(b) we show the MC_i calculated with data, while in the lower plot we show the ratio $MC_i/(N^{RS,2}_{sel} - NF^5 \times N^{WS,2}_{sel})$ calculated with data. As explained in App.A in the data calculation we use the value of NF^5_{data} calculated with data. Each

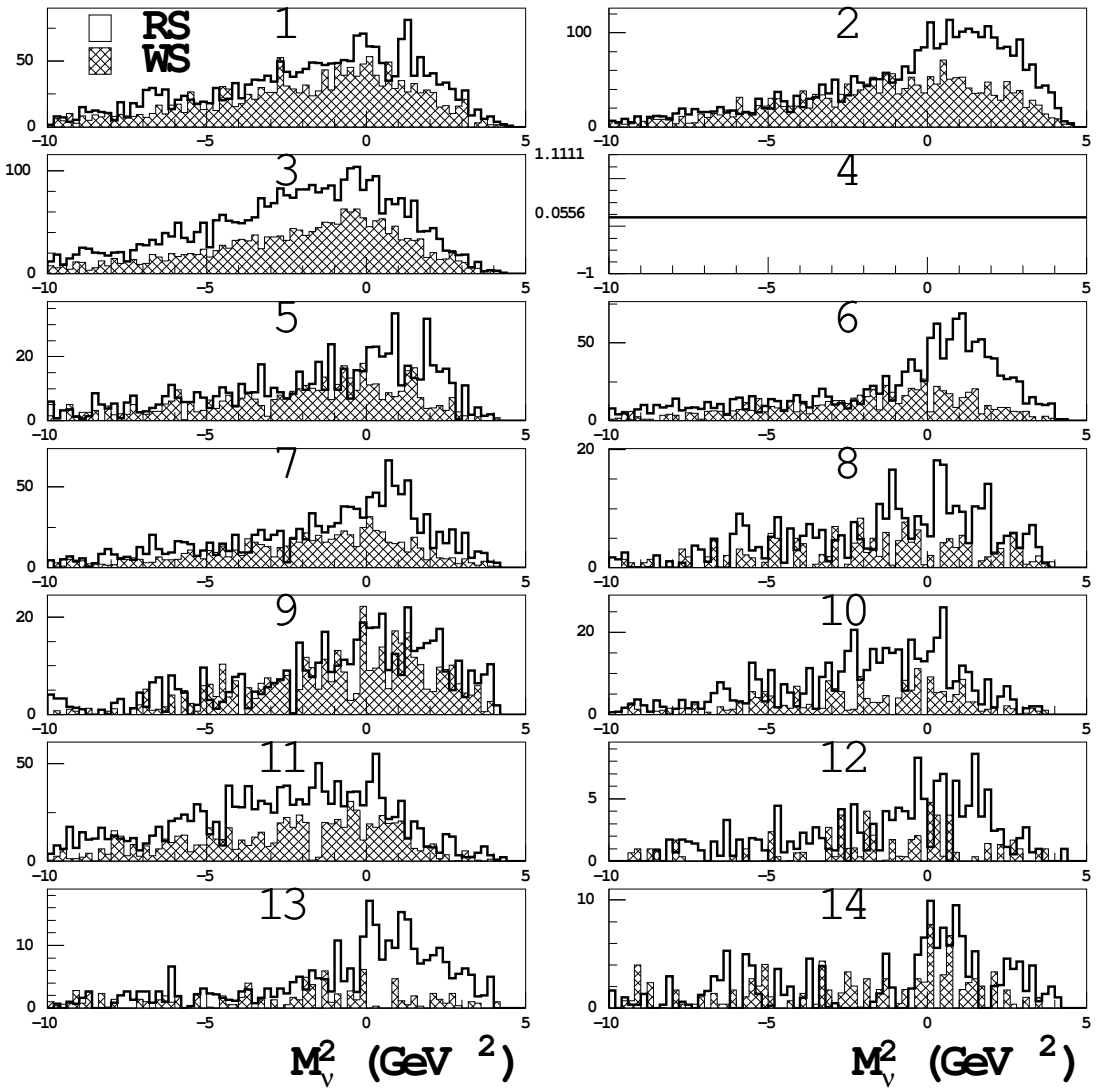

Figure 5.3: M^2_ν distributions of the 14 background samples from Monte Carlo. Each plot shows M^2_ν distribution from RS selection (white area) and from WS selection (cross-hatched area).

single sample gives a contribution that varies between 0% and 4% on Monte Carlo and between 0% and 3% on data. The values of the factor NF^5 and of the total MC_{corr} for Monte Carlo and data are:

$$NF^5_{mc} = \quad 1.33 \pm 0.04 \tag{5.15}$$

$$NF^5_{dat} = \quad 1.43 \pm 0.11 \tag{5.16}$$

$$MC^{mc}_{corr} = \quad 3176 \pm 478 \tag{5.17}$$

$$MC^{dat}_{corr} = \quad 431 \pm 46(stat_{dat}) \pm 93(stat_{mc}) \tag{5.18}$$

The differences between the global factor NF^5 and the single NF^2_i can be explained looking at the differences in the M^2_ν distribution for RS and WS for the total of background events and for each sample. In Fig.5.3 we plot the M^2_ν distributions for the 14 background samples, each plot shows the distribution of RS (white area) and WS selections (cross-hatched are). Comparing the plots in Fig.5.3 and the middle plot of Fig.5.2(a) it possible to understand that a background sample with similar M^2_ν distributions (for $M^2_\nu > -2$) for RS and WS selections gives a low MC_{corr} contribution, while the MC_{corr} contribution is high for background samples with different M^2_ν distributions for RS and WS selections. In order to give a low contribution to MC_{corr}, it is clearly not enough to have similar distributions for RS and WS selections, but the ratio between RS and WS at $M^2_\nu > -2$ has also to be near to the NF^5 factor. For example sample 1 has similar M^2_ν RS and WS distributions and the corresponding MC_{corr} is low compared with the one coming from sample 2. Contributions to the RS and WS for Monte Carlo correction coming from samples with few events are not easy to compute from the corresponding M^2_ν distributions, and the associated

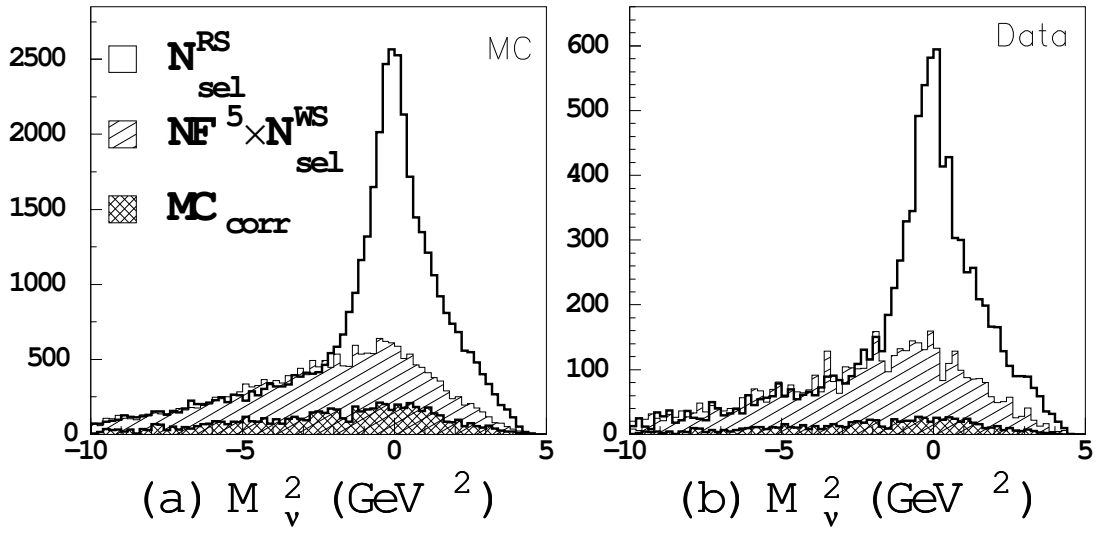

Figure 5.4: M^2_ν distribution of N^{RS}_{sel} (white area), $NF^5 \times N^{WS}_{sel}$ (shaded area) and MC_{corr} (cross-hatched are). (a) on Monte Carlo and (b) on data.

errors become very high (see sample 11 for example). The values of $N_{sel}^{RS,2} - NF^5 \times N_{sel}^{WS,2}$ are 20374 and 4400 respectively in Monte Carlo and data, then the MC_{corr} gives 16% and 14% corrections for MC and data, respectively.

The physical background subtraction developed here, applied on Monte Carlo for $M_\nu^2 > -2$ is shown in Fig.5.4(a) where we plot the M_ν^2 distribution respectively for N_{sel}^{RS} (white area), $NF^5 \times N_{sel}^{WS}$ (shaded area) and MC_{corr} (cross-hatched area). In Fig.5.4(b) we plot the same distributions obtained from data. These M_ν^2 distributions are obtained requiring $m_{\rm ES} > 5.27$ and subtracting the M_ν^2 distribution of the continuum and combinatorial backgrounds below the $m_{\rm ES}$ peak [1].

5.3.4 Monte Carlo correction on signal events

As described above some Monte Carlo corrections have to be taken into account for the final calculation of the number of $D^{*-}\ell^+\nu_\ell$ events. The background subtraction described in the previous section will subtract also the two following samples of events:

1. a fraction of signal events = $NF^5 \times N_{sig}^{WS,2}$
2. a fraction of signal events with $D^{*+} \to D^+\pi^0$ = $NF^5 \times N_{sig(D^+)}^{WS,2}$

this two fractions cannot be corrected in the background subtraction procedure, because when going from Monte Carlo to Data a rescaling with luminosity has to be performed. Since this two samples are related to the branching ratio that we want to measure, they cannot be treated as the other samples. This correction will be evaluated from Monte Carlo. A correction factor K_{MC} has to be inserted into the final calculation (see App.A):

$$K_{MC} = \left(1 - NF^5 \times \left(K_{sig}^{WS/RS,2} + K_{sig(D^-)}^{WS/RS,2}\right) + K_{sig(D^-)}^{RS/RS,2}\right) \tag{5.19}$$

where the factors K are computer from Monte Carlo defined as:

$$K_{sig}^{WS/RS,2} = \frac{N_{sig}^{WS,2}}{N_{sig}^{RS,2}} = 0.123 \pm 0.003 \tag{5.20}$$

$$K_{D^-/sig}^{WS/RS,2} = \frac{N_{D^-}^{WS,2}}{N_{sig}^{RS,2}} = 0.051 \pm 0.002 \tag{5.21}$$

$$K_{D^-/sig}^{RS/RS,2} = \frac{N_{D^-}^{RS,2}}{N_{sig}^{RS,2}} = 0.084 \pm 0.003 \tag{5.22}$$

[1] The M_ν^2 distribution for continuum and combinatorial backgrounds events below the $m_{\rm ES}$ peak fitted with $m_{\rm ES}$ fit is obtained rescaling with this number the M_ν^2 distribution for those events at $m_{\rm ES} < 5.25$. Since we can access the M_ν^2 shape of these background events only at low values on $m_{\rm ES}$, this procedure implies that the shape of M_ν^2 distribution for continuum and combinatorial background events is the same for different region of $m_{\rm ES}$.

where sig means $B^0 \to D^{*-}\ell^+\nu_\ell$ events with $D^{*\pm} \to D^0\pi^\pm$, while "D^-" means $B^0 \to D^{*-}\ell^+\nu_\ell$ events with $D^{*-} \to D^-\pi^0$. The values of K_{MC} for Monte Carlo and data are:

$$K_{MC}^{MC} = 0.852 \pm 0.009(stat_{mc}) \tag{5.23}$$

$$K_{MC}^{dat} = 0.835 \pm 0.019(stat_{data}) \pm 0.006(stat_{mc}) \tag{5.24}$$

The differences between K_{MC}^{MC} and K_{MC}^{dat} is due entirely to the different normalization factors NF_{MC}^5 and NF_{dat}^5 (see App.A).
If instead of using all signal events which survive the cuts, we want to extract the number of signal events with the soft pion correctly identified, the correction factor will be:

$$K_{sig,\pi_s}^{MC} = \left(1 + K_{sig}^{\pi_w/\pi_s,RS,2}\right) \times K_{sig}^{MC} \tag{5.25}$$

where $K_{sig}^{\pi_w/\pi_s,RS,2}$ is defined in eq.A.16 in App.A.
Using the first definition we find the following values for the number of selected signal events on Monte Carlo and on data:

$$N_{sel,MC}^{RS,2} = 20136 \pm 809(stat_{mc}) \quad \left(N_{True,MC}^{RS,2} = 20877 \pm 174(stat_{mc})\right) \tag{5.26}$$

$$N_{sel,data}^{RS,2} = 4748 \pm 301(stat_{dat}) \pm 117(stat_{mc}) \tag{5.27}$$

while using the second definition the $N_{sel(\,\mathrm{ps}_s),data}^{RS,2}$ is:

$$N_{sel(\pi_s),data}^{RS,2} = 4118 \pm 241(stat_{dat}) \pm 135(stat_{mc}) \tag{5.28}$$

With the corresponding selection efficiencies for $N_{sel}^{RS,2}$ and $N_{sel(\pi_s)}^{RS,2}$ from eq.5.30 and eq.5.31 respectively, it easy to see that the ratios $N_{sig}^{RS,2}/\epsilon^{cut}$ and $N_{sig(\pi_s)}^{RS,2}/\epsilon^{cut,\pi_s}$ are similar, in fact the ratio between them is 1. Moreover the error from Monte Carlo with the second correction is 3.3%, whereas without this correction the error decreases at 2.5%. Then in the final calculation the first definition of signal events (eq.5.27) will be used,

$$N_{sel}^{D^*l\nu} = N_{sel,data}^{RS,2} \tag{5.29}$$

5.4 Efficiency calculations

The signal efficiencies for the final and semileptonic selections are calculated from Monte Carlo. For the final calculation we need to determine three efficiencies:

- ϵ^{cut} (ϵ^{cut,π_s}) which is the efficiency of the final signal (signal with correctly identified π_s) selection relative to the semileptonic selection.
- $\epsilon_{sig}^{Breco,SL}$ which is the efficiency of the B reconstruction and semileptonic selection on signal events.

- $\epsilon_{SL}^{Breco,SL}$ which is the efficiency of the B reconstruction and semileptonic selection on B^0 semileptonic events.

Concerning the efficiencies of the final selection we have two cases: the first one when we select signal events without requiring that the soft pion in signal event is the correct one (ϵ^{cut}) and the second case when we correct for that (ϵ^{cut,π_s}). The efficiencies $\epsilon_{sig}^{Breco,SL}$ and $\epsilon_{SL}^{Breco,SL}$ should be very similar, because our signal is a significant fraction ($\sim 50\%$) of all semileptonic decays.

5.4.1 Signal selection efficiency

The signal selection efficiency is the ratio between the number of signal events with the final and semileptonic selection, as determined from $m_{\rm ES}$ fits:

$$\epsilon^{cut} = \frac{N_{sig}^{RS,2}}{N_{sig}^{Breco,SL}} = \frac{20877 \pm 174}{36529 \pm 236} = 0.572 \pm 0.006(stat_{mc}) \tag{5.30}$$

$$\epsilon^{cut,\pi_s} = \frac{N_{sig(\pi_s)}^{RS,2}}{N_{sig}^{Breco,SL}} = \frac{18122 \pm 149}{36529 \pm 236} = 0.496 \pm 0.005(stat_{mc}) \tag{5.31}$$

In the final calculation the first one will be used, but the second one has also been used to check the consistency of the two results (see section 5.3.4).

5.4.2 Semileptonic selection efficiency

The B reconstruction and semileptonic selection efficiency on signal is the ratio between the number of signal events that survive the B reconstruction and the semileptonic selection, and the number of total generated signal events, which is the product of the total number of generated $B^0\overline{B}^0$ pairs, the semileptonic branching ratio and the $D^{*+} \to D^0\pi^+$ branching ratio used in Monte Carlo:

$$\begin{aligned}\epsilon_{sig}^{Breco,SL} &= \frac{N_{sig}^{Breco,SL}}{N_{B^0\overline{B}^0}^{gen} \times \mathcal{B}\left(B^0 \to D^{*-}\ell^+\nu_\ell\right) \times \mathcal{B}(D^{*+} \to D^0\pi^+)} \\ &= \frac{36529 \pm 236}{3.6 \times 10^8 \times 0.056 \times 0.677} = (2.668 \pm 0.017(stat_{mc})) \times 10^{-3}\end{aligned} \tag{5.32}$$

The efficiency of B reconstruction and semileptonic selection on B^0 semileptonic events is the ratio between semileptonic events that survive the B reconstruction and the semileptonic selection and the total generated number of B^0 semileptonic events, which is the product of the total number of generated $B^0\overline{B}^0$ pairs and the semileptonic branching ratio used in Monte Carlo:

$$\begin{aligned}\epsilon_{SL}^{Breco,SL} &= \frac{N_{SL}^{Breco,SL}}{N_{B^0\overline{B}^0}^{gen} \times \mathcal{B}(B \to Xl\nu)} \\ &= \frac{94666 \pm 397}{3.6 \times 10^8 \times 0.1061} = (2.470 \pm 0.010(stat_{mc})) \times 10^{-3}\end{aligned} \tag{5.33}$$

As said before these two efficiencies are similar and the ratio $\epsilon_{sig}^{Breco,SL}/\epsilon_{SL}^{Breco,SL}$ is $1.08 \pm 0.001(stat_{mc})$.

5.5 Systematic uncertainties

The systematic uncertainties for this partial reconstruction analysis are due to:

- σ_1: Uncertainties on used branching ratios: $\mathcal{B}\left(B^0 \to Xl\nu\right)$ and $\mathcal{B}\left(D^{*+} \to D^0\pi^+\right)$.
- σ_2: limited Monte Carlo statistics.
- uncertainties coming from MC_{corr}:
  - σ_{3a}: limited knowledge of semileptonic B decays in higher D states $\mathcal{B}\left(B \to D_2^* l\nu\right)$, $\mathcal{B}\left(B \to D_1 l\nu\right)$ and $\mathcal{B}\left(\text{other}B \to D^{**} l\nu\right)$.
  - σ_{3b}: limited knowledge of other B decays $\mathcal{B}\left(B \to \text{other}\right)$.
- σ_4: effects on $\epsilon_{sig}^{Breco,SL}/\epsilon_{SL}^{Breco,SL}$ due to the fully reconstructed B.
- σ_5: lepton tracking.
- σ_6: lepton identification.
- σ_7: lepton misidentification.
- σ_8: soft π_s detection.
- σ_9: $m_{\rm ES}$ fit.

5.5.1 $\mathcal{B}\left(B^0 \to Xl\nu\right)$ and $\mathcal{B}\left(D^{*+} \to D^0\pi^+\right)$ (σ_1)

The branching ratios $\mathcal{B}\left(B^0 \to Xl\nu\right)$ and $\mathcal{B}\left(D^{*+} \to D^0\pi^+\right)$ taken from PDG [4] with their errors give the following contribution to systematic errors on final value of branching ratio:

$$\sigma_1 = 0.42 \times 10^{-2} \ \ (7.7\% \text{ on } \mathcal{B}) \tag{5.34}$$

where the contribution due to the former process dominates.

5.5.2 Monte Carlo statistics (σ_2)

All factors calculated from Monte Carlo used in the final calculations are affected by statistical errors coming from the limited number of Monte Carlo events, then we treat these uncertainties as systematic error,

$$\sigma_2 = 0.16 \times 10^{-2} \ \ (2.8\% \text{ on } \mathcal{B}) \tag{5.35}$$

5.5.3 MC_{corr} (σ_{3a} and σ_{3b})

The limited knowledge of the branching ratios $\mathcal{B}(B \to D_2^* l\nu)$, $\mathcal{B}(B \to D_1 l\nu)$, $\mathcal{B}(\text{other}B \to D^{**} l\nu)$ and $\mathcal{B}(B \to \text{hadrons})$ is a source of systematics uncertainty, because the simulated fractions of these events satisfying the final selection are used in MC_{corr}. Since in Monte Carlo these events are generated with given branching ratios we have to take into account that these values are not known with high precision, then we have to look at the variation on branching ratio due to possible variations on these fractions. For this purpose we distinguish the hadronic modes from the semileptonic ones.

The semileptonic decays in higher D resonances are generated in Monte Carlo with the following branching ratios:

$$\mathcal{B}(B \to D_2^* l\nu) = 0.0037 \tag{5.36}$$

$$\mathcal{B}(B \to D_1 l\nu) = 0.0056 \tag{5.37}$$

$$\mathcal{B}(\text{other}B \to D^{**} l\nu) = 0.0177 \tag{5.38}$$

The sum of these three branching ratios $\mathcal{B}(B \to D^{**} l\nu) = 0.027$ is better known, since it is by definition $\mathcal{B}(B \to X l\nu) - \mathcal{B}(B \to D l\nu) - \mathcal{B}(B \to D^* l\nu)$, but the single $\mathcal{B}$ listed above are not known. Therefore we evaluate the effect on the final branching ratio by varying each single fraction of corresponding events while keeping constant the sum of the three $\mathcal{B}$s. This variation has been done on the number of events that appear in MC_{corr} allowing a variation of each single $\mathcal{B}$ in the range between 0 and $\mathcal{B}_{tot}$. In detail, we associate two random values of $\mathcal{B}$ at two channels with the constraints $\mathcal{B}_1 + \mathcal{B}_2 \leq \mathcal{B}_{tot}$ then we calculate the third as the difference $\mathcal{B}_3 = \mathcal{B}_{tot} - (\mathcal{B}_1 + \mathcal{B}_2)$, and we iterate on all possible combinations. The systematic error is taken as the RMS of the obtained distribution of results, shown in Fig.5.5(a). This distribution is asymmetric with a tail at lower $\mathcal{B}$, because this method allows each single $\mathcal{B}$ to vary from 0 to $\mathcal{B}_{tot}$ [2].

We take the RMS of the distribution as systematic error:

$$\sigma_{3a} = 0.18 \times 10^{-2} \ \ (3.3\% \text{ on } \mathcal{B}) \tag{5.39}$$

The uncertainty due to the B decays in hadronic final states was determined by the same method used before, where we allowed a 100% variation on the number of selected hadronic events in Monte Carlo. The distribution of branching ratios obtained with this variation results to be flat, as shown in Fig.5.5(b), in the range between 0.05542 and 0.05554 with an RMS of $0.33 \times$

[2] An associated $\mathcal{B} = 0$ corresponds to a decreasing variation of 100% on both $\mathcal{B}$, while an associated $\mathcal{B} = \mathcal{B}_{tot}$ corresponds to an increasing variation of 630%, 382% and 53% for $\mathcal{B}(B \to D_2^* l\nu)$, $\mathcal{B}(B \to D_1 l\nu)$ and $\mathcal{B}(\text{other}B \to D^{**} l\nu)$ respectively. For the first two branching ratios, the increasing variation is larger then the decreasing variation. This asymmetry causes an increase of the contribution in relative MC_{corr}, then the number of signal events decreases, reducing the calculated branching ratio.

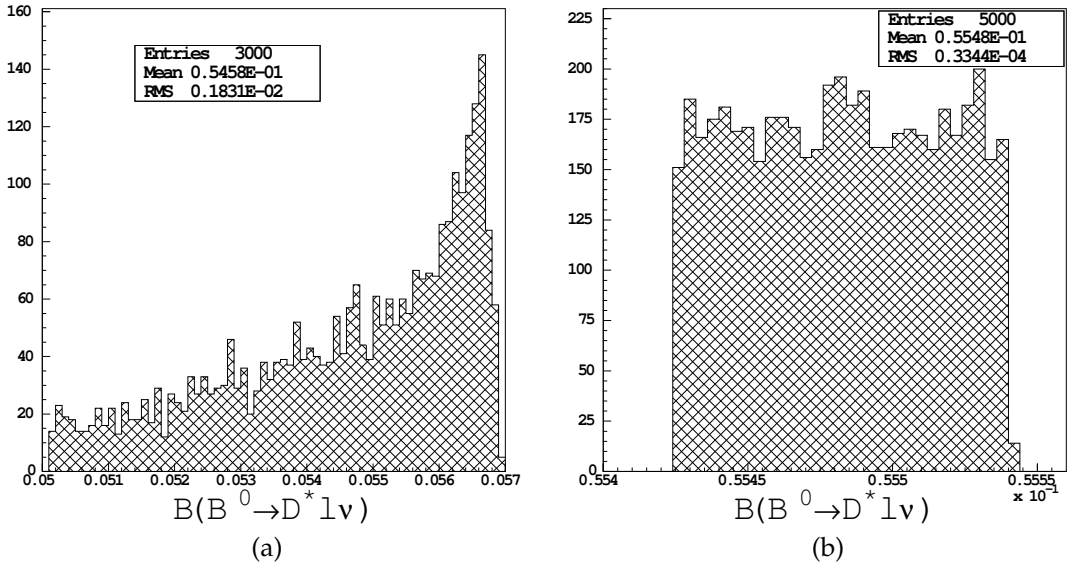

(a) (b)

Figure 5.5: Distribution of the $\mathcal{B}\left(B^0 \to D^{*-}\ell^+\nu_\ell\right)$ obtained from the variation of $\mathcal{B}\left(B \to D_2^* l\nu\right)$, $\mathcal{B}\left(B \to D_1 l\nu\right)$ and $\mathcal{B}\left(\text{other}B \to D^{**} l\nu\right)$ in (a), and from the variation of $\mathcal{B}\left(B \to \text{non-SL}\right)$ in (b).

10^{-4}, then the associated systematic error is:

$$\sigma_{3b} = 0.33 \times 10^{-4} \ \ (0.06\% \text{ on } \mathcal{B}) \tag{5.40}$$

which gives a negligible contribution to the final systematic uncertainty. This is due to a very low contamination from hadronic B decays in our final sample.

5.5.4 Effect on efficiency ratio due to the fully reconstructed B (σ_4)

The systematic on the efficiency ratio $\epsilon_{sig}^{Breco,SL}/\epsilon_{SL}^{Breco,SL}$ due to the fully reconstructed B is taken from previous studies [44] in which the same reconstruction technique is used. The associated systematic error on the efficiency of B reconstruction is 3% [44], then the final systematic uncertainty on branching ratio is:

$$\sigma_4 = 0.17 \times 10^{-2} \ \ (3\% \text{ on } \mathcal{B}) \tag{5.41}$$

5.5.5 Lepton tracking (σ_5)

A systematic uncertainty of 1.3% [43] associated to the tracking of the lepton has to be applied at all terms containing a lepton in the $\mathcal{B}$ formula. The right technique to estimate this uncertainty consists in the random killing of lepton tracks with a probability of 1.3%. We allow a random variation on the number of selected semileptonic events within 1.3%. The final systematic on $\mathcal{B}$ from lepton tracking is the RMS of the $\mathcal{B}$ distribution obtained from this method and plotted in

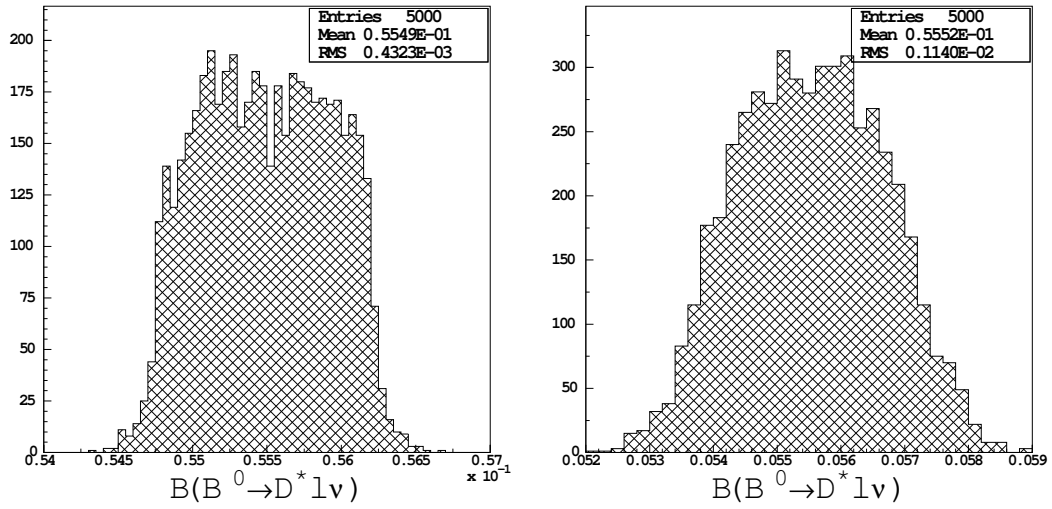

(a) (b)

Figure 5.6: Distribution of $\mathcal{B}\left(B^0 \to D^{*-}\ell^+\nu_\ell\right)$ obtained with random killing of lepton tracks (a), and with random failing of lepton ID (b).

Fig.5.6(a):

$$\sigma_5 = 0.43 \times 10^{-3} \ \text{(0.8\% on } \mathcal{B}) \tag{5.42}$$

5.5.6 Lepton ID (σ_6)

The lepton identification has uncertainties of 2% and 3% for electrons and muons respectively [43]. In order to be conservative we use an uncertainty of 3% for each lepton. The same method used for the previous systematics has been used for this estimation. The final systematic error on $\mathcal{B}$ from lepton identification is the RMS of the $\mathcal{B}$ distribution obtained from this method and plotted in Fig.5.6(b):

$$\sigma_6 = 0.11 \times 10^{-2} \ \text{(2.1\% on } \mathcal{B}) \tag{5.43}$$

5.5.7 Lepton misidentification (σ_7)

A systematic error of 15% [43] of the lepton misidentification has to be applied on the Monte Carlo number of semileptonic events with fake leptons ($N_{sel}^{SL,l_{fake}}$), i.e. a 15% of systematic error on K_{lfake}. This means a relative error on the number of B^0 semileptonic events equal to $(15\% \times K_{lfake})/K^{SL} = 0.85\%$. A systematic of 0.85% on the branching ratio means:

$$\sigma_6 = 0.47 \times 10^{-3} \ \text{(0.8\% on } \mathcal{B}) \tag{5.44}$$

5.5.8 Soft pion detection (σ_8)

The systematic uncertainty to be associated to the soft pion reconstruction is due to two effects [43]: 2.2% of systematic on soft pion reconstruction efficiency and the uncertainty on the tracking algorithm which gives 1.4% effect on the efficiency. The sum in quadrature of these two systematics gives a 2.6% uncertainty for each detected soft pion. In order to calculate the systematic on $\mathcal{B}$ due to soft pion detection we allow a random variation of 2.6% on the number of events characterized by a soft pion. The RMS of the distribution of $\mathcal{B}$ obtained from this variation gives an uncertainty

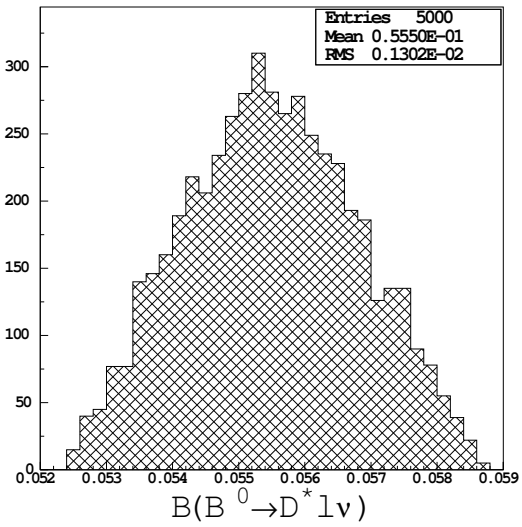

Figure 5.7: Distribution of $\mathcal{B}\left(B^0 \to D^{*-}\ell^+\nu_\ell\right)$ obtained with random killing of soft pion.

$$\sigma_8 = 0.13 \times 10^{-2} \text{ (2.3\% on } \mathcal{B}) \tag{5.45}$$

5.5.9 $m_{\rm ES}$ fits (σ_9)

The systematics due to the $m_{\rm ES}$ fits can be estimated by using a different function to fit the $m_{\rm ES}$ distribution [42]. We repeated the analysis fitting with a Gaussian instead of a Crystal-Ball function. Since all the fitting parameters are floating in $m_{\rm ES}$ fits, we do not have uncertainties related to their limited knowledge. Fitting the signal with a Gaussian function, we find the following value for the branching ratio:

$$\mathcal{B}_{Gauss}\left(B^0 \to D^{*-}\ell^+\nu_\ell\right) = (5.54 \pm 0.31)\% \tag{5.46}$$

Fig.5.8(a) and (b) show $m_{\rm ES}$ fit on RS selected data at $M_\nu^2 > -2$ obtained by fitting with a Crystal-Ball and a Gaussian function respectively.
The systematic error on $\mathcal{B}$ due to the $m_{\rm ES}$ fit is taken as the difference between the nominal fit and the Gaussian $m_{\rm ES}$ fits ($|\mathcal{B} - \mathcal{B}_{Gauss}|$), which results to be:

$$\sigma_9 = 0.62 \times 10^{-4} \text{ (0.11\% on } \mathcal{B}) \tag{5.47}$$

5.5.10 Total error (σ_{tot})

The total systematic error is the sum in quadrature of each uncertainty listed above:

$$\sigma_{syst} = 0.55 \times 10^{-2} \text{ (9.9\% on } \mathcal{B}) \tag{5.48}$$

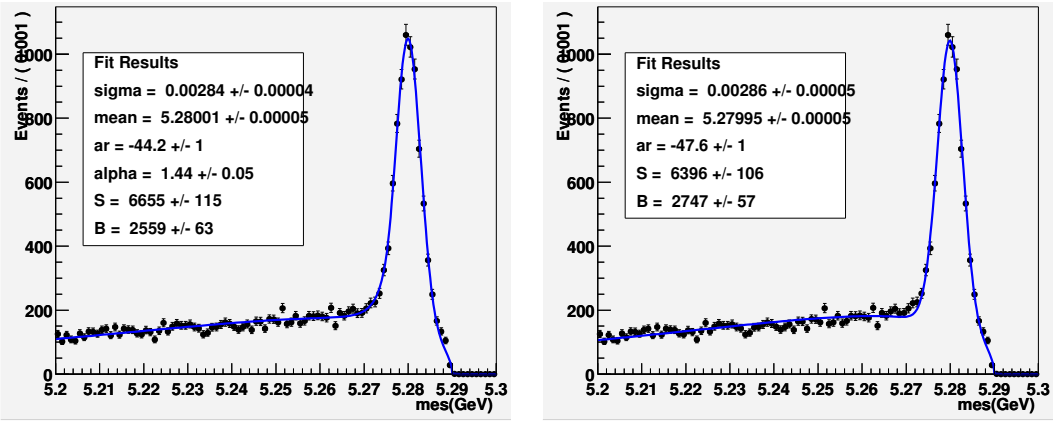

(a) (b)

Figure 5.8: Crystal-Ball (a) and Gaussian (b) $m_{\rm ES}$ fit on RS selected data at $M_\nu^2 > -2$.

which gives a total error:

$$\sigma_{tot} = 0.65 \times 10^{-2} \ \ (11.7\% \text{ on } \mathcal{B}) \tag{5.49}$$

In Tab.5.2 we report all statistical and systematic uncertainties computed in this analysis.

Error contribution	$\sigma_{\mathcal{B}} \times 10^{-2}$	$\frac{\sigma_{\mathcal{B}}}{\mathcal{B}}\%$
data statistics	0.35	6.3
1. uncertainties on $\mathcal{B}\left(B^0 \to X l\nu\right)$ and $\mathcal{B}\left(D^{*+} \to D^0\pi^+\right)$	0.42	7.7
2. Monte Carlo statistics	0.16	2.8
3a. unknown $\mathcal{B}\left(B \to D_2^* l\nu\right)$, $\mathcal{B}\left(B \to D_1 l\nu\right)$ and $\mathcal{B}\left(\text{other}B \to D^{**} l\nu\right)$	0.18	3.3
3b. unknown $\mathcal{B}\left(B \to \text{hadrons}\right)$	0.0033	0.06
4. Fully reconstructed B	0.17	3.0
5. Lepton tracking	0.043	0.8
6. Lepton ID	0.11	2.1
7. Lepton misID	0.047	0.8
8. soft pion reconstruction	0.13	2.3
9. $m_{\rm ES}$ fit	0.0062	0.11
total systematics	0.55	9.9
total error	0.65	11.7

Table 5.2: Summary of all statistical and systematic errors on the $\mathcal{B}\left(B^0 \to D^{*-}\ell^+\nu_\ell\right)$ measurement.

5.6 Measured value of $\mathcal{B}\left(B^0 \to D^{*-}\ell^+\nu_\ell\right)$

The value of $\mathcal{B}\left(B^0 \to D^{*-}\ell^+\nu_\ell\right)$ determined in this analysis by using the partial reconstruction of the D^* on the recoil of fully reconstructed B^0 is:

$$\mathcal{B}\left(B^0 \to D^{*-}\ell^+\nu_\ell\right) = (5.55 \pm 0.35(stat_{dat}) \pm 0.55(syst)) \times 10^{-2} \tag{5.50}$$

In Fig.5.9 we compare all existing measurements of $\mathcal{B}\left(B^0 \to D^{*-}\ell^+\nu_\ell\right)$ with the value obtained in this analysis, which is compatible with the world average.

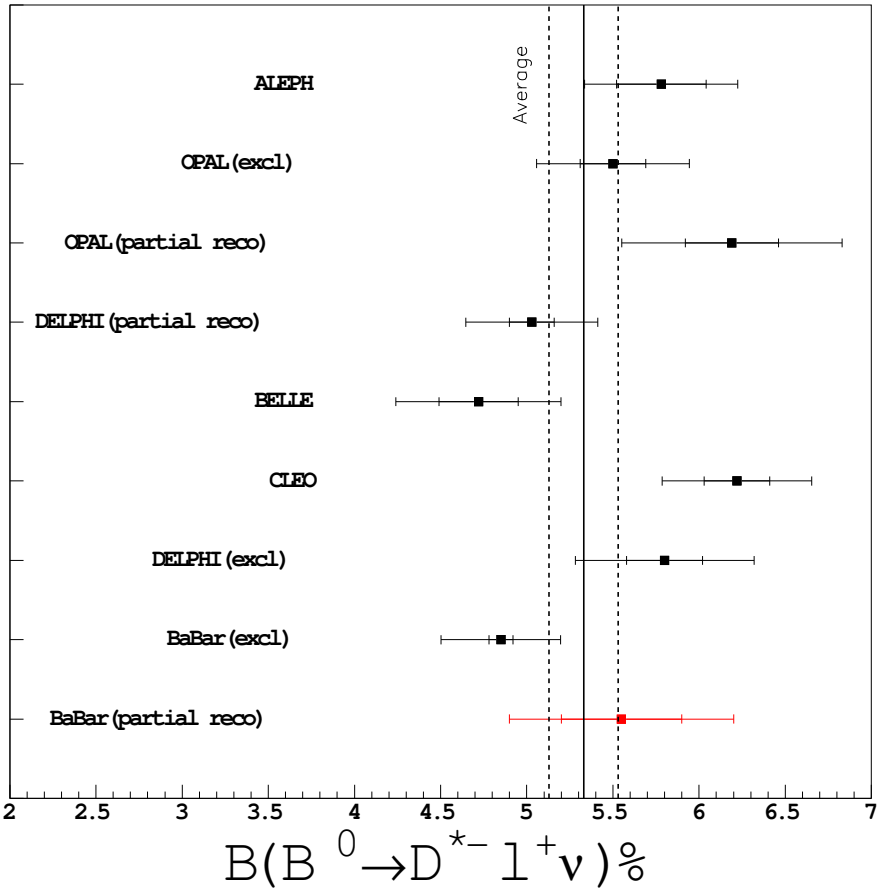

Figure 5.9: Existing measurements of $\mathcal{B}\left(B^0 \to D^{*-}\ell^+\nu_\ell\right)$ compared with the measurements obtained from this analysis (in red). The world average $\mathcal{B}_{ave} = 5.33 \pm 0.20$ is also indicated with the central value as a solid line and the error as dashed lines. The measurement of this analysis does not enter in the average.

Chapter 6

Conclusion and outlook

In this thesis we presented a measurements of the branching ratio $\mathcal{B}\left(B^0 \to D^{*-}\ell^+\nu_\ell\right)$, where the signal events have been selected by means of partial reconstruction of the D^* meson with the soft pion from the $D^{*\pm} \to D^0\pi^\pm$ decay, in events where a B meson has been fully reconstructed in an hadronic decay. Other seven experiments have measured this branching ratio. A previous *BABAR* measurement was based on the exclusive reconstruction of D^0 mesons from $D^{*\pm} \to D^0\pi^\pm$ decays. Since no good agreement appears between the existing measurements and since the exclusive analysis is systematically dominated by track and D^0 reconstruction, we measured this branching ratio with a different method. The method of the partial reconstruction allows us to ignore all tracks except the lepton from B^0 and the soft pion from D^*. Moreover by applying the partial reconstruction on the recoil of a fully reconstructed B we have less background contamination from this second B, thus obtaining a cleaner sample. The full reconstruction of one B reduces the available statistics, but the accumulated data will increase allowing to improve the statistical error. The main advantage of this method is to reduce the systematic uncertainties. The measured value of $\mathcal{B}\left(B^0 \to D^{*-}\ell^+\nu_\ell\right)$ results to be comparable with the world average. In this thesis the systematics errors have been evaluated in a simple and conservative way.

The method used in this analysis is useful for the extraction of the $\mathcal{B}\left(B^0 \to D^{*-}\ell^+\nu_\ell\right)$, and will be used to determine the CKM matrix element $|V_{cb}|$. In order to improve the measurement we plan to evaluate the systematic uncertainties in more detail. For instance we want to extract the number of signal events from all semileptonic decays $B \to Xl\nu$ and not only from semileptonic decays of the B^0. This will reduce the associated systematic uncertainty from 7.6% to 3%, since $\mathcal{B}\left(B \to Xl\nu\right)$ is known better than the $\mathcal{B}\left(B^0 \to Xl\nu\right)$. Concerning the Monte Carlo simulation, more events are now available, thus allowing another reduction of systematic uncertainties due to Monte Carlo statistics.

Appendix A

Master formula for signal extraction

A.1 Signal extraction

The physical background in this analysis can be estimated by using the following samples:

1. events at high and low M_ν^2: $M_\nu^2 \geq -2.0\,\mathrm{GeV}^2$ and $M_\nu^2 \leq -5.0\,\mathrm{GeV}^2$
2. events where the lepton and the pion have right-sign (RS) or wrong-sign (WS) charge correlation

The number of RS signal events with $M_\nu^2 \geq -2$ ($N_{sig}^{RS,2}$) will be the difference between selected events and background events:

$$N_{sig}^{RS,2} = N_{sel}^{RS,2} - N_{bkg}^{RS,2} \tag{A.1}$$

where $RS,2$ means right-sign sample with $M_\nu^2 > -2$. The number of background events can be expressed as the sum over all RS contributions from background samples, and each RS sample can be related with the correspondent WS sample as:

$$\begin{aligned} N_{bkg}^{RS,2} = \sum_{i,i\neq sig} N_i^{RS,2} &= \sum_{i,i\neq sig} \frac{N_i^{RS,2}}{N_i^{WS,2}} N_i^{WS,2} \\ &= \sum_{i,i\neq sig} NF_i^2 N_i^{WS,2} \end{aligned} \tag{A.2}$$

it is clear that the normalization factors $NF_i^2 = N_i^{RS,2}/N_i^{WS,2}$ and each contribution $N_i^{WS,2}$ cannot be extracted by data. However we can extract the total number of WS events that has to be related to the RS sample with proper normalization without using each single sample. We can then make the assumption that the following relation is approximately true for background events:

$$NF^5 \equiv \frac{N^{RS,5}}{N^{WS,5}} = \frac{N^{RS,2}}{N^{WS,2}} = NF^2 \tag{A.3}$$

where the index "5" indicates the sample with $M_\nu^2 < -5$. This means that we can estimate the background by normalizing the RS and WS samples on the data at $M_\nu^2 \leq -5.0$. Eq.A.2 can be

modified as follows:

$$N_{bkg}^{RS,2} = NF^5 \times N_{bkg}^{WS,2} + \sum_{i,i\neq sig} (NF_i^2 - NF^5) N_i^{WS,2} \tag{A.4}$$

the last term in eq.A.4 is a Monte Carlo correction which takes into account any difference in the RS/WS normalization between the total sample and its different components. This correction is zero by definition only if $NF_i^2 = NF^5$ for each i, but this is not true because background is composed by samples which may or may not peak in M_ν^2 , characterized by $NF_i^2 > NF_i^5$ and $NF_i^2 \approx NF_i^5$ respectively, as shown in Fig.A.1. Coming back to eq.A.4 we note that not only

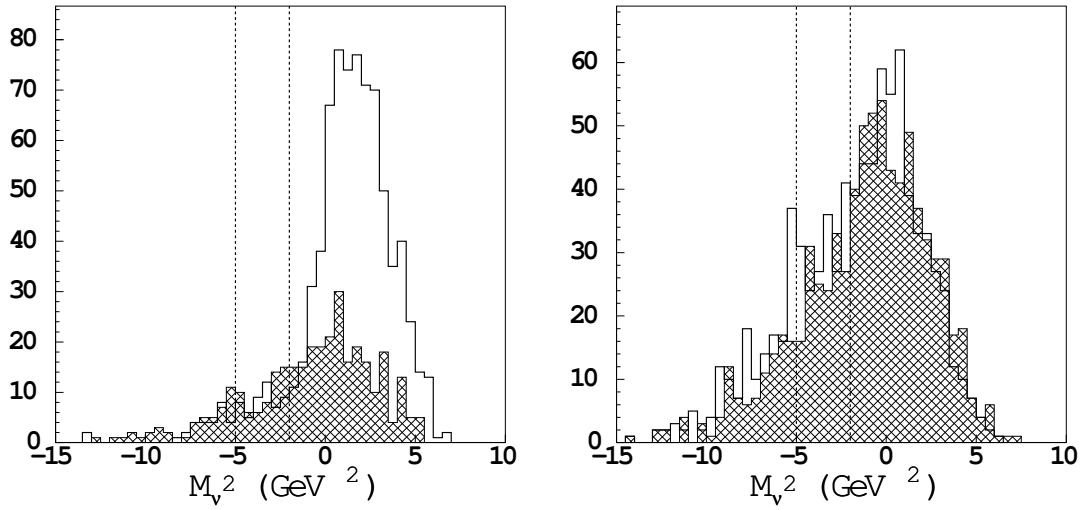

(a) (b)

Figure A.1: M_ν^2 distribution for RS (white area) and WS (cross-hatched are) for a peaking background sample in (a) and for a non-peaking background sample in (b).

$N_{bkg}^{RS,2}$, but also $N_{bkg}^{WS,2}$ cannot be extracted directly from data, since:

$$N_{bkg}^{WS,2} = N_{sel}^{WS,2} - N_{sig}^{WS,2} - N_{D^+}^{WS,2} \tag{A.5}$$

We also have to take into account that this definition of background events $N_{bkg}^{WS,2}$ contains a number of signal events, e.g. $D^* \to D^0\pi^+$ ($N_{sig}^{WS,2}$) and $D^* \to D^+\pi^0$ ($N_{D^+}^{WS,2}$) where the soft pion is wrong, that are generated in the Monte Carlo with a branching ratio, which is exactly what we want to measure from data. The same sample is included in the sum over all background samples. Since going from Monte Carlo to data we will have to rescale the above correction with their respective luminosity, as we will show later, we cannot rescale the signal samples which enter in eq.A.5 as we do with the other backgrounds. In order to understand how we correct for this contribution we isolate these two signal contributions in the sum of eq.A.4. By using eq.A.5,

the $N_{bkg}^{RS,2}$ expressed in eq.A.4 becomes:

$$\begin{aligned} N_{bkg}^{RS,2} &= NF^5 \times N_{bkg}^{WS,2} + NF^5 \times N_{D^+}^{WS,2} \\ &+ \sum_{i,i\neq sig,D^+} (NF_i^2 - NF^5) N_i^{WS,2} + (NF_{D^+}^2 - NF^5) N_{D^+}^{WS,2} \\ &= NF^5 \times \left(N_{sel}^{WS,2} - N_{sig}^{WS,2} - N_{D^+}^{WS,2} \right) + N_{D^+}^{RS,2} \\ &+ \sum_{i,i\neq sig,D^+} (NF_i^2 - NF^5) N_i^{WS,2} \end{aligned} \tag{A.6}$$

The sum over background samples gives a contribution of about 10%, as mentioned in Chap.5, then it is not negligible and we will call it MC_{corr}:

$$MC_{corr} = \sum_{i,i\neq sig,D^+} (NF_i^2 - NF^5) N_i^{WS,2} \tag{A.7}$$

then putting together eq.A.1,A.6 and A.7, $N_{sig}^{RS,2}$ will be given by the following relation:

$$N_{sig}^{RS,2} = N_{sel}^{RS,2} - NF^5 \times \left(N_{sel}^{WS,2} - N_{sig}^{WS,2} - N_{D^+}^{WS,2} \right) - N_{D^+}^{RS,2} - MC_{corr} \tag{A.8}$$

In eq.A.8 there is no way to extract $N_{sig}^{WS,2}$, $N_{D^+}^{WS,2}$ and $N_{D^+}^{RS,2}$ from data for the reasons given above, but we can extract them from Monte Carlo: the ratios between them and $N_{sig}^{RS,2}$ do not depend by the simulated branching fraction of the signal events. We can then define another MC correction as K_{MC} and we can use it to relate $N_{sig}^{RS,2}$ with accessible quantities as follows:

$$N_{sig}^{RS,2} = \frac{1}{K_{MC}} \times \left(N_{sel}^{RS,2} - NF^5 \times N_{sel}^{WS,2} - MC_{corr} \right) \tag{A.9}$$

where K_{MC} is defined as:

$$K^{MC} = 1 - NF^5 \times \left(K_{sig}^{WS/RS,2} + K_{D^+/sig}^{WS/RS,2} \right) + K_{D^+/sig}^{RS/RS,2} \tag{A.10}$$

and the three Monte Carlo factors are:

$$K_{sig}^{WS/RS,2} = \frac{N_{sig}^{WS,2}}{N_{sig}^{RS,2}} \tag{A.11}$$

$$K_{D^+/sig}^{WS/RS,2} = \frac{N_{D^+}^{WS,2}}{N_{sig}^{RS,2}} \tag{A.12}$$

$$K_{D^+/sig}^{RS/RS,2} = \frac{N_{D^+}^{RS,2}}{N_{sig}^{RS,2}} \tag{A.13}$$

As shown in chapter 5 signal events ($N_{sig}^{RS,2}$) are the sum of events with the correct soft pion $\pi_s = \pi_{soft}$ ($N_{sig(\pi_s)}^{RS,2}$) and the wrong soft pion $\pi_s = \pi_w$ ($N_{sig(\pi_w)}^{RS,2}$):

$$N_{sig}^{RS,2} = N_{sig(\pi_s)}^{RS,2} + N_{sig(\pi_w)}^{RS,2} \tag{A.14}$$

In the final calculation of the branching fraction we will use the values of $N_{sig}^{RS,2}$ and not the value $N_{sig(\pi_s)}^{RS,2}$, because the ratios between these number of events and the respective efficiencies are

the same. In order to confirm this assumption we give also the expression for $N^{RS,2}_{sig(\pi_s)}$, which is obtained from eq.A.9 by applying another Monte Carlo correction similar to those used in eq.A.13. From eq.A.14 we simply express $N^{RS,2}_{sig}$ as:

$$N^{RS,2}_{sig} = N^{RS,2}_{sig(\pi_s)} \times \left(1 + K^{\pi_w/\pi_s,RS,2}_{sig}\right) \tag{A.15}$$

where the Monte Carlo factor is:

$$K^{\pi_w/\pi_s,RS,2}_{sig} = \frac{N^{RS,2}_{sig(\pi_w)}}{N^{RS,2}_{sig(\pi_s)}} \tag{A.16}$$

The number $N^{RS,2}_{sig(\pi_s)}$ can be extracted by using the following relation:

$$N^{RS,2}_{sig(\pi_s)} = \frac{1}{K^{MC}_{sig(\pi_s)}} \times \left(N^{RS,2}_{sel} - NF^5 \times N^{WS,2}_{sel} - MC_{corr}\right) \tag{A.17}$$

where the new factor is:

$$K^{MC}_{sig(\pi_s)} = \left(1 + K^{\pi_w/\pi_s,RS,2}_{sig}\right) \times K^{MC}_{sig} \tag{A.18}$$

A.2 From Monte Carlo to Data

When we operate with formula A.9 on Monte Carlo nothing will be changed, but when finally we will apply it to the data we have to apply some changes. The factors K_{MC1} and K_{MC2} remain unchanged, when going from Monte Carlo to data, because they can be calculated only from the simulation, while the factor NF^5 will be calculated from data. The term MC_{corr} will be rescaled with the luminosity ratio between data and simulation and the same NF^5 determined from data will be used. In summary, the changes to be applied when going from Monte Carlo to data are:

$$NF^5_{data} = \frac{N^{RS,5}_{data}}{N^{WS,5}_{data}} \tag{A.19}$$

$$K^{MC,data}_{sig} = 1 - NF^5_{data} \times \left(K^{WS/RS,2}_{sig} + K^{WS/RS,2}_{D^+/sig}\right) + K^{RS/RS,2}_{D^+/sig} \tag{A.20}$$

$$\begin{aligned} MC^{data}_{corr} = {} & \frac{\mathcal{L}_{data}}{\mathcal{L}^{B^0}_{MC}} \sum_{B^0 bkg} (NF^2_i - NF^5) N^{WS,2}_i \\ & + \frac{\mathcal{L}_{data}}{\mathcal{L}^{B^+}_{MC}} \sum_{B^+ bkg} (NF^2_i - NF^5) N^{WS,2}_i \end{aligned} \tag{A.21}$$

$$N^{RS,2,data}_{sig} = \frac{1}{K^{MC,data}_{sig}} \times \left(N^{RS,2}_{sel} - NF^5_{data} \times N^{WS,2}_{sel} - MC^{data}_{corr}\right) \tag{A.22}$$

The master formula A.9 developed above can be applied at Monte Carlo in order to check the validity of the method, then eq.A.22 will be used to extract signal events from data.

Appendix B

Fit to the $m_{\rm ES}$ variable

The $m_{\rm ES}$ variable is used in this analysis and in most of the *BABAR* analyses, or more generally in B-factory experiments. This variable is a powerful tool for discriminating, on a statistical level, combinatorial and continuum background from B candidates. The variable $m_{\rm ES}$ is defined as the energy of the reconstructed B in the center of mass system:

$$m_{ES} = \sqrt{\frac{s}{4} - \vec{p}_B^2} \tag{B.1}$$

where we have substituted the reconstructed energy with $\sqrt{s}/2$, being $\sqrt{s}$ the center of mass energy. The high background rejection obtainable from the $m_{\rm ES}$ fit is due to the fact that the $m_{\rm ES}$ resolution is dominated by the center of mass energy resolution, which is very low $\approx 2.7\,\mathrm{MeV}$, and is independent from the specific B meson decay mode.

The background shape in $m_{\rm ES}$ distribution is parametrized using the Argus function [39]:

$$\frac{1}{N}\frac{dN}{dm_{ES}} = x \times \sqrt{1-x^2} \times e^{-\xi(1-x^2)} \tag{B.2}$$

where $x = m_{ES}/m_{max}$ and the shape parameter ξ is determined from a fit. The endpoint of the Argus curve, m_{max}(=5.29 GeV), is fixed in the fit, since it depends only on the beam energy. The Argus function provides a good parametrization of both continuum ($c\overline{c}$ and uds) and combinatoric background from $b\overline{b}$ events.

The signal component is fitted using a Crystal Ball function [40] defined as:

$$\begin{aligned} m_{ES} > m - \sigma\cdot a \;:\;& \frac{1}{N}\frac{dN}{dm_{ES}} = \frac{1}{\sqrt{2\pi}\sigma}\cdot e^{-\frac{(m/ES-m)^2}{2\sigma^2}} \\ m_{ES} < m - \sigma\cdot a \;:\;& \frac{1}{N}\frac{dN}{dm_{ES}} = \frac{1}{\sqrt{2\pi}\sigma}\cdot\left(\frac{n}{a}\right)^n\cdot e^{-\frac{a^2}{2}}\cdot\frac{1}{\left(\frac{(m_{ES}-m)}{\sigma}+\frac{n}{a}-a\right)^n} \end{aligned} \tag{B.3}$$

where m is the peak position, σ is the width of the Gaussian distribution, a determines the crossover point from the Gaussian distribution to the power law tail distribution and n is a

parameter describing the tail: smaller values generate a longer tail. The tail of this function accounts for energy losses in the shower of reconstructed π^0 mesons, thus the tail of the distribution depends on the reconstructed B decay mode and in particular on the number of π^0 present in it. The maximum total number of floating parameters in the $m_{\rm ES}$ fit is seven: two terms are for the Argus function, while the remaining five (N, m, σ, n and a) refer to the Crystal Ball function.

By fitting the $m_{\rm ES}$ distribution with Argus and Crystal Ball functions we estimate the number of background events as the area above a threshold in $m_{\rm ES}$, $m_{\rm ES} = 5.27\,{\rm GeV}$, of the Argus function, while the number of signal events will be the area above the same threshold of the Crystal Ball function as indicated in Fig.B.1.

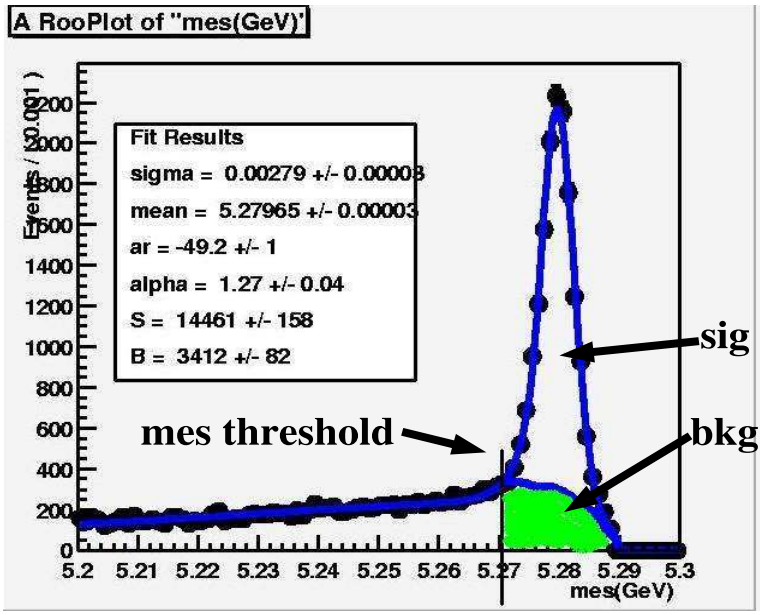

Figure B.1: Example of fit of the $m_{\rm ES}$ distribution. The green area represents the background to be subtracted, the peak above the background is the signal.

Bibliography

[1] S.L. Glashow, Nucl. Phys. **B 22** 579 (1961);
S. Weinberg, Phys. Rev. Lett. **19** 1264 (1967);
A. Salam, in Proc. of the 8th Nobel Symp., p. 367, ed N. Svartholm,
Almqvist and Wiksell, Stockholm, 1968.

[2] N. Cabibbo, Phys. Rev. Lett. **10**, 531 (1963);
M. Kobayashi, K. Maskawa, Prog. Theor. Phys. **49** 652 (1973).

[3] J. B. Richman and P. R. Burchat, Rev. Mod. Phys. **67**, 893 (1995). hep-ph/9508250

[4] Particle Data Group, S. Eidelman *et al.*, Phys. Lett. B **592**, 1 (2004).

[5] L.L. Chau and W.Y. Keung, Phys. Rev. Lett. **53**, 1802 (1984);
H. Harari and M. Leurer, Phys. Lett. B **181**, 123 (1986);
H. Fritzsch and J. Plankl, Phys. Rev. D **35**, 1732 (1987);
F. Botella and L.L. Chau, Phys. Lett. B **168**, 97 (1986).

[6] L. Wolfenstein, Phys. Rev. Lett. **51**, 1945 (1983).

[7] M. Neubert, Phys. Rep. **245**, 259 (1994).

[8] M. Neubert, Phys. Lett. B **338**, 84 (1994).

[9] For a pedagogical review see:
J. B. Richman, Les-Houches School in Particle Physics (1997) and references therein.

[10] N. Isgur and M.B. Wise, Phys. Lett. B **232**, 113 (1989);
N. Isgur and M.B. Wise, Phys. Lett. B **237**, 527 (1990).

[11] M. Wirbel, B. Stech, and M. Bauer, 1985, Z. Phys. C **29**, 637.
M. Wirbel, M. Bauer, 1989, Z. Phys. C **42**, 671.

[12] M.E. Luke, Phys. Lett. B **252**, 447 (1990).

[13] I. Caprini, L. Lellouch and M. Neubert, Nucl. Phys. B **530**, 153 (1998).

[14] The *BABAR* Physics Book, P.F. Harrison and H.R. Quinn, SLAC-R-504 (1998).

[15] S. Hashimoto *et al.*, Phys. Rev. D **66**, 014503 (2002).
(S. Hashimoto *et al.*, FERMILAB-PUB-01/317-T, hep-ph/0110253.)

[16] *BABAR* Collaboration, B. Aubert *et al.*, Phys. Rev. Lett. 93, 011803 (2004); hep-ex/0404017.
BABAR Collaboration, B. Aubert *et al.*, Phys. Rev. D - Rapid Communications 69, 111104 (2004); hep-ex/0403030.
BABAR Collaboration, B. Aubert *et al.*, Phys. Rev. D - Rapid Communications 69, 111103 (2004); hep-ex/0403031.

[17] CLEO Collaboration, J. Duboscq *et al.*, Phys. Rev. Lett. **76**, 3898 (1996).

[18] CLEO Collaboration, R.A. Briere *et al.*, LNS Preprint CLNS 01-1776 (2002); hep-ex/0203032.

[19] BELLE Collaboration, K. Abe *et al.*, Phys. Lett. B **526**, 247 (2002) ; hep-ex/0111060.

[20] *BABAR* Collaboration, B. Aubert *et al.*, *BABAR*-PUB-04/018, SLAC-PUB-10591, hep-ex/0408027.

[21] LEP V_{cb} Working Group, Internal Note,
http://lepvcb.web.cern.ch/LEPVCB/

[22] Working Group 1 Summary, CKM Workshop, CERN, CH (2002)
http://ckm-workshop.web.cern.ch/ckm-workshop.

[23] The Heavy Flavor Averaging Group (HFAG):
http://www.slac.stanford.edu/xorg/hfag/

[24] *BABAR* Collaboration, B. Aubert *et al.*, Nucl. Instrum. Meth. A **479** (2002) 1 (hep-ex/0408027).
BABAR Technical Design Report, SLAC-R-457 (1995).

[25] Private communication with Dr. Michael Sullivan (PEP-II Run Coordinator).

[26] Private communication with Dr. Rainer Bartoldus.

[27] CLEO Collaboration, S.E. Csorna *et al.*, Phys. Rev. D **61**, 111101 (2000).

[28] R. Santonico, R. Cardarelli, Nucl. Instrum. and Meth. **A409**, 377 (1981).

[29] G. P. Dubois-Felsmann, E. Chen, Yu. Kolomensky *et al.*, IEEE Trans. Nucl. Sci. **47** (2000) 353.

[30] William R. Leo, "Techniques for Nuclear and Particle Physics Experiments", Springer-Verlag, 1993.

[31] The LST Team, *A Barrel IFR Instrumented with Limited Streamer Tubes*, (Proposal from the *BABAR* Collaboration to the SLAC Experimental Program Advisory Committee), 2003. http://www.slac.stanford.edu/BFROOT/www/Detector/LST/LSTprop-A4-May30-ajss.pdf

[32] F. Forti *et al.*, Report of the IFR Barrel Replacement Review Committee, 2003.

[33] http://www.slac.stanford.edu/BFROOT/www/Detector/LST/LSTprop-A4-May30-ajss.pdf

[34] http://www.fe.infn.it/electron/babar_ifr.htm

[35] G. Battistoni *et al.*, *Operation Of Limited Streamer Tubes*, Nucl. Instrum. Meth. **164** (1979) 57.
G. Battistoni *et al. Resistive Chatode Detectors With Bidimensional Strip Readout: Tubes and Drift*, Nucl. Instrum. Meth. **176** (1980) 297.
E. Iarocci *et al.*, Nucl. Instrum. Meth. **217** (1983) 30.
G. Battistoni *et al.*, *Influence of Gas Mixture and Cathode Material on Limited Streamer Operation*, Nucl. Instrum. Meth. **217** (1983) 433.
M. Caria *et al.*, *Large Series test of Limited Streamer Tubes*, CERN-EP/87-76, 10 April 1987.

[36] G. Abbiendi *et al.*, *The ZEUS barrel and rear muon detector*, Nucl. Instrum. Meth. A**333** (1993) 342-354.
F. Fabbri *et al.*, *Results From The Testing of Limited Streamer Tubes for the OPAL Hadron Calorimeter*, CERN-EP/87-134.
G. Artusi *et al.*, *Construction of Limited Streamer Tubes For the OPAL Hadron Calirometer*, DFUB-87/10.
OPAL Collaboration, G. Artusi *et al.*, *Limited Streamer Tubes for the OPAL Hadron Calorimeter*, Nucl. Instrum. Meth. A**279** (1989) 523.
L. Piemontese *et al.*, *SLD Hadron Calorimeter with Limited Streamer Tubes: Prototype Test Results*, 29 June 1985.
MACRO Collaboration, M. Calicchio *et al.*, *The Streamer Tubes for the MACRO Experiment at the Gran Sasso Laboratory*, Proceedings of 20th ICRC,Moscow, 6 (1987) 510-512.

[37] LST Team for *BABAR* Collaboration, Collection of all tests done on LSTs prototype for the Barrel IFR replacement (2002-2003):
http://www.slac.stanford.edu/BFROOT/www/Detector/LST/index.html
http://www.slac.stanford.edu/BFROOT/www/Detector/LST/testtube_page.html
http://www.slac.stanford.edu/BFROOT/www/Detector/LST/documentation/Lu/LusPage.htm

[38] G. Cavoto, M. Negrini, M. Rotondo, *Results for μ detection efficiency for IFR barrel with LST*, *BABAR* private communication, 2003.

[39] ARGUS Collaboration, H. Albrecht *et al.*, Z. Phys. C **48**, 543 (1990).

[40] Crystal Ball Collaboration, T. Skwarnicki, DESY F31-86-02.

[41] T. Brandt, *Likelihood Based Electron Identification*, *BABAR* Analysis Documents #396 (2002).

[42] R. Faccini, D. del Re, A. Sarti, G. Denardo, S. Grancagnolo, *Semi-Exclusive B Reconstruction*, *BABAR* Analysis Documents #271, 2001.
C. Bozzi *et al.*, *Determination of $|V_{ub}|$ with inclusive semileptonic B decays*, *BABAR* Analysis Documents #347, 2002.

[43] T. Allmendinger *et al.*, *Tracking Efficiency Studies in Release 12 and 14*, *BABAR* Analysis Document #867, 2004.
Owen Long, *Measurement of the slow π relative efficiency using helicity distributions*, *BABAR* Analysis Document #54, 2001.

[44] R. Faccini, U. Langenegger, A. Sarti, D. del Re *Determination of $|V_{ub}|$ with inclusive semileptonic B decays*, *BABAR* Analysis Documents #540, 2003.

List of Figures

List of Tables

Acknowledgments

I would like to thank my tutor, Prof. Roberto Calabrese, for given me the opportunity to realize this work and for his talent demonstrated during these few years. I would also like to thank Dott. Concezio Bozzi for all work that we have done together in order to realize this thesis and for his enormous patience. A special thank to Prof. Livio Piemontese and Prof. Pietro Dalpiaz.

Finally thanks to all *BABAR* Ferrara group: Prof. Diego Bettoni, Prof. Eleonora Luppi, Dott. Ing. Angelo Cotta Ramusino, Dott. Ing. Vito Carassiti, Dott. Matteo Negrini, Dott. Gianluigi Cibinetto, Dott. Virginia Azzolini, Roberto Malaguti and Claudio Padoan.

Many thanks to my dear Elisa and her family.

The more important thanks to my parents, no explanation is needed.

Ringraziamenti

Grazie bisognerebbe dirlo a tante persone, forse troppe per poter entrare in una decina di righe. Un ringraziamento scritto qui non è solo per coloro che mi hanno aiutato nello svolgimento del lavoro di questi tre anni di dottorato, ma anche per tutte quelle belle cose che ho ricevuto da amici parenti e colleghi, per tutti coloro che in questi anni mi hanno supportato e sopportato! Alla fine di una tesi uno si sente piú sollevato nel poter cogliere l'occasione per comunicare qualcosa di bello a tutte le persone che sente vicine.

Come anticipato sopra ringrazio sentitamente il Prof. Roberto Calabrese per la fiducia che mi ha dato in questi anni nello svolgere lavori di grande responsabilità, a Carsoli mi telefonava anche in bagno... Ringrazio Roberto anche per tutte le opportunità offerte. Vorrei ringraziare inoltre il Dott. Concezio Bozzi (Concez) per avermi seguito ed aiutato nello sviluppo del lavoro presentato in questa tesi, anche se sto ancora aspettando un pranzo... che probabilmente dovró offrirgli io. Altro speciale ringraziamento va al Prof. Livio Piemontese che spero non sia troppo arrabbiato per come gli abbiamo ridotto il laboratorio, con tutta quella confusione non troverà piú gli occhiali... Un sentito riconoscimento al Prof. Diego Bettoni, per il sostegno offerto durante questi anni, e alla Prof. Eleonora Luppi per aver in parte sostituito la mamma nei momenti di bisogno quando eravamo lontani da casa. Un ringraziamento al Prof. Pietro Dalpiaz.

Un sentito riconoscimento va a tutto il resto del gruppo *BABAR* di Ferrara: Gigi (Dott. Gianluigi Cibinetto), il quale ha vissuto piú con me che con le sue morose. Matteo (Dott. Matteo Negrini), con il quale è sempre aperta la competizione per il peggior cinghiale. La Vir (Dott. Virginia Azzolini) che ha sopportato i cinghiali dell'ufficio. L'Annalisa per il supporto e consigli che mi ha fornito a per la pasta fatta a mano a SLAC. Luca per tutte le volte che mi ha sistemato il pc sbananto e per tutte le mie pare che si ascoltato. Alfredo, il grande cremino del sud. Infine Vito, Angelo, Claudio e Roberto per le super cene a SLAC, a sí propria di sugaman!
Tutti gli altri Babariani che conosco sarebbero troppi da elencare.

Saluto gli amici che mi hanno accompagnato durante il dottorato, Calza che è diventato talmente tecnologico da risultare persino fastidioso a volte... il Terun che è fastidioso per altri motivi che è meglio non specificare. Infine Pisa, pure lui è fastidioso, ma essendo in un altro ufficio altri si lamenteranno. Un saluto a Dante, con il quale non sono ancora riuscito a fare una suonatina.

Un ringraziamento ad Alberto e Michele per il supporto informatico.

Un sentito grazie a Simone e la Roby per tutto il sostegno che mi hanno dato e per la vera amicizia che mi hanno sempre dimostrato. Devo ancora pagare loro le prestazioni da camerieri svolte durante le mie pizzate...

Un affettuoso saluto a tutto lo staff dell'albergo Le Sequoie di Carsoli, che è stato la mia casa per l'inverno 2003/2004. In particolare un abbraccio a Silvia (la patata), Emiliano (il fratello matto), Maria. Un salutone a Gloria e Vittorio. Per quanto riguarda Carsoli un saluto va dedicato a tutto il personale della Pol.Hi.Tech.. Devo inoltre ricordare tutti i fisici conosciuti a Carsoli, in particolare il grande Dott. Eduard Simioni, un po' fuso eh, ma molto simpatico.

Anche se non ci lavoro piú, un particolare saluto lo dedico a tutto lo staff della Pizzeria da Moreno. Il mio maestro Moreno, la Rossella, Nicole, Roberto, Cristiana, Martina, la Milva (anche lei non ci lavora piú) e la super Cuoca cinghiala Rosanna.

Un sincero saluto agli amici a professori dell'ITIS, ricordando chi purtroppo se n'è andato, anni fa Milan e poco tempo fa Bado, lasciandoci belle cose che non scorderemo mai. Mai scorderó quando Bado mi chiamava "nano di merda!", pure Annalisa si ricorda con quanto affetto me lo diceva.

Un sincero abbraccio a Giorgia, che come me anche lei ha iniziato a girare il mondo; a Lisa con la quale ormai da anni ci dobbiamo prendere un caffè... prima o poi ci riusciremo; e a Claudia & Jo, anche con loro prima o poi una cena ci salterà fuori... Un saluto a Marco e Francesca per averci insegnato a ballare decentemente la salsa-spin. Saluto e ringrazio anche Mirco, il mio maestro di chitarra, paziente in abbondanza, visto l'allievo che si ritrova.

Non posso assolutamente dimenticare degli amici di S.Bianca, i quali mi hanno sempre seguito in tutte le mie vicende: il Kalle, Ale & Cla, Rubert e la Lara, Carlo, Marzel, il Cibano & Michi & figli, il Pablo e Silvia. Un rigraziamento particolare al Kalle, Rubert a Marzel per tutti gli spritz presi durante i racconti delle mie vicende. Un sincero ciao e grazie a tutti. Un sincero ricordo per Giorgia che ci ha lasciato.

La mia "sorellina" Serena merita un immenso riconoscimento per tutto quello che mi ha dato da quando ci conosciamo. Un abbraccio forte a Serena e Giulio, alla Mamma Antonella e alla Sorella Silvia e al cognato Riccardo. Con i due orsi Ulisse e Follia che ci avete donato, la nostra casa è piombata in un trambusto quotidiano molto piacevole! Anche se non possono leggere, pure Ulisse e Follia meritano un riconoscimento, non so se mi hanno fatto piú incazzare loro o la scrittura della tesi...

Un immenso grazie al Nonno Giuliano, che mi ha accompagnato in qualche mio viaggio e alla Nonna Carla, che ad ogni partenza del Nonno brontola, perchè avendo paura dell'aereo non puó partecipare ai nostro viaggi.

Non di meno ringrazio la Nonna Benita, che quando la guardo scorgo ancora la ragazzina che c'è in lei e ricordo sempre nel cuore il Nonno Franco che in passato mi chiamava *capelón*, mentre negli ultimi anni era solito chiamarmi *pelatón*, per ovvi motivi.

Un saluto a tutto lo Ziame e Cuginame.

Con le parole posso solo tentare di esprimere quanto sono grato alla mia piccola Eli, ha anche cercato di stare sveglia, senza successo, mentre passavo le notti in bianco per scrivere, ma solo il pensiero bastava per spingermi avanti ad oltranza. Devo riconoscere l'ospitalità e la disponibilità offertami da tutta la Famiglia Pasti e Pastine comprese. Prima o poi anche i cognati desiderosi di pizza saranno saziati insieme a tutto il Nipotame (come l'Eli è solita chiamare i nipoti quando alle 7 del mattino combinano il disastro), chitarristi e non. Grazie veramente di cuore.

Per il gran finale, come posso ringraziare i miei genitori Marco e Marina? Per tutto quello che hanno fatto per me a per tutto quello che continuano a fare e, semplicemente, soprattutto perchè sono i miei genitori, e questo basta a spiegare tutto, non ci sono parole che possano ringraziare abbastanza. Spero che il sincero riconoscimento possa essere sempre evidente dal mio sorriso. Un abbraccio forte e grande!

Grazie a tutti, ciao!
Mirco